Dynamics of Granular Poiseuille Flow

A Thesis
Submitted for the Degree of
Master of Science (Engineering)

by

Deepthi S

Engineering Mechanics Unit
Jawaharlal Nehru Centre for Advanced Scientific Research
(A Deemed University)
Bangalore – 560 064

JANUARY 2014

To Thatha

DECLARATION

I hereby declare that the matter embodied in the thesis entitled "**Dynamics of Granular Poiseuille Flow**" is the result of investigations carried out by me at the Engineering Mechanics Unit, Jawaharlal Nehru Centre for Advanced Scientific Research, Bangalore, India under the supervision of **Prof. Meheboob Alam** and that it has not been submitted elsewhere for the award of any degree or diploma.

In keeping with the general practice in reporting scientific observations, due acknowledgment has been made whenever the work described is based on the findings of other investigators.

Deepthi S

CERTIFICATE

I hereby certify that the matter embodied in this thesis entitled "**Dynamics of Granular Poiseuille Flow**" has been carried out by **Ms. Deepthi S** at the Engineering Mechanics Unit, Jawaharlal Nehru Centre for Advanced Scientific Research, Bangalore, India under my supervision and that it has not been submitted elsewhere for the award of any degree or diploma.

Prof. Meheboob Alam
(Research Supervisor)

Acknowledgements

It has been a wonderful two year stay at JNC. It would not be so if not for the people who helped me to grow into a better individual intellectually and personally.

I would like to first thank my advisor Prof. Meheboob Alam for his constant guidance and motivation. He gave me a lot of independence to work which helped me to become a better researcher. Regular presentations helped me overcome my stage fears and become a better speaker. Two important things I have learnt from him are attention to detail and dedication towards work.

I thank Prof. K. R. Sreenivas for his guidance. Prof. Rama Govindarajan has been an inspirational figure. I would like to thank Prof. S. Balasubramanian who taught scientific computing in FORTRAN. Thanks to CCMS for organizing a short 15 day course on shell programming and Linux operators. It helped speed up the post processing of the results.

Life in JNC would not be colorful if not for *EMUites*. Though I got to know *Ponnu* personally just for a few months, she has been a great influence to me. She has been like a elder sister who has helped and guided me throughout my 2nd year. *Rashmi*, who I know since my first day at JNC was a great company. I remember both of out attempts to do combined studies at the eleventh hour before final exams. I would have felt very lonely at the lunch tables if not for *Chakri*, *Deepak*, *Kanwar*, *Milli*, *Navaneeth*, *Prashanth*, *Rajesh*, *Sankalp*, *Reddy*, *Vicky*. Our debates varied from cats in JNC to Rahul Gandhi. Most of all I cannot forget the birthday parties and late night pizza eating sessions with all the EMUites. For any technical glitches I have always relied on *Rajesh*, *Prashanth* and *Milli* who have helped me immensely. Thanks to *Saikishan* and *Aarthi* - the lovely fluid dynamists couple of EMU, from whom I have received valuable advice. Talks with my lab-mates - *Priyanka Shukla*, *Ashish*, *Ujjain*, *Reddy*, *Saikat*, *Ansari*, *Ryan* were motivating. I cannot forget the time spent with with *Nivedita*, *Sharmila*, *Priyanka*, *Manjusha*, *Shiwani*. I had some laughing sessions with *Shashank*, *Siddharth*, *Sunil*, *Vybhav*.

TT with *Sanjeev*, *Bharat*, *Alok*, *Gayatri* and many others was the best recreation. *Sharanappa* and *Raju's* amazing coffees quenched my caffeine addiction.

I thank the academic, admin, security, mess committee for all their support. I thank JNCASR for providing all facilities to pursue my graduation.

Finally, I thank my grandfather who never lost hopes on me. His love, affection and support towards me knew no bounds. Abhinav has been a pillar of strength through my peaks and plateaus. My mother, father, sister, grandmother, aunts, uncles, and cousins have been very supportive.

Abstract

In the present study, a basic problem of granular particles flowing in a channel under the influence of gravity is considered. Granular particles are modeled as smooth inelastic hard spheres which interact through binary collisions. Event-driven molecular dynamics simulation is used to study granular Poiseuille flow in two and three-dimensions.

2D Poiseuille flow

In the first part, the bi-modality in granular temperature profile is studied as a function of normal restitution coefficient (e_n), wall roughness (β_w) and volume fraction (ν) and the results are compared with previous theoretical work. In the second part, the velocity distribution functions (VDF) are analyzed for varying e_n and β_w over three orders of magnitude of Knudsen number [Kn $\sim$ O(1), O(0.1), O(0.01)] for dilute flows. The VDFs tend to obey a Gaussian for nearly elastic collisions ($e_n \sim 1$) but are non-Gaussian if the system is dissipative. The high-velocity tail of VDFs is fitted to $\sim C \exp^{(-\gamma(|u|/\sigma)^{\alpha})}$ where c is the normalized fluctuation velocity. It is found that the exponent $\alpha(e_n$, Kn, $\beta_w)$ decreases with the reduction of Knudsen number. For Kn $\sim$ O(1) with smooth walls, the exponent is $\sim$ 2.0 (i.e. a Gaussian) throughout the system but decreases as we move from the center of the channel towards the walls for both Kn $\sim$ O(0.1) and Kn $\sim$ O(0.01). The VDF for cross-stream fluctuation velocity is found to be bimodal for dissipative flows, and the degree of bi-modality is enhanced with increasing Knudsen number.
In the final part of 2D granular flows, slip velocity (U_w), wall temperature (T_w) is looked into. Effect of normal restitution coefficient and wall restitution coefficient on U_w, T_w and their gradients [$d(U_w/U_0)/dy$ and $d(T_w/y_0)/dy$] is studied for dilute flows ($\nu = 0.01$). An effort is made to understand the relation between Knudsen number, slip velocity and gradient of slip.

3D Poiseuille flow

Two geometries are considered in 3D flows - (i) the flow between two parallel plates and (ii) the flow in a closed duct. Mean field properties like velocity (U), granular temperature (T) and volume fraction (ν) along with VDFs, as a function of normal restitution coefficient (e_n), are studied for both geometries. For dissipative systems ($e_n < 1$), the particles accumulate in the center of the channel, exhibiting various wave patterns. Evolution of density waves with time is studied in detail in 3D channels with square cross-section. Plug, symmetric and asymmetric waves are different types of patterns observed in simulations. To analyze the effect of asymmetry in flow in a duct, the width (W) of the system is increased compared to the depth (D). Separation and periodic migration of density waves along the width (W) of the channel is evident.

List of Figures

List of Tables

Contents

Chapter 1

Introduction

Granular materials can be defined as individual solid entities put together. Their size ranges over many orders of magnitude - from micron (below this size Brownian motion of the particle becomes dominant) to huge boulders of ice floating in the polar region. Two important features of granular particles are [Jaeger *et al.* (1996)] - (i) the room temperature (T) does not affect them. The energy k_bT, where k_b is the Boltzmann's constant is negligible. The relevant parameter is mgd where m is the mass of the particle, g is gravitational acceleration and d is the particle diameter. This is greater than k_bT by twelve orders of magnitude. (ii) collisions are dissipative. Granular matter can be considered a separate state of matter as they behave like a solid when at rest, liquid when made to flow and a gas in dilute conditions. Study on sand piles by Leonardo da Vinci, laws of dry friction by Coulomb and study of effect of vibration on sand piles by Michael Faraday laid the fundamental foundation for granular physics.
Granular materials can be studied as a group of particles as in case of discrete models or can be modeled as a continuous medium as in continuum analysis. Limitations in computing power does not allow us to simulate large system using discrete models but flow in complex geometries can be easily modeled [Rao *et al.* (2008)].

1.1 Some interesting phenomena

Granular particles exhibit myriad phenomena such as granular saltation, singing sands, Brazil nut effect, granular convection and pattern formation. In this section, we introduce some of these phenomena.

Brazil nut effect
When a box of different sized particles is shaken vertically, the larger particles tend to accumulate at the top while the smaller particles settle at the bottom. This phenomena is called Brazil nut effect The name Brazil nut comes from the fact that Brazil nuts are always found on the top when a cereal box is opened. Some explanations suggest that each time the box containing polydisperse granular particles is shaken vertically, the smaller particles tend to seep through the interstitial space to the bottom [Rosato *et al.* (1987)], thus letting the larger particles to come up. Some studies suggest that the convection currents set due to the vertical vibrations, density difference and air flow also have effective contributions [Möbius *et al.* (2001)]. Another complication observed while experimenting on Brazil nut effect is the reverse Brazil nut effect explained by Shinbrot & Muzzio (1998). Their experiment showed that if two large balls of different densities are vibrated vertically in a granular bed, the lighter ball migrates down and stays at the bottom at all times whereas the heavier ball tends to remain at the top.

Singing sands

It is a distinctive booming/whistling sound is observed in some sand dunes and sea shores when an avalanche is created by displacing the top layer of the sand. The dune is said to act as a resonator. Vriend (2010) lists few sand dunes are found all over the world which produce such sounds. They summarize from various other studies that the frequency of the sound produced in the dunes depends on the size of the particle, size distribution and moisture content [Vriend (2010)]. Laboratory experiments done by Goldsack *et al.* (1997) show that booming noise is produced in silica-gel type materials. Not much research is done till date to understand them thoroughly.

Maxwell's demon effect

When a cell with a large number of compartments containing granular particles is vertically shaken at an optimum frequency for sufficient time, all the particles tend to cluster in a single compartment due to dissipation. This phenomena is analogous to the Maxwell's demon effect seen in gases.

Pattern formation

Many interesting structures are formed when granular particles are vibrated. One can see different oscillating peak-like patterns when granular particles are vibrated in a Hele-shaw cell and in circular plates. Streaks like patterns were observed experimentally by Forterre & Pouliquen (2001) for flow down a inclined plane. In Chapter 5 we discuss the various patterns formed in granular Poiseuille flow.

1.2 Industrial applications

Granular materials are used in almost all manufacturing industries. One of the first documented research on bulk solids was by *Janssen*. As the saying goes - 'necessity is the mother of invention' - during the end of $19th$ century there was excess import of corn. He discovered that, unlike in liquids, the pressure at the bottom of a vertical silo does not proportionally increase with the height of the corn. He devised a scale similar to the barometric scale of fluids which is used till date [Sperl (2006), Schulze (2012)].

Processing of clinkers for cement production, processing of food grains, mixing of powders to manufacture tablets in pharmaceutical industries, extraction of metals from ores, all require proper design of equipments to handle these granular materials. After water, granular materials are the second most used raw material. They account for 10% of the energy consumption in industries [Duran (2000)]. Though extremely important not much efforts are put in optimizing the design of equipments which process them (except the major ones like silos and hoppers).

Two most important problems encountered in processing grains are segregation and clogging. Segregation is a phenomenon where two different mixtures of particles separate out after mixing, due to small differences in properties like size, shape and density . It is a colossal problem especially in pharmaceutical industry where different powders with different chemical compositions need to be mixed homogeneously. Uniformity is achieved by mixing the powders a number of

times in different mixers which is time consuming. Lack of realistic models and continuum descriptions are the reasons for poor engineering of mixers [Ottino & Khakhar (2000)]. Clogging is another major problem encountered in hoppers and chutes. It is caused due to jamming where a large number of particles accumulate and obstruct the flow.
While designing granular flow equipments for industries, along with parameters like shape, size and distribution of particles; humidity, temperature, chemical composition and other variables also need to be accounted for. It is not possible to include all these in design consideration. Thus, engineers includes two-three important variables for the design. Proper quantification of the bulk properties of granular matter based on particle-level properties and system parameters would benefit the industries.

1.3 Chapter organization

In our present study we consider rapid flow dry granular matter. Some interesting reviews in rapid flows are Campbell (1990) and Goldhirsch (2003). A simple problem of flow of granular particles in a channel under the influence of gravity (Poiseuille flow) is simulated for 2D and 3D cases. The results of 2D granular flows are discussed in Chapter 3 and 4. 3D granular flows are dealt in the Chapter 5.

Chapter 2
In this chapter, the geometrical description of the problem is given. Details of the event-driven molecular dynamics algorithm is discussed briefly. The hard sphere collision dynamics of two granular particles is explained with schematic diagrams. The equations of used to obtain the mean properties like velocity, volume fraction and density are listed. The results from the present code is validated with published results [Alam & Chikkadi (2010)].

Chapter 3
The chapter is divided into 2 sections. In the first section, mass flow rate is studied as a function of Knudsen number for 3 different volume fractions $\nu = 0.01$, 0.1 and 0.3 for granular Poiseuille flow. The granular temperature (T) exhibiting bimodal behavior is analyzed as a function of normal restitution coefficient (e_n), wall restitution coefficient (β_w) and volume fraction (ν).
In the second section, results for the velocity distribution function (VDF) in dilute granular flows are presented for different orders of Knudsen number as a function of e_n and β_w. The tails of the distribution are analyzed similar to the method used by van Noije & Ernst (1998) and van Zon & MacKintosh (2005).

Chapter 4
This chapter has 2 sections. In the first, slip velocity (U_w) and its gradient ($d(U_w/U_0)/dy$) is studied as a function of e_n, Knudsen number and β_w. We also try to analyze the relationship between the slip velocity, gradient of slip velocity and Knudsen number which corresponds to the boundary conditions in granular Poiseuille flow.
In the second section, the variation of wall temperature (T_w) and gradient of wall temperature

(dT_w/dy) is looked into.

Chapter 5

Simulations are done for 2 different geometries - flow between two parallel plates and flow in a square duct. All simulations in this chapter are done for moderately dense flows $\nu = 0.15$. This chapter has 5 sections. The results in the first 4 sections are for square cross-section of the system.

In the first section, mean properties are examined at varying dissipations (e_n). In the second section - VDF results are shown for varying restitution coefficients for both flow between two parallel plates and flow in a square duct. Density wave pattern observed in flow in parallel plates and square duct are examined in third and fourth section, respectively. The power spectrum analysis similar to Liss *et al.* (2002). The fifth section explain the results obtained for simulating rectangular channel.

Chapter 2

Problem description and simulation technique

2.1 Problem description

In the present study, a basic problem of granular flow through a channel under the influence of gravity (Poiseuille flow) is considered. Simulations are done for 2 and 3 dimensional channel flows, see Fig. 2.1.
The width of the channel is represented by W/d where d is the diameter of the sphere. L/W is the ratio of length to width and D/W (for 3D flows) is the ratio of depth to width. Trials are done for mono-disperse spheres and all the system dimensions are scaled by the particle diameter (d). The system is periodic in x-direction for both 2D and 3D cases. The walls are present in the y-direction for the 2D case (Fig. 2.1a); the z-direction is periodic for flows between two parallel plates. The walls are present in y- and z-direction for flows in a closed channel. The body force (g), represented by the red arrow in Fig. 2.1, acts in the positive x-direction.

2.2 Model used

Granular particles are modeled using hard sphere potential. According to this the particles are impenetrable and interact only during collisions. The hard sphere potential is given by

$$U(r) = \begin{cases} 0 & (r > d) \\ \infty & (r \leq d) \end{cases} \tag{2.1}$$

All the particles are assumed to be smooth i.e. there is no rotational degree of freedom.

2.3 Hard sphere collision dynamics

Consider two particles 1 and 2 move towards each other for collision as shown in Fig. 2.2. Let $\vec{u}_1, \vec{u}_2$ be the pre-collision velocities and $\vec{u'_1}, \vec{u'_2}$ be the post collision velocities. Collisions occurring only in pairs are accounted for. Thus, conservation of linear momentum gives

$$m\vec{u}_1 + m\vec{u}_2 = m\vec{u'}_1 + m\vec{u'}_2 \tag{2.2}$$

The mass of particles is set to unity. The collisions between granular particles are always inelastic and some amount of energy is lost during this process. The coefficient of restitution (e_n), which is the ratio of post-collision velocity to the pre-collision velocity, quantifies this energy loss. It is assumed to be constant throughout the simulation though in practice it depends on the impact

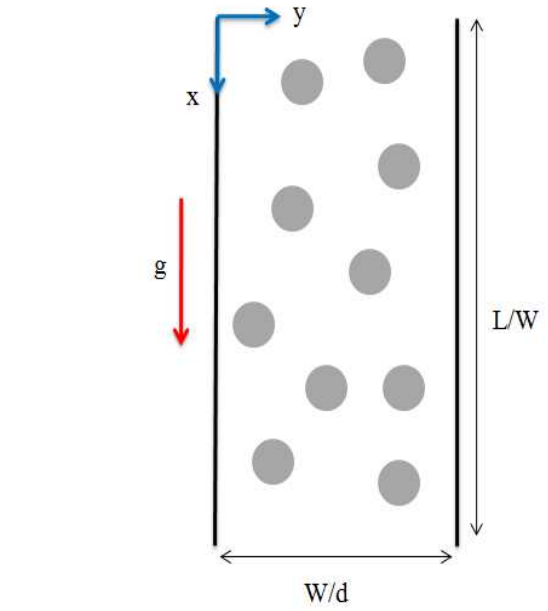

(a)

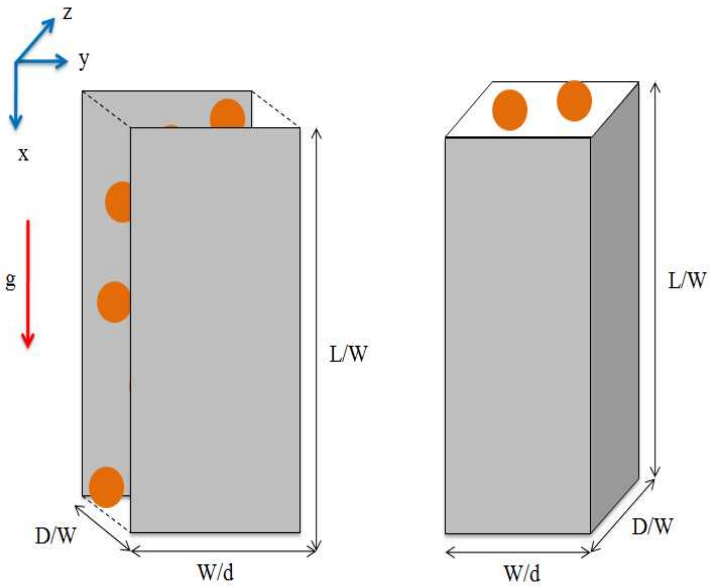

(b)

Figure 2.1: Schematic of the (a) 2D system (b) 3D system

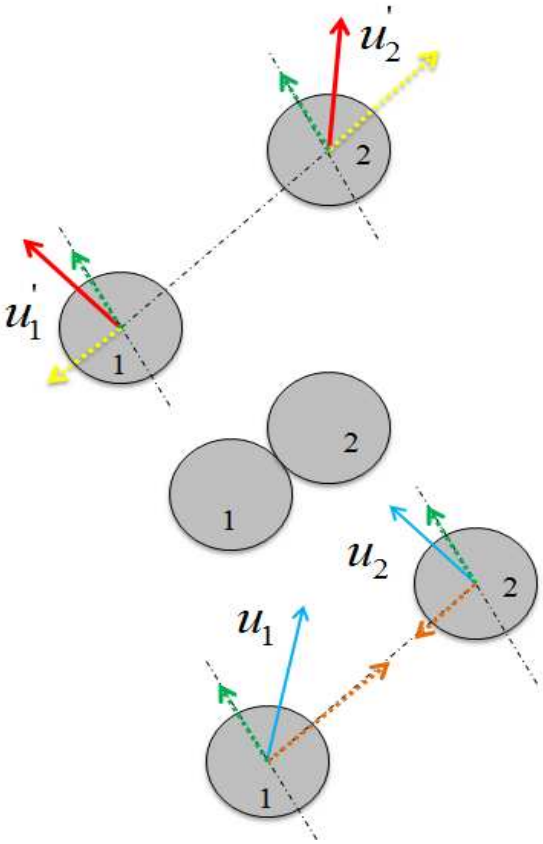

Figure 2.2: Vector diagram of two smooth hard spheres (1) and (2), before and after collision. u_1, u_2 are pre-collision velocity and $\acute{u}_1$,$\acute{u}_2$ are post-collision velocities

velocity Lun & Savage (1986). During a collision the particles conserve their tangential velocity and the loss is manifested as change in the normal velocity which is the velocity component along the line joining the particle centers. Thus we can write

$$\vec{u'}_{12}.\vec{n} = -e_n\vec{u}_{12}.\vec{n} \tag{2.3}$$

where $\vec{n}$ is vector in normal direction and $\vec{u}_{12} = \vec{u}_2 - \vec{u}_1$. The coefficient of restitution varies from 0 to 1. It is set to 1 for elastic collisions and less than 1 for inelastic collisions.

Expanding Eq. 2.3

$$\vec{u'}_1 - \vec{u'}_2 = -e_n\vec{u}_1 + e_n\vec{u}_2 \tag{2.4}$$

Substituting Eq. 2.4 in Eq. 2.2 and rearranging the terms we get post-collision velocity in terms of pre-collision velocity as:

$$\vec{u'}_1 = \vec{u}_1 - \frac{1+e_n}{2}(\vec{u}_{12}.\vec{n})\vec{n} \tag{2.5}$$

$$\vec{u'}_2 = \vec{u}_2 + \frac{1+e_n}{2}(\vec{u}_{12}.\vec{n})\vec{n} \tag{2.6}$$

Collision time calculations

Consider two particles of same diameter d at distances r_1 and r_2. At any time t, for the collision to occur the minimum distance between the particles must be equal to the particle diameter.

$$\vec{r}_1(t) - \vec{r}_2(t) = d \tag{2.7}$$

$\vec{r}_2$ can be written in terms of $\vec{r}_1$

$$\vec{r}_2(t) = \vec{r}_1(t_0) + \vec{u}_{12}t_{12} \tag{2.8}$$

Substituting Eq. 2.8 in 2.7 and squaring on both sides we get

$$[\vec{r}_{12} + (t_{12}\vec{u}_{12})]^2 = d^2 \tag{2.9}$$

The above equation is quadratic in t_{12}.

$$t_{12} = t_0 + \frac{(-\vec{u}_{12}.\vec{r}_{12}) \pm \sqrt{(\vec{u}_{12}.\vec{r}_{12})^2 - \vec{u}_{12}^2(\vec{r}_{12}^2 - d^2)}}{\vec{u}_{12}^2} \tag{2.10}$$

The solution of the above quadratic equation can be real or complex. If real, it can be positive or negative. In order to eliminate the complex and negative roots and zero down to the minimum time of collision the following conditions are imposed.

Condition A:

The particles can be moving parallel to each other, away from each other or towards each other. The collisions occur when particles move towards each other. To find out the the condition for such a situation a vector construction is shown in Fig. 2.3. The red line represent u_{12} and the green line represents r_{12} which are the resultants of the individual velocity and position vectors of particle 1 and 2. It can be seen that for the particles to be moving towards each other, the

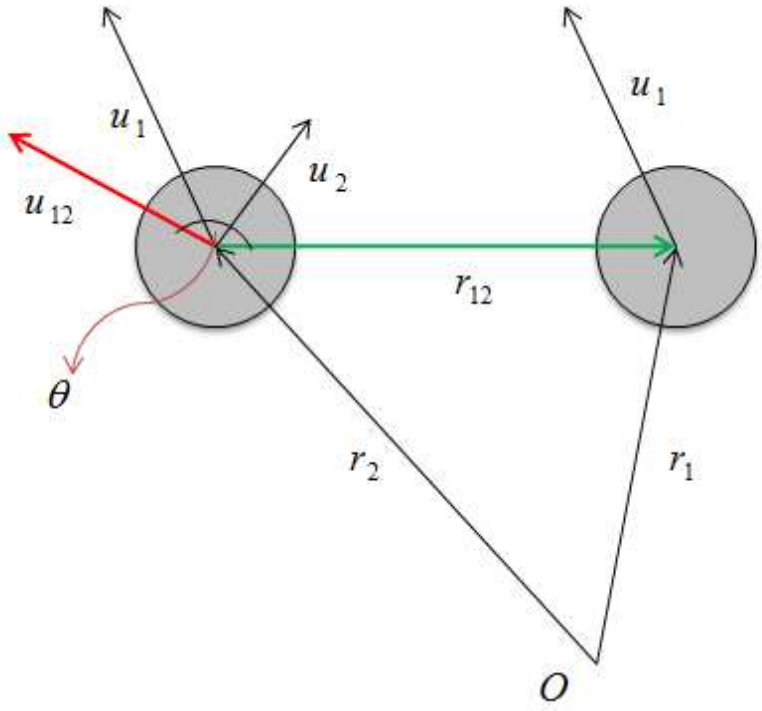

Figure 2.3: Vector construction showing condition for 2 particles to collide

dot product $\vec{u}_{12}.\vec{r}_{12} < 0$ or $\frac{3\pi}{2} > \theta > \frac{\pi}{2}$ where θ is the angle between the 2 vectors $\vec{u}_{12}$, $\vec{r}_{12}$. If this product is positive then the particles are moving away from each other.

Condition B:

Further to eliminate complex root, Eq. 2.10 must satisfy the rule of discriminant.

$$(\vec{u}_{12}.\vec{r}_{12})^2 - \vec{u}_{12}^2(\vec{r}_{12}^2 - d^2) >= 0 \tag{2.11}$$

Condition C:

When all the above conditions are fulfilled two real roots are obtained. The larger root is neglected as the particles are impenetrable while the small root is chosen.

Boundary conditions

There are various ways in which the walls can be modeled. Lennard-Jones potential is commonly used to model flow of molecular gases. Some assume that once the particle hits the wall they lose their previous memory and the new particle velocity is assigned as per Maxwellian distribution. The walls can also act as thermostats through which the system can be heated or cooled.

In our simulations, the boundary conditions are set such that the particles which hit the wall either bounce back or specularly reflect as shown in Fig. 2.4. Due to the impenetrable boundary condition the magnitude of the normal velocity is unchanged whereas the tangential component of the velocity can change. To characterize this, a parameter called wall restitution or tangential restitution coefficient (β_w) is defined, which is the ratio of post collision tangential velocity to pre-collision tangential velocity. This also is assumed to be a constant throughout the simulation.

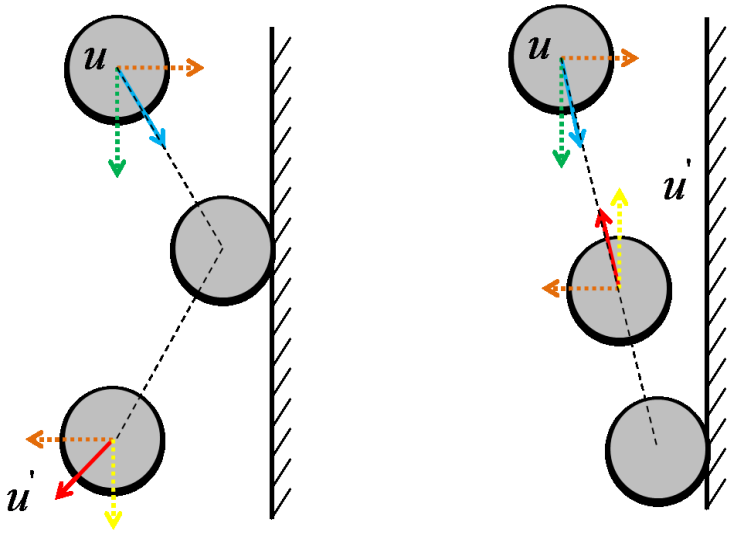

Figure 2.4: Vector diagram of particle 1 and 2 colliding with the wall

Thus, collision rule for wall-particle collision for 2D granular Poiseuille flow is as follows:

$$\vec{u}_x = -\beta_x \vec{u}_x, \tag{2.12}$$
$$\vec{u}_y = -e_w \vec{u}_y, \tag{2.13}$$

where $e_w = 1$ for walls and β_w = [-1,1].
For the 3D simulations in a closed channel, the collision rule for a wall-particle collision is as follows

$$\vec{u}_x = -\beta_x \vec{u}_x, \tag{2.14}$$
$$\vec{u}_y = -e_{wy} \vec{u}_y, \tag{2.15}$$
$$\vec{u}_z = -e_{wz} \vec{u}_z, \tag{2.16}$$
$$\tag{2.17}$$

where e_{wy}, $e_{wz} = 1$ for walls and β_w = [-1,1].
For the 3D flows between two parallel plates, the collision rule for a wall-particle collision is as follows

$$\vec{u}_x = -\beta_x \vec{u}_x, \tag{2.18}$$
$$\vec{u}_y = -e_w \vec{u}_y, \tag{2.19}$$
$$\vec{u}_z = -\beta_z \vec{u}_z. \tag{2.20}$$
$$\tag{2.21}$$

where $e_w = 1$ for walls and β_x, β_z = [-1,1].
In above equations, β_x and β_z are set to -1 for specular reflection and to 1 for bounce back condition [Chikkadi & Alam (2007); Alam & Chikkadi (2010)]. The walls which reflect all particles (β_w = -1) forward are called *smooth walls*, and those which bounce back ($\beta_w = 1$) the particles

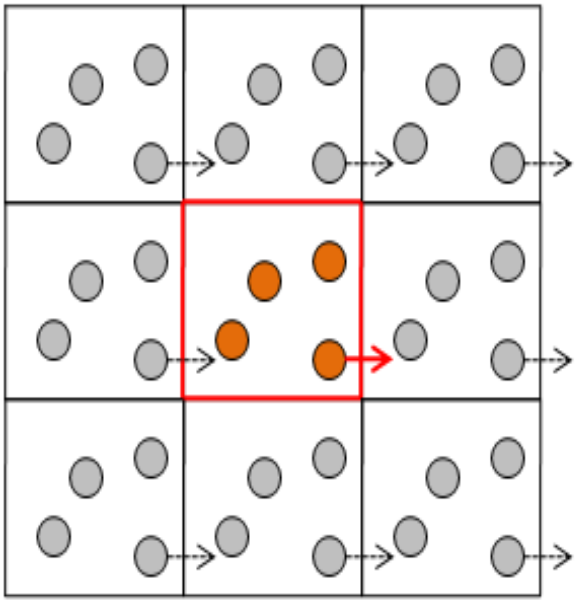

Figure 2.5: Schematic of periodic boundaries

in the direction of incidence are called *perfectly rough walls*.
The no slip boundary condition corresponds to $\beta_w = 1$, for elastic collisions.

Periodic boundaries

Periodic boundary conditions are used to mimic large systems. The positions of the particles are replicated in all directions as shown in Fig. 2.5. If a particle moves out of the box as depicted by solid arrow, the corresponding particles in all the other cells also move as marked by broken arrow. In the present Poiseuille flow problem the domain is periodic in x-direction. Thus, for all the particles leaving the cell through the bottom boundary, a periodic image of the particle is created in the top boundary. Thus periodic boundary condition in x-direction implies that the system is replicated infinitely in the x-direction. In 3D simulations, two directions - x and z are periodic for flow between two parallel plates and only x-direction is periodic for flow in closed channel

Inelastic collapse In our our simulations the normal restitution coefficient (e_n) is kept constant. For very small values of e_n (~ 0.0) there might be a condition where two particles collide infinitely in a finite interval of time. This effect is called inelastic collapse [McNamara & Young (1992); Pöschel & Schwager (2005)] and is commonly encountered in molecular dynamics simulations where the system is highly dissipative. In order to prevent this, we adopt the TC rule formulated by Luding & McNamara (1998). According to this rule, if the collision time between particles is less than a critical time of collision (t_c) then e_n is set to 1 which implies elastic collision. This critical time of collision in all our simulations is set to 10^{-9}.

2.4 Simulation procedure

A general procedure of molecular dynamics involves step by step process of moving the system by an interval of δt along with accounting for the collisions which might occur in the time interval. All input parameters (eg. e_n, β_w) are assumed to be independent of time. In such cases of event-driven molecular dynamics, the system moves from one state to another with respect to events. The main assumption in event-based molecular dynamics is that at any instant only one collision occurs in an infinitesimal small interval of time. The framework of this event-based simulation constitutes the following steps [Allen & Tildesley (1989)]:

1. Setting up particle positions in the system [r_{ix},r_{iy},r_{iz}]
2. Initialization of particle velocities $[u_{ix}, u_{iy}, u_{iz}]$
3. Calculation of collision time of all particle pairs $(t_{12}, t_{13}...t_{1n}...t_{(n-1)n})$
4. Find the minimum of collision between particle pairs t_{ij}
5. Move the system to time $t = t_0 + t_{ij}$ by calculating the new positions and velocities of the system
6. Go to step 3

In such a procedure there are two types of events - particle-particle collision and wall-particle collision.

Domain modification In a scenario as described above one needs to calculate the collision time between all the pairs of particles 12, 13, 14 ..., 23 ,24 ...., (n-1)n. The computational time required is of the order of the $O(N)$ per event processed. Such algorithms are efficient only for small number of particles.

To ease the load it was suggested that the domain be divided into regions and the collision partners of i be searched in cells neighboring the cell containing particle i. For example, in 2D case, particles in 8 neighboring cells and the cell in which the particle is present is to be looked into as shown in Fig. 2.6. This reduces the computational load to $O(logN)$ per one processed event (Lubachevsky (1991)) for a system with all peroidic boundaries. Using such scheme, following are considered as an event while simulating Poiseuille flow - particle-particle collision, cell-crossing and wall-particle collision. In order to implement this scheme efficiently a separate array-list is required, which contains information regarding the particles, the cell to which they belong, and their neighbors. Though this is computationally burdensome, it is better than the conventional method where one moves the whole system event by event

Event calendar

The present molecular dynamics code is based on the algorithm developed by Rapaport (1980, 2004). An event calendar contains a list of future events, its partners and the time of occurrence of the event. For a large number of particles it becomes imperative to not only use manage the calendar effectively but also use the memory space economically. A event calendar must satisfy the following conditions:

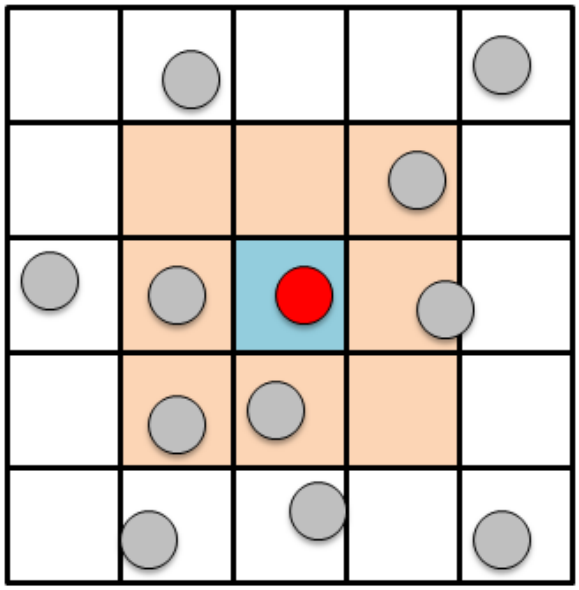

Figure 2.6: Schematic of cell division in 2D system

- Should be easy to add and delete events.
- Should be ordered depending on the time of event occurrence.
- No memory wastage in any step of the algorithm.

In the present algorithm event calendar is maintained in the form of a binary tree. Each event is represented by a node.
Node:
A node carries information about collision partner for particle-particle collision, particle number and which cell it is crossing for cell crossing, and particle number and which wall it collides along with the time of event. A node can be pictorially represented as shown in Fig. 2.7. It is initialized as follows:

typedef struct{
real time;
int left, right, up, circAL, circAR, circBL, circBR, idA, idB;
}*Evtree;*

Unlike a linear linked where a single pointer connects one node to another, this structure has 2 pointer (*left, right*) which connect to two successive nodes. These are placed such that the occurrence of the event in left node is before the current node and the occurrence of event in the right node is after the current node event. The pointer *up* is used for easy traversing through the binary tree. *circAL, circAR, circBL, circBR* are used to maintain doubly linked circular lists where A and B represent the 2 lists. *idA, idB* store information required to process the event. They represent the particle identity if the future event is a collision or represent the wall identity and particle number in case of wall collision. For cell crossing they represent the particle identity and identity of the cell. The real pointer *time* represents the time of the event.

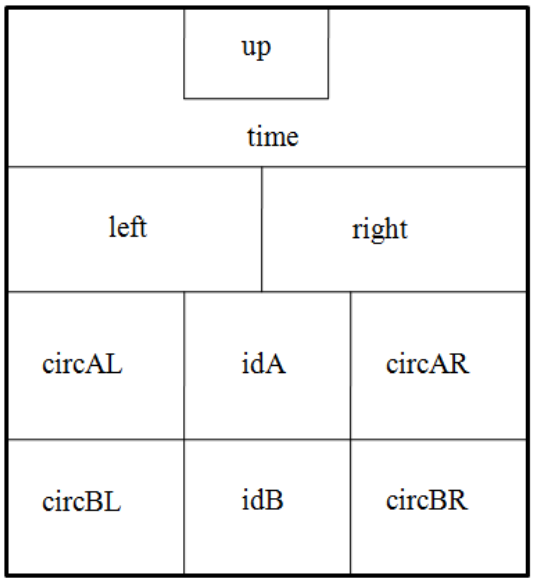

Figure 2.7: Representation of a single node

A typical binary tree for a few particles looks as shown in Fig. 2.8. The following operations are performed on a binary tree:

- finding the earliest event
- add a new event
- delete unwanted events
- create new events

A pool of nodes is maintained. The deleted events are stored in an event pool and new events are created by retrieving the nodes from the event pool. Hence at each loop a check has to be made to ensure that the event pool is not empty. The binary tree fluctuates in size as the simulation progresses. The algorithm given by Rapaport (1980) allows efficient modification (during cell crossing and wall-particle collision) and deletion (during particle-particle collision) of nodes. It give a computational efficiency of $2ln(N) + O(1)$ which is close to $log_2(N)$.

Basic functions of the program

There are two different structures which are used in this procedure. The entire simulation revolves around modifying relevant nodes in every step. The event calendar which maintains the sequence of events is made up of nodes interconnected with pointers to form a binary tree. Each node is represented by a structure *Evtree* which holds information of the type of event the partners involved and the time of event. The position, velocity and time of each particle stored in the structure *Mol* The following operations are the basic units of the simulation algorithm:

1. Setparams: Calculates the dimensions of the system, number of particles, number of cells and dimension of each cell.
2. Initcoords: Initializes the particle positions and ensures that they do not overlap.

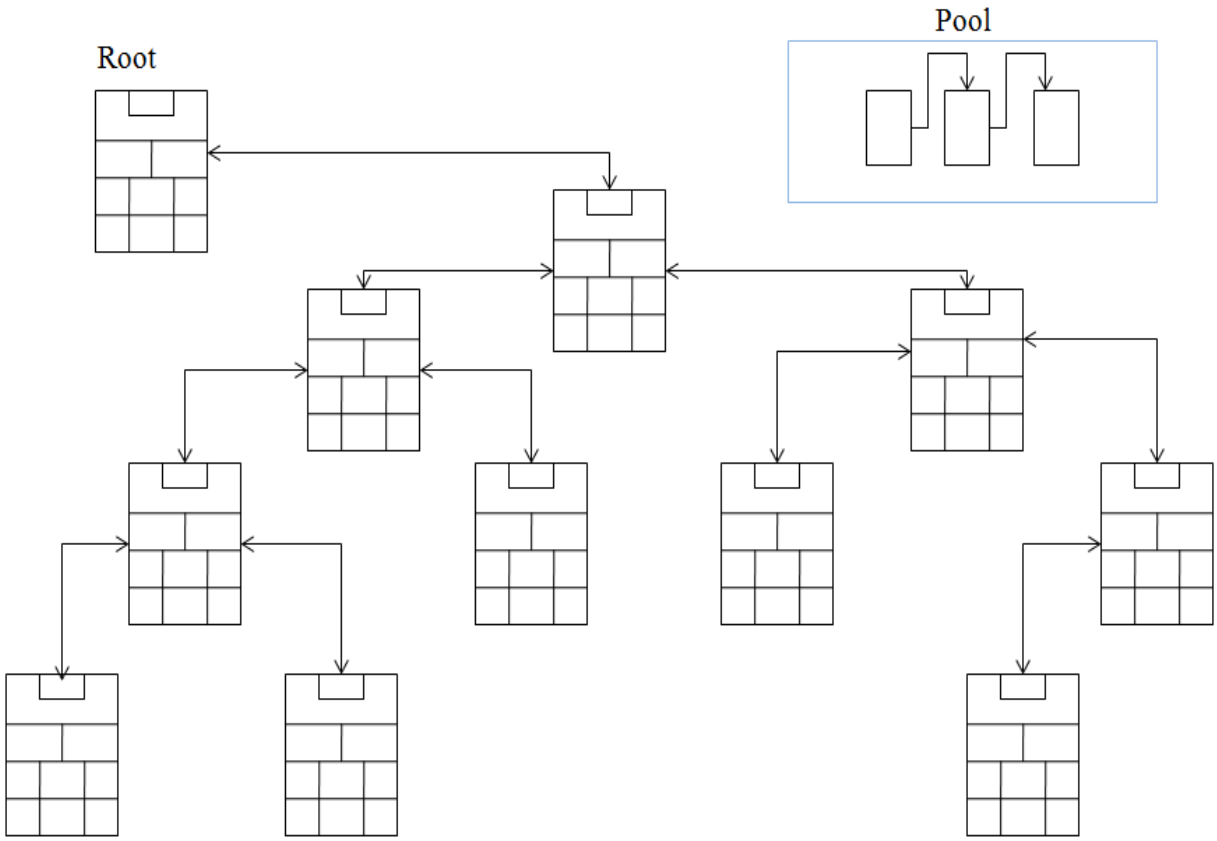

Figure 2.8: Representation of a binary tree

3. Initvels: Initializes the particle velocity in all directions using random number generator function

4. PredictEvent: Predicts the future boundary crossing, wall-particle collision and particle-particle collisions taking into account the periodic boundary condition.

5. ScheduleEvent: Inserts an event node at the correct location in the event calendar and links it to the circular linked lists. Each time a node is taken from the pool it checks if the event pool is empty.

6. NextEvent: Searches for immediate future event.

7. DeleteEvent: Once the immediate future event is found the node becomes invalids. DeleteEvent recognizes these nodes.

8. DeleteAllMolEvents: It deletes all the nodes which are linked to the previous events as they are no longer valid. It also restructures the broken branches of the binary tree.

9. InitEventList: Initializes the first set of nodes in the event calendar.

10. Single Event: Once the future event is predicted, a variable called MOL_LIMIT is set to a known integer - say 1000000 for collision, >1000000 for boundary crossing and wall-particle collision and 1000006 for updating the whole system. Single event reads this variable and ensures that the proper event is processed.

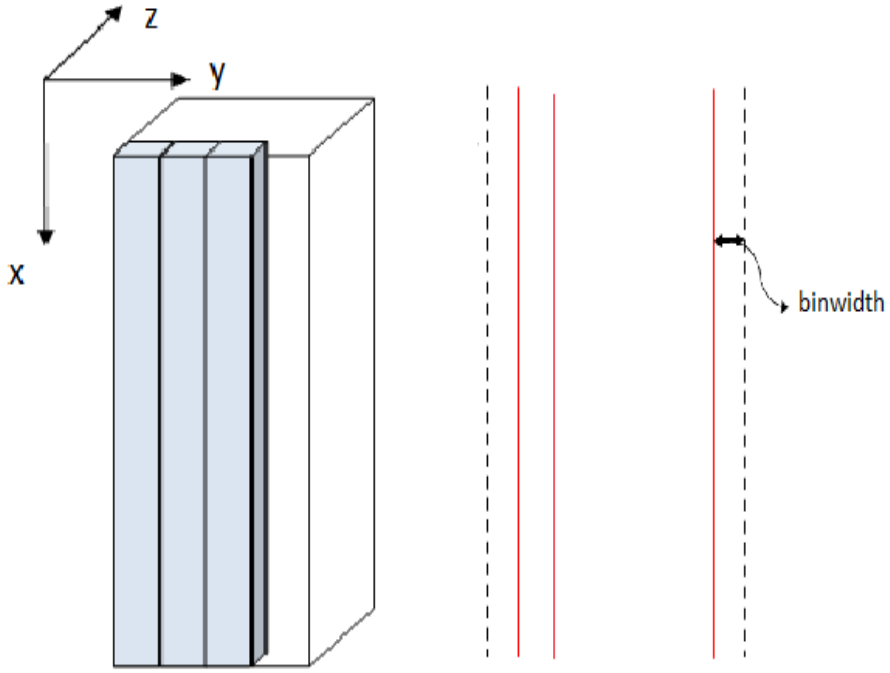

Figure 2.9: Schematic of 3D and 2D bins

2.5 Calculation of macroscopic properties

The gravity acts in the positive x-direction and the walls are present the y-direction. As the quantities change along the direction of the wall, we divide the system in vertical bins as shown in Fig. 2.9. Within each bin, the macroscopic properties of all particles are assumed to be almost constant. The width (w) of each bin is set as per a thumb rule given by -

$$d < w < 2d. \tag{2.22}$$

The simulations are run for N*30000 collisions. The average kinetic energy [E(t)] initially varies but later reaches a steady state in case of dissipative systems. The macroscopic properties like granular temperature (T), stream-wise velocity (U_{xa}), volume fraction (ν) are calculated by averaging the microscopic properties once the system reaches a steady state. It is to be noted that mean square energy term is inversely propotional to $\sqrt{N}$. Thus, the fluctuations can be reduced by increasing the number of particles. The mean properties for 2D simulations are obtained by:

$$u_i(t) = c_i(t) - U_x(y_i, t) \tag{2.23}$$

$$U_x(y_i, t) = \frac{1}{N_y}\sum_{i=1}^{N} c_i(t)\delta(y - y_i) \tag{2.24}$$

$$U_x(y) = \langle U_x(y_i, t)\rangle \tag{2.25}$$

$$\nu(y) = \frac{\pi d^2}{4}\Big\langle \frac{1}{A_y N_y}\sum_{i=1}^{N}\delta(y - y_i)\Big\rangle \tag{2.26}$$

$$T(y) = \Big\langle \frac{1}{2N_y}\sum_{i=1}^{N} u_i(t)u_i(y)\delta(y - y_i)\Big\rangle \tag{2.27}$$

$$E = \frac{1}{2N}\sum_{i=1}^{N} U_{\alpha i}^2 \tag{2.28}$$

The mean properties for 3D simulations are obtained by dividing the simulation domain in x and z-direction into columns (Fig. 2.9) and the macroscopic properties are calculated by the below formula :

$$u_i(t) = c_i(t) - U_{xz}(y_i, z_i, t) \tag{2.29}$$

$$U_{xz}(y_i, z_i, t) = \frac{1}{N_y}\sum_{i=1}^{N} c_i(t)\delta(y - y_i)\delta(z - z_i) \tag{2.30}$$

$$U_{xz}(y, z) = \langle U_{xz}(y_i, z_i, t)\rangle \tag{2.31}$$

$$\nu(y, z) = \frac{\pi d^3}{6}\Big\langle \frac{1}{V_{yz} N_{yz}}\sum_{i=1}^{N}\delta(y - y_i)\delta(z - z_i)\Big\rangle \tag{2.32}$$

$$T(y, z) = \Big\langle \frac{1}{2N_{yz}}\sum_{i=1}^{N} u_i(t)u_i(t)\delta(y - y_i)\delta(z - z_i)\Big\rangle \tag{2.33}$$

$$E = \frac{1}{3N}\sum_{i=1}^{N} U_{\alpha i}^2 \tag{2.34}$$

where E is the average kinetic energy, c_i is the instantaneous velocity, u_i is the fluctuating velocity, A_y is area of single bin and V_{xz} is the volume of one bin. The angular brackets represent average over time.

2.6 Validation of the code

The code was compared with the results published by Alam & Chikkadi (2010). The average kinetic energy versus time is plotted in Fig. 2.10 for volume fraction ν=0.565, e_n=0.99, β_w=-0.9, W/d=31.0, L/W=1.3 and number of particles N=900. The results from the code based on Rapaport (2004) algorithm agrees with published results within an error margin of 0.1%.

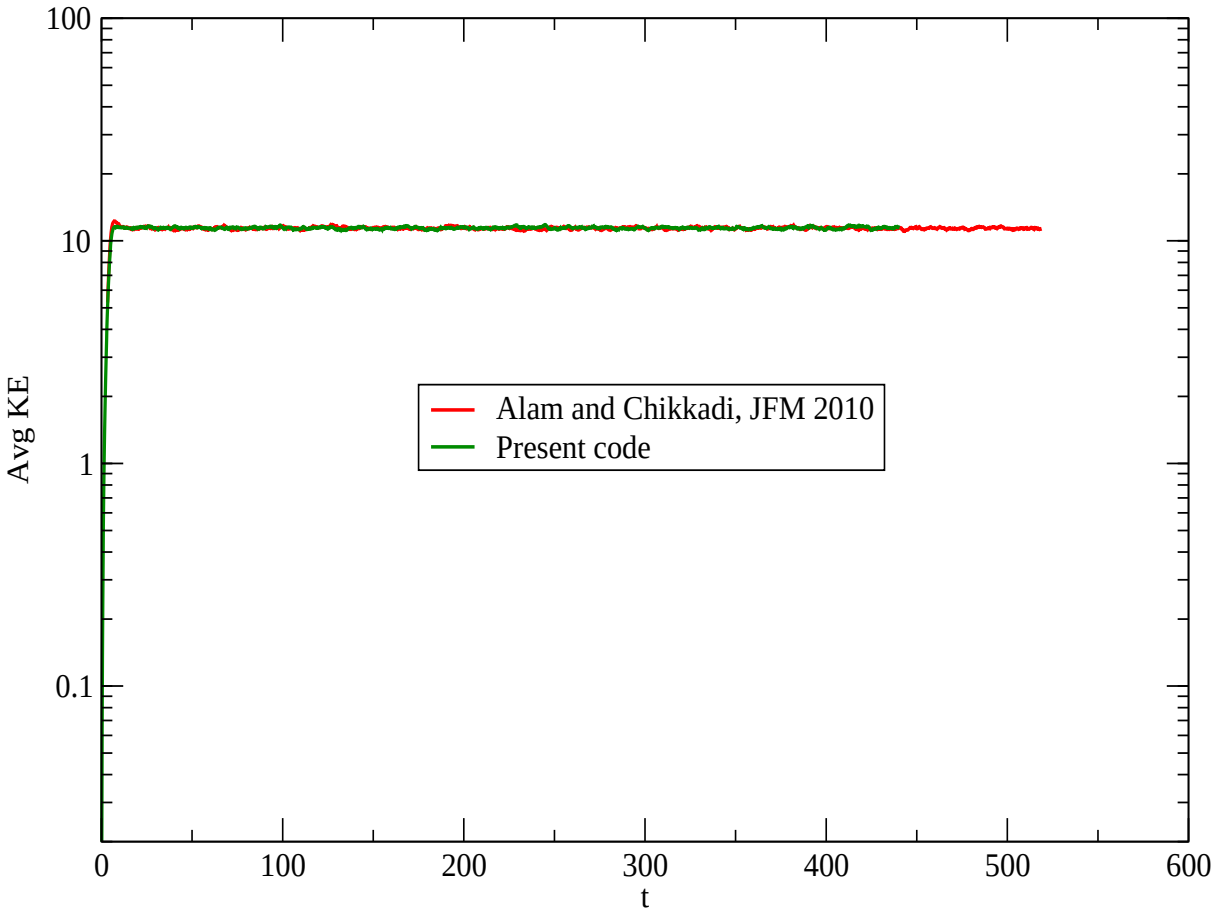

Figure 2.10: Average kinetic energy (E(t)) Vs time (t) to validate the present code with published results for ν=0.565, e_n=0.99, β_w=-0.9, N=900, W/d=31.0, L/W=1.3.

Chapter 3

Mean fields and velocity distribution function

Velocity distribution function (VDF) obeying the Boltzmann equation has been studied theoretically for inelastic hard spheres by Esipov & Pöschel (1997). van Noije & Ernst (1998) calculated the VDF for heated hard spheres by solving Enskog-Boltzmann equation using Sonine polynomial expansion. It was found that the distribution function goes as $\sim exp(-Ac^{3/2})$ where A$\sim 1/sqrt(\epsilon)$, with ϵ being the inelasticity and c the normalized velocity. The validity of these results was further discussed by Brey *et al.* (1999) and specifically for the high energy tails by Moon *et al.* (2001). VDF has been studied in detail for vibrated granular matter by Brey & Ruiz-Montero (2003) and Moon *et al.* (2004). Rouyer & Menon (2000) carried out experiments with inelastic spheres in between two horizontal Plexiglas plates vibrated in vertical direction and found an expression for VDF as $P(v) = C\exp^{(-\gamma(|u|/\sigma)^{\alpha})}$ where α =1.55±0.1. Blair & Kudrolli (2001) conducted experiments for granular matter flowing along an inclined plane with energy supplied through a oscillating wall and found that the exponent $\alpha \sim 1.5$ is not always true. They found that the exponent α varies from 0.7 to 2.0. van Zon & MacKintosh (2004, 2005) did simulations for dilute granular gases subjected to boundary heating and uniform heating. They quantify the exponent depending on two parameters: (i) $q = N_H/N_c$ where N_H average number of heating events and N_C is the total number of collisions; and (ii) coefficient of restitution e_n.

In granular Poiseuille flow, the deviation of VDF from a Gaussian has been attributed to the spatial correlation by Moon *et al.* (2004), Chikkadi & Alam (2007) and Alam & Chikkadi (2010). The theoretical description for dilute Poiseuille flow is derived from Boltzmann equation and compared with Navier-Stokes equation by Tij & Santos (2004) . They found the existence of bimodality in the temperature profile. Galvin *et al.* (2007) devised a method to locate the Knudsen layer in 3-dimensional flows between two parallel plates with periodic boundary conditions applied to all other sides. All these studies show that the VDF is a Gaussian for dilute gases within the elastic limit and non-Gaussian for inelastic and dense systems.

In the present chapter we focus on understanding the mean fields and VDF in a dilute granular Poiseuille flow. In the first section, mean fields - mean velocity, temperature and volume fraction at different orders of magnitude of Knudsen number is discussed. Granular temperature bimodality and mass flow rate as a function boundary conditions and Knudsen number of the system are studied in detail. As the width of the system (W/d) is decreased the ratio of wall-particle to particle-particle collision increases leading to wall effects being visible near the channel center. In the present work simulations are done in regimes where continuum approximation is no longer valid. Velocity distribution function has been studied extensively

for varying volume fraction, normal restitution coefficient and wall restitution coefficient for granular Poiseuille flow by Alam & Chikkadi (2010) and Chikkadi & Alam (2007). In the above works, the effect of Knudsen number is studied by varying the density of the system. In the present work, the density of the system is set to a constant value and the Knudsen number is varied by varying the width of the channel. An attempt is made to explain the high energy tails of velocity distribution functions in dilute granular flows in a way similar to the work done by van Zon & MacKintosh (2005).

3.1 Knudsen number and flow regimes

Knudsen number It is the ratio of mean free path (λ) to the width of the channel (W).

$$Kn = \frac{\lambda}{W} \tag{3.1}$$

Flow regimes can be classified based on the Knudsen number as follows Karniadakis *et al.* (2005):

- Kn $\leq 10^{-2}$, continuum regime
- 10^{-2} < Kn<0.1, slip flow regime
- 0.1 < Kn < 10, transition flow regime
- Kn $\geq$ O(10), free molecular regime.

In all simulations in this chapter the length of the system is kept constant (L/d=500) and the width of the system(W/d) is varied to get results for different Knudsen number.

Volume fraction

It is defined as the ratio of the volume occupied by the spheres to the volume of the system, given by

$$\vartheta = \frac{\pi d^2 N}{4L * W} \tag{3.2}$$

where N is the number of particles, d is the diameter of the particle.

For most of the simulations in this chapter the volume fraction is set to 0.01 that corresponds to a dilute flow. The effect of varying density on the mass flow rate and the temperature bimodality is also assessed.

3.2 Mean fields and other quantities

Granular temperature, mean velocity and the volume fraction are calculated by the method described in Sec. 2.28. Figure 3.1 shows the mean fields versus position of the bin for different orders of Knudsen number at e_n=0.99, e_w=1.0 and β_w=-0.5. The volume fraction is set to ν=0.01 which approximately fixes the mean free path of the system. The width (W/d) of the channel is decreased to increase the Knudsen number. The number of bins is set according to a thumb-rule given in Eq. 2.22. The mean properties are averaged once the system reaches a steady state. In general the properties are calculated over at least N*5000 collisions. Table 3.1 gives details about the system parameters used to obtain the mean fields in different regimes.

Order of Knudsen Number	L/W	N	Knudsen number	Number of bins
O(1)	0.0608	200	1.204	25
O(0.1)	0.782	2500	0.101	300
O(0.01)	3.14	10000	0.039	1000

Table 3.1: Parameters used in simulations for different orders of Knudsen number.

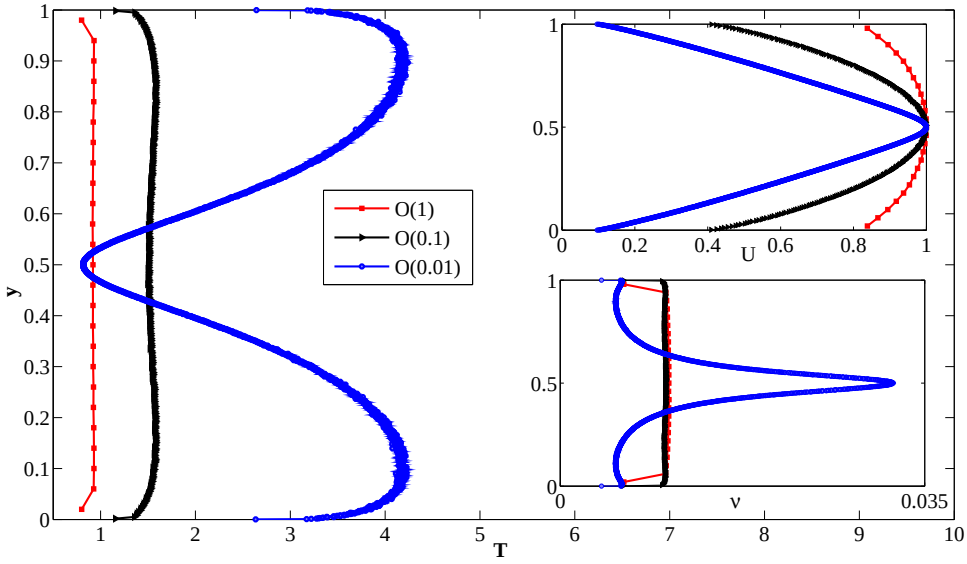

Figure 3.1: Granular temperature (T) (main panel), mean stream-wise velocity (U) (top inset) and volume fraction (ν) (bottom inset) versus position at different orders of Knudsen number for e_n=0.99, β_w=-0.5.

As seen in Fig. 3.1, the temperature profile is bimodal and it is pronounced for Knudsen number of O(0.01). The granular temperature is studied more rigorously in the next section. The density profile shown in the lower inset of Fig. 3.1 shows inverse behavior of granular temperature. The density profile is peaked at the center of the channel for Kn $\sim$ O(0.01) which indicates accumulation of particles at the center of the system, unlike that of Kn $\sim$ O(0.1) and Kn $\sim$ O(1). The ratio of wall-particle to particle-particle collision increases in case of higher Knudsen number flows which in turn leads to homogeneous system. However, significant clustering at the center of the system is seen in lower Knudsen flows. Lower Knudsen number implies larger width of the channel. Hence, the effect of the wall is not felt near the center of the system. On examining the velocity profile shown in the top inset of Fig. 3.1, we see that the slip near the wall increases as the Knudsen number is increased. The velocity profile is sharper for Kn $\sim$ O(0.01). The slip velocity and wall temperature details will be dealt in detail in Chapter 4.

3.2.1 Mass flow rate versus Knudsen number

The length of the system is kept constant for all simulations at a given density, and the width is varied to calculate the mass flow rate at different orders of Knudsen number. The length (L/d) of the system is 500.0, 200.0 and 60.0 for ν = 0.01, 0.1, 0.3, respectively.

The plots of Knudsen number versus mass flow rate for varying wall roughness (β_w) for ν=0.01, 0.1 and 0.3 are shown in Figs. 3.2, 3.3 and 3.4, respectively. The mass flow rate is calculated as:

$$Q = \frac{\int \nu U dy}{\bar{\nu} g^{\frac{1}{2}} W^{\frac{3}{2}}}, \tag{3.3}$$

which has been made dimensionless.

The perfectly rough walls corresponding to β_w=1.0 has the lowest mass flow rate (Q) at all volume fractions. The denser systems have relatively higher mass flow rates for a given Knudsen number and wall restitution coefficient. This is because higher density implies increased particle-particle interactions compared to wall-particle interactions, leading to increased clustering at the center and hence larger mass flow rates. It is observed that Knudsen number decreases with increase in density of the system for a fixed width (W/d) of the system.

For a fixed width of the channel, both the Knudsen number and mass flow rate increase with the change in β_w from 1.0 to -1.0 (i.e with decreasing wall roughness). The plots corresponding to $\beta_w \geq 0.0$ (Figs. 3.2a, 3.3a, 3.4a) show that the flow rate decreases in a similar fashion for all positive values of wall restitution coefficient. The wall roughness, which is corresponds to $-1.0 < \beta_w < 0.0$, yields results which are non-monotonous with Knudsen number. The flows with high-slip show a drastic increase in the mass flow rate. The high-slip walls tend to align the particles which collide with the wall along the direction of gravity which in turn increases the mass flow rate. The same is seen from Figs. 3.2b, 3.3b and 3.4b. The mass flow rate, particularly for $\beta_w > -0.9$, decreases rapidly for Kn $\sim$ O(0.01), becomes flatter at Kn $\sim$ O(0.1) but later decreases faster for Kn > 1.

At lower Knudsen numbers (Kn < 0.01) the particle-particle collisions become important but as the width is decreased in order to span higher Knudsen regimes the wall-particle collisions dominate. The dense flows in narrow channels lead to Kn decrease below 0.01 as seen in Fig. 3.4b. For this case, the flow rate decreases with the decrease in Knudsen number below Kn $\sim$ 0.005.

A schematic of the Knudsen-paradox predicted by Knudsen (1909); Toschi & Succi (2005); Dongari *et al.* (2009); Taheri & Struchtrup (2012) is shown in Fig. 3.5. Results which predicted Knudsen paradox were done by considering a mixture of reflection and bounce-back [Succi (2002)], implementing isothermal wall [Taheri & Struchtrup (2012)] or by considering that the particles loose their memory once they hit the the wall and the outgoing particles velocities are random. These boundary conditions are not realistic for granular flows. Thus, by comparing our results with Fig. 3.5, we find that Knudsen-paradox is absent in a dilute granular Poiseuille flow.

3.2.2 Bimodality of granular temperature

Rarefied gas flow between two plates has shown a deviation in the general hydrodynamics when it comes to the temperature profile. Mansour *et al.* (1997) was one of the first to simulate dilute Poiseuille flow for elastic Maxwellian molecules and reported the clear presence of bimodality in the temperature at a Knudsen number as low as 0.01. Aoki *et al.* (2002) did asymptotic analysis for rarefied flows in low Knudsen regimes, and numerical analysis for intermediate

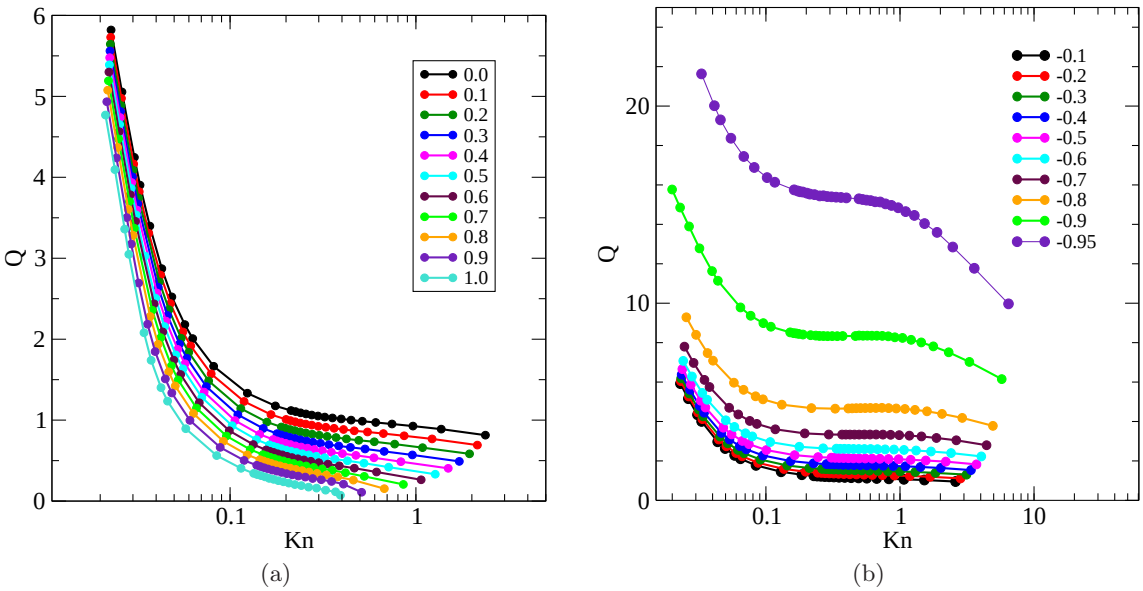

(a) (b)

Figure 3.2: Plot of mass flow rate (Q) as a function of Knudsen number for (a) $\beta_w \geq 0.0$ (b) $\beta_w < 0.0$. The parameters are e_n=0.99, L/d=500.0, ν=0.01.

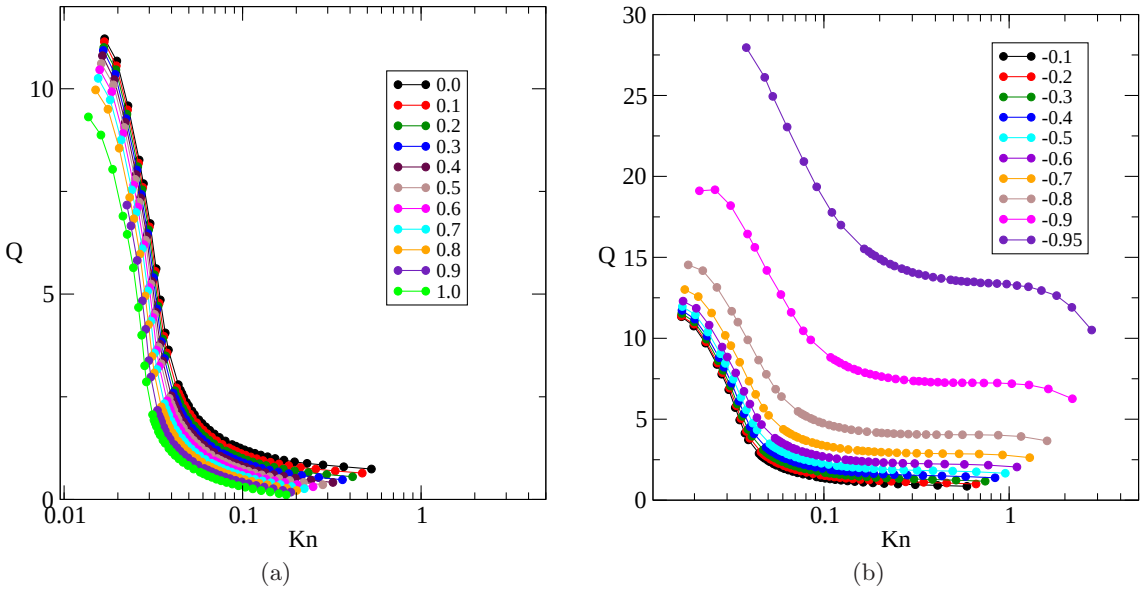

(a) (b)

Figure 3.3: Plot of mass flow rate (Q) as a function of Knudsen number for (a) $\beta_w \geq 0.0$ (b) $\beta_w < 0.0$. The parameters are e_n=0.99, L/d=200.0, ν=0.1.

and low Knudsen number flows. Tij & Santos (2004) studied the Poiseuille flow of granular particles subjected to constant gravitational force and white noise in two-dimensions in inelastic regime. The later work showed that the decrease in the normal restitution coefficient (e_n) moves the maxima seen in the granular temperature profile towards the center of the system for a given $g\lambda_0/(v_0)^2$ where λ_0 is the mean free path in the center of the system, T_0 is the granular temperature at the center of the system and g is the gravitational acceleration. This behavior reverses when e_n reduces below 0.4. They also found that the location of peaks in the granular temperature occur at $\sim$ 3 mean free paths from the center of the system for $g\lambda_0/(v_0)^2$=0.05. The ratio (T_0-T_{max})/T_0 is approximately 10 times the square of the non-dimensional number

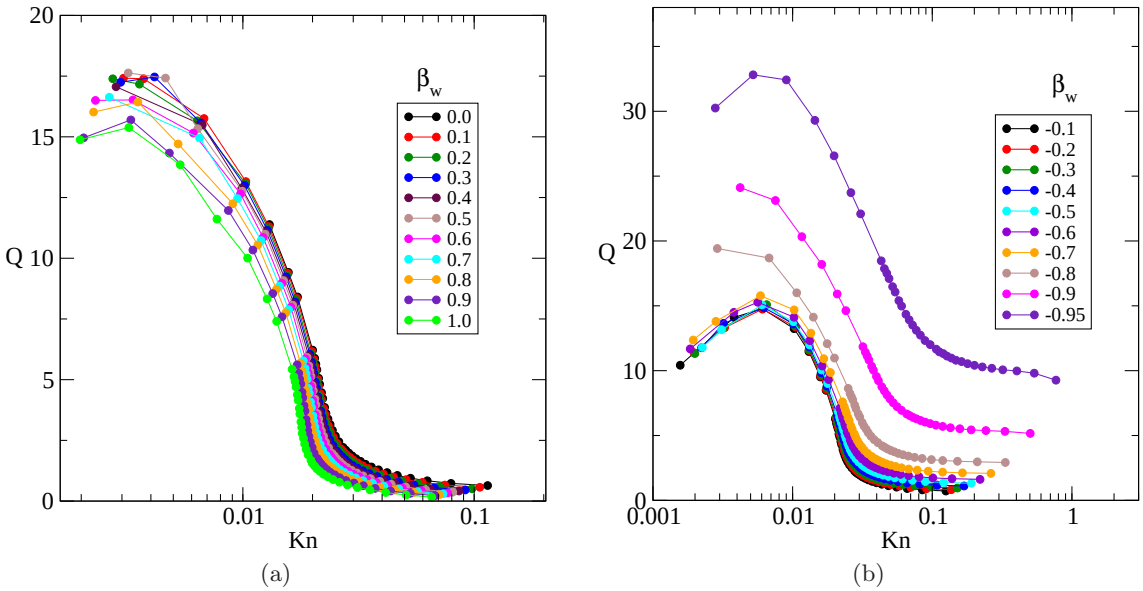

Figure 3.4: Plot of mass flow rate (Q) as a function of Knudsen number for (a) $\beta_w \geq 0.0$ (b) $\beta_w < 0.0$. The parameters are e_n=0.99, L/d=60.0, ν=0.3.

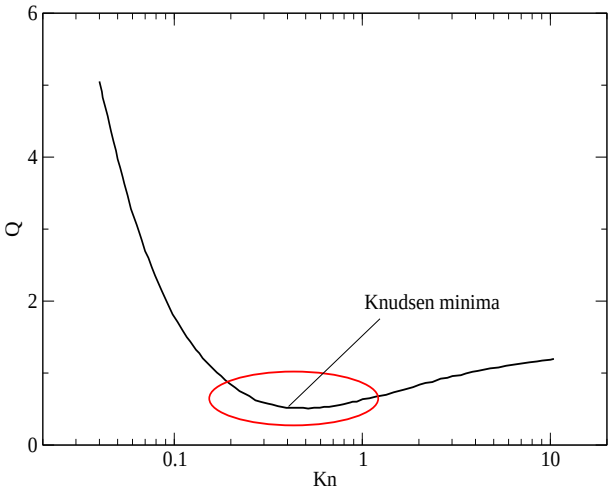

Figure 3.5: Schematic showing Knudsen paradox.

$g\lambda_0/(v_0)^2$. In this section we discuss our simulation results with reference to the theoretical work reported by Tij & Santos (2004).

Effect of restitution coefficient

The raw data of granular temperature is fluctuating and hence to smoothen the curve, running averages are taken as follows -

$$T_i = \frac{\sum_{j=i}^{i+n} T_j}{n}, \qquad y_i = \frac{\sum_{j=i}^{i+n} y_j}{n}, \tag{3.4}$$

where $n \sim 5$ to 10, which corresponds to spatial averaging over bins.

All simulations in this section are done for L:W = 2.94:1, $\beta_w = 0.0$, N = 1500.

The effects of e_n on the temperature bimodality for $\nu = 0.01$, 0.1 and 0.3 are shown in Figs. 3.6, 3.8 and 3.10, respectively. The channel widths for ν=0.01, 0.1, 0.3 are 200.0, 63.0 and

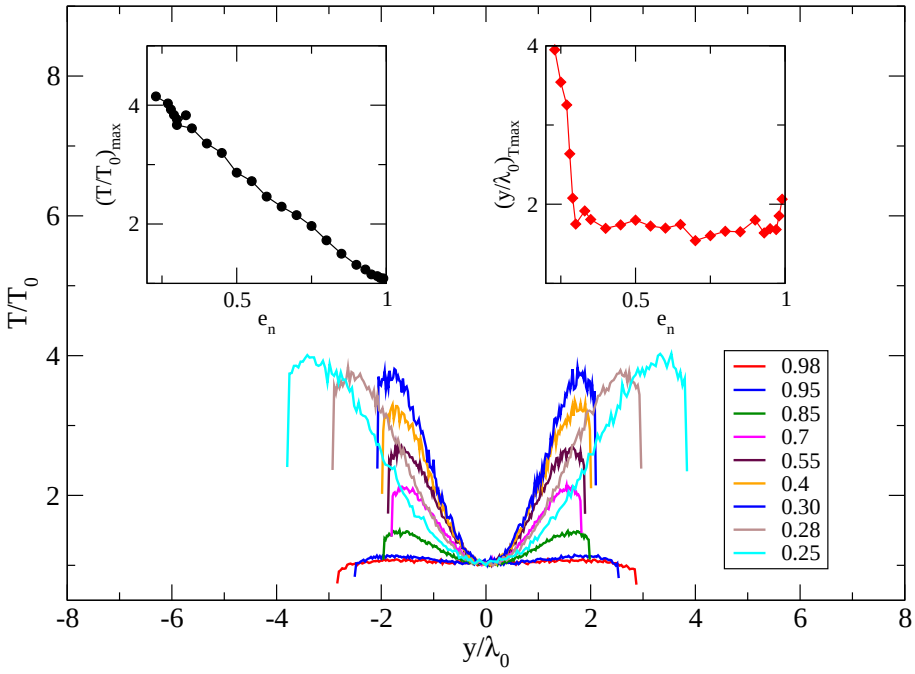

(a)

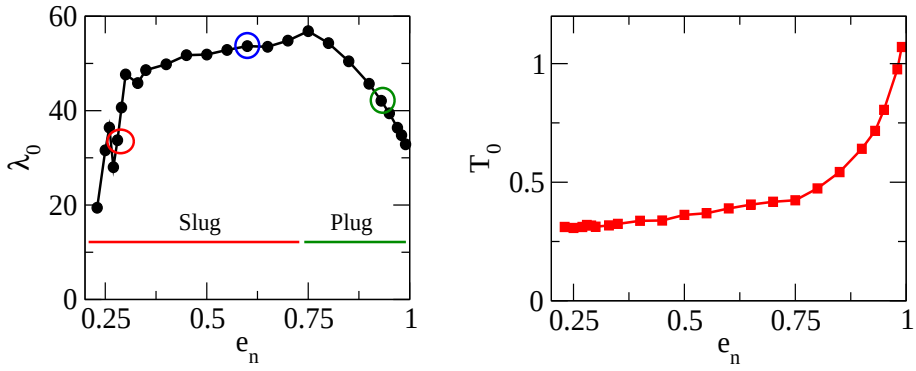

(b)

Figure 3.6: (a)Variation of granular temperature with restitution coefficient (main panel). Top left inset: Maximum temperature versus e_n. Top right inset: Position of maxima at different e_n (b) Centerline mean free path (left inset), centerline granular temperature (right inset) versus e_n for β_w=0.0, ν=0.01, L/d=589.1.0, W/d=200.0, N=1500.

36.5, respectively. The main panel in Figs. 3.6a, 3.8a and 3.10a shows the smoothened data of granular temperature for e_n ranging from nearly elastic to inelastic. The top left and right insets show the value of the peak granular temperature $[(T/T_0)_{max}]$ and the position of this peak $[(y/\lambda_0)_{Tmax})]$ as a function of e_n. The variation of centerline mean free path and granular temperature are shown in Figs. 3.6b, 3.8b and 3.10b. One cannot simulate beyond a certain inelasticity for a given system due to the problem of inelastic collapse as discussed in Chapter 2.

The bimodality becomes pronounced with the increase in inelasticity as shown in the plots of peak temperature versus e_n in top left inset of Figs. 3.6a, 3.8a, 3.10a. The top right insets indicates that the position of the bimodal peak initially decreases slightly, reaches a minima and increases further on. But beyond a certain value of e_n the position of the peaks rapidly increases.

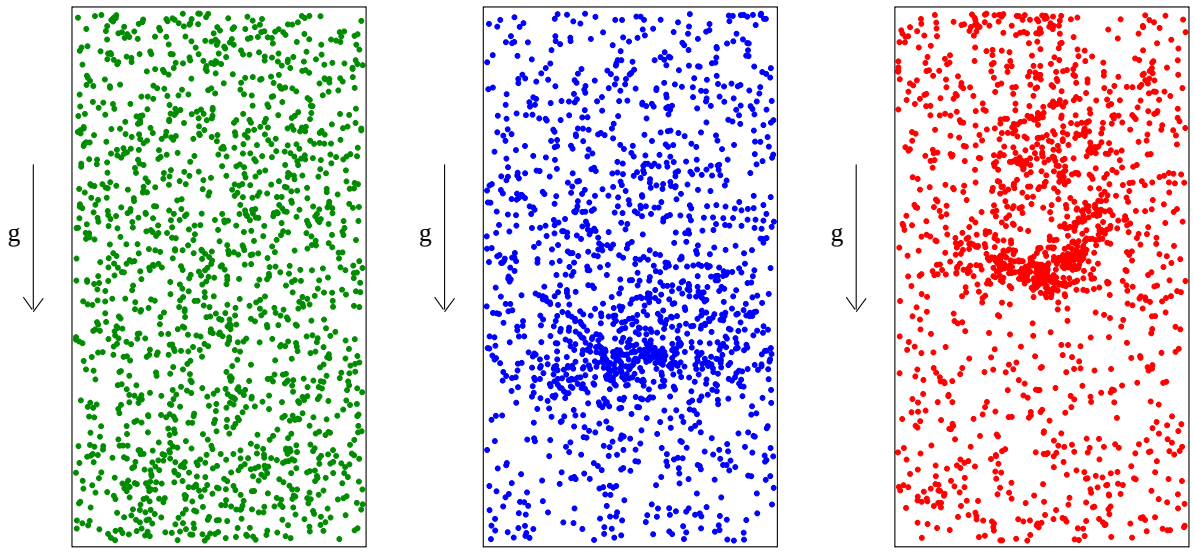

Figure 3.7: Snapshots of instantaneous particle positions for e_n=0.95 (Fig. 3.7a), e_n=0.65 (Fig. 3.7b) and e_n=0.26 (Fig. 3.7c) corresponding to Fig. 3.6.

This value of e_n is dependent on the density of the system; it appears closer to the elastic limit for denser systems. The value of e_n beyond which the bimodal peaks start moving away from the center rapidly is ∼0.3, ∼0.7 and ∼0.8 for ν = 0.01, 0.1 and 0.3, respectively. In order to understand the reasons for such anomalous behavior, a plot of λ_0 as a function of e_n is shown in the left panel of Figs. 3.6b, 3.8b and 3.10b. The centerline granular temperature (T_0) decreases sharply and the curve flattens out at lower dissipations as seen in the right panel of Figs. 3.6b, 3.8b and 3.10b. The centerline mean free path (λ_0) increases initially as e_n is decreased, reaches a maxima and decreases beyond a certain value of e_n. The plug flow and wavy structures as reported by Liss *et al.* (2002) and Alam *et al.* (2009) are seen in regions where the centerline mean free path increases. The flow transitions from plug to slug as the dissipation in the system is increased. The region where the mean free path decreases with decrease e_n represents the slug flow region. The plug and slug flow regions are marked in Figs. 3.6b, 3.8b and 3.10b. The snapshots of plug and slug flows are shown in Figs. 3.7, 3.9 and 3.11. A detailed study of plug and slug-type flows is provided in Chapter 5.

Effect of wall roughness

The granular temperature versus distance curves are smoothened as per Eq. 3.4. The effect of wall roughness (β_w) on the temperature profile is studied in Fig. 3.12. The granular temperature (T) is normalized with the centerline temperature (T_0), which is plotted against y/λ_0 where λ_0 is the centerline mean free path. The smoothened curve is shown in the main panel. It is observed from the graph that as the boundaries are made very smooth ($\beta_w \sim$ -1) or very rough ($\beta_w \sim 1$), the peaks move away from the center. Thus for easier identification of the peak most of the simulations in this section are carried on for $\beta_w \sim 0.0$.

Effect of volume fraction

Fig. 3.13 shows the variation of granular temperature at different volume fractions, for e_n=0.9 and β_w=0.0. For L/d=1000, W/d=1570.0, e_n = 0.9 and β_w= 0.0, the increase in volume fraction

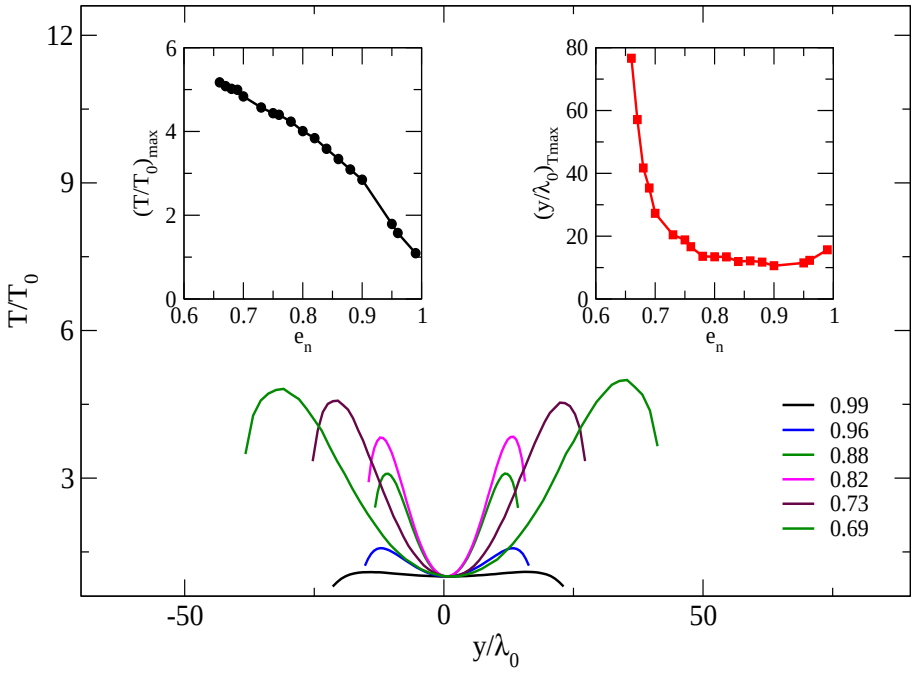

(a)

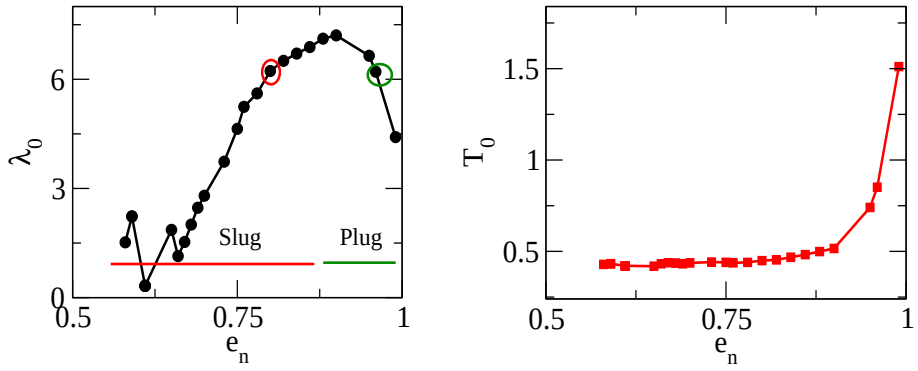

(b)

Figure 3.8: (a)Variation of granular temperature with restitution coefficient (main panel). Top left inset: Maximum temperature versus e_n. Top right inset: Position of maxima at different e_n (b) Centerline mean free path (left inset), centerline granular temperature (right inset) versus e_n for β_w=0.0, ν=0.1, L/d=187.0, W/d=63.0, N=1500.

(ν) leads to broader temperature profiles. The maximum temperature (T_{max}) along with the position of this peak (y_{max}) increases with increasing ν. The peaks for ν = 0.001, 0.002, and 0.005 appear at 2.4, 3.3 and 4.8 times the mean free path, respectively.

3.3 Velocity distribution function

Here we discuss results on VDF in a dilute ($\nu = 0.01$) granular Poiseuille flow. The goal in this section is to assess the effect of normal restitution coefficient (e_n) and the wall roughness (β_w) on VDF over different orders of Knudsen number in a dilute granular Poiseuille flow.

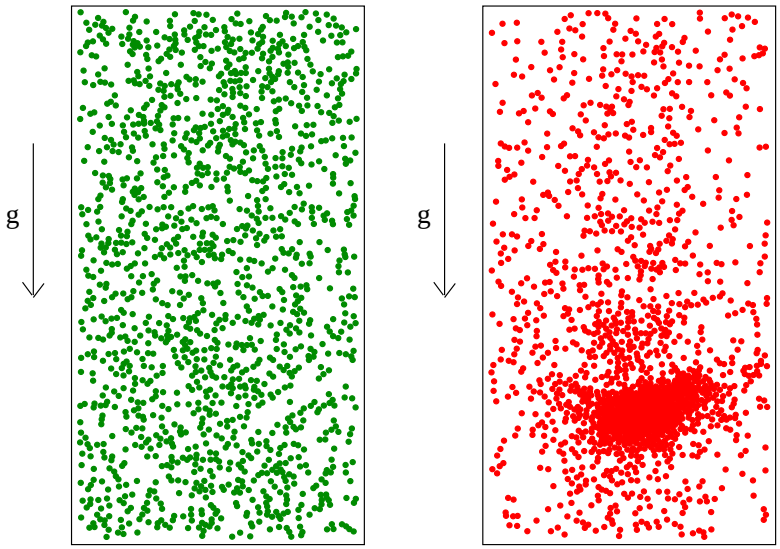

Figure 3.9: Snapshots of instantaneous particle positions for e_n=0.95 (Fig. 3.9a) and e_n=0.8 (Fig. 3.9b) corresponding to Fig. 3.8.

3.3.1 Varying normal restitution coefficients

The stream-wise mean velocity profile for Kn $\sim$ O(1), Kn $\sim$ O(0.1) and Kn $\sim$ O(0.01) are plotted for e_n = 0.99, 0.9 and 0.85 in Fig. 3.14. The velocity profiles overlap for all values of e_n for Kn $\sim$ O(1) as seen in the bottom panel of Fig. 3.14. For lower Knudsen numbers [O(0.1) and O(0.01)] the slip near the wall increases with increase in inelasticity as seen in the main and top panel of Fig. 3.14.

To understand the effects of particle-particle dissipation on the system-distribution function, wall restitution coefficient (β_w) is set to -0.9, volume fraction (ν) to 0.01, wall-particle normal restitution coefficient (e_w) to 1 and the normal restitution coefficient (e_n) is varied. This value of wall restitution coefficient β_w = -0.9 corresponds to a nearly smooth wall. The fluctuating velocity (u_i) is normalized with standard deviation ($\sigma_i = \sqrt{u_i{}^2}$). Stream-wise [$P(u_x/\sigma_x)$] and cross-stream [$P(u_y/\sigma_y)$] fluctuating velocity distribution plot for quasi-elastic limit (e_n=0.99) over different orders of Knudsen number is plotted in Fig. 3.15a and Fig. 3.15b. The y-axis is normalized by the area under the curve. The green solid is a reference to Gaussian distribution. The main panel in each the VDF plot shows the distribution in the wall bin. The upper and lower insets show the distribution at intermediate and middle bin of the system. The intermediate bin is located between the wall bin (bin=1) and the center bin. Most of the distributions tend to obey Gaussian distribution.In order to find out the behavior at high velocity, log-log plots of the VDF are shown in Fig. 3.15c and Fig. 3.15d. The data points corresponding to $|u_x|$,$|u_y|$ < 1 are ignored to calculate the exponent for the high energy tails. As the VDF seems to be symmetric, both tails are analyzed together. The scatter plots marked by open circles represent the data from the wall bin and those marked by stars are for the center bin. It is seen that the exponent $\alpha \sim 2.0$ in all middle bins. There is a minor decrease in the exponent ($\sim$ 1.84 to 1.9) for lower Knudsen number in the wall bin which is attributed to the wall roughness.

Figs. 3.16a and Fig. 3.16b show the velocity distributions for the inelastic case of e_n =

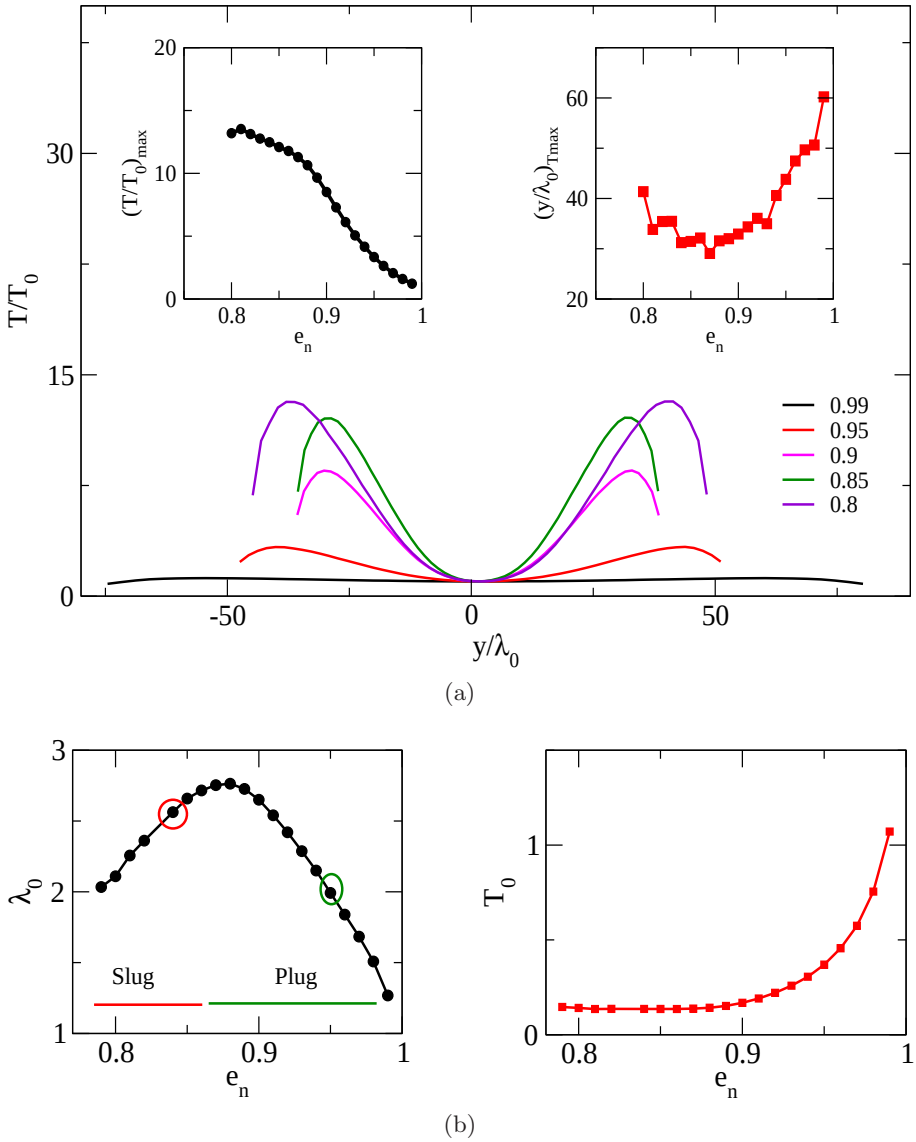

Figure 3.10: (a)Variation of granular temperature with restitution coefficient (main panel). Top left inset: Maximum temperature versus e_n. Top right inset: Position of maxima at different e_n (b) Centerline mean free path (left inset), centerline granular temperature (right inset) versus e_n for β_w=0.0, ν=0.3, L/d=107.6, W/d=36.5, N=1500.

0.9 and β = -0.9. Both distributions are shifted from the Gaussian distribution and appear to be skewed. To understand the degree of deviation from the Gaussian, the kurtosis (κ_i) and skewness (s_i) was calculated in all the bins as shown in Fig. 3.18. Kurtosis tells the peakedness of the distribution. The equation to calculate the kurtosis for a finite number of points (m) is given by:

$$\kappa_i = \frac{\sigma_{j=1}^{m}(Y_j - \bar{Y})^4}{\sigma_i^4(m-1)} \tag{3.5}$$

where σ_i is the standard deviation and $\bar{Y}$ is the mean. Kurtosis is equal to 3 for a Gaussian/normal distribution. The bin-wise kurtosis for stream-wise and cross-stream fluctuating velocity for Kn $\sim$ O(1), Kn $\sim$ O(0.1) and Kn $\sim$ O(0.01) are shown in Figs. 3.18a and 3.18b. It is seen that the κ_i is high near the channel centerline for Kn $\sim$ O(0.01) which indicates maximum

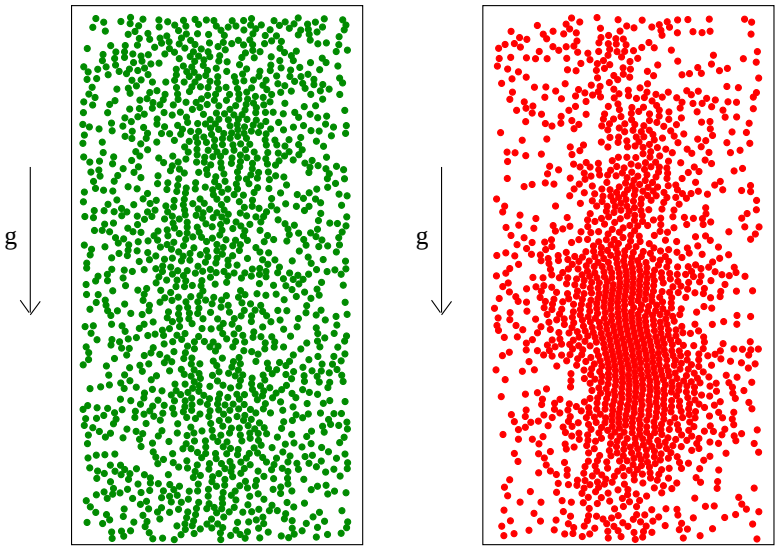

Figure 3.11: Snapshots of instantaneous particle positions for e_n=0.95 (Fig. 3.11a) and e_n=0.83 (Fig. 3.11b) corresponding to Fig. 3.10.

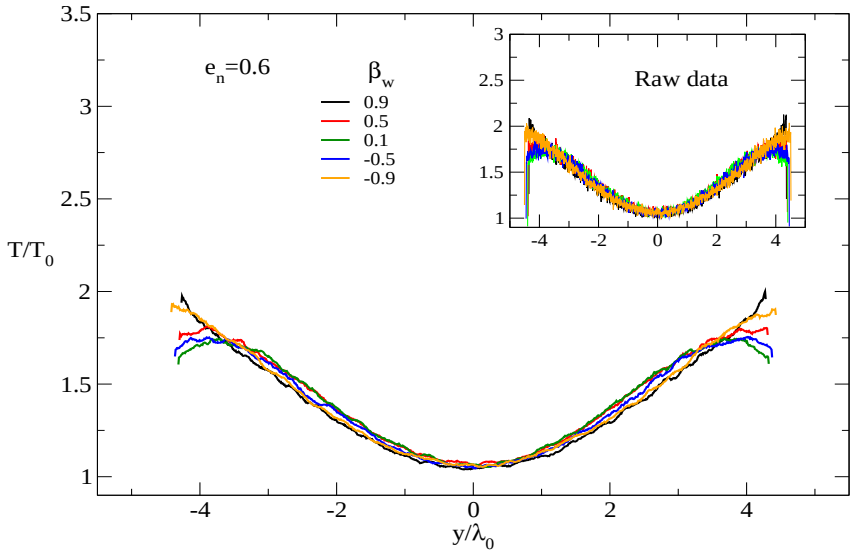

Figure 3.12: Granular temperature at varying wall restitution coefficients (β_w) for ν=0.001, e_n=0.6, W/d=1570.0, L/d=1000, N=2000. Inset indicates the raw data at different β_w. Main panel shows the smoothened values of the raw data.

peakedness in the VDF near the channel center compared to any other bin. Kurtosis is close to 3 for Kn $\sim$ O(0.1) and Kn $\sim$ O(1).

The skewness is a measure of asymmetry of the distribution. It tells how much and to which side the distribution is tilted with respect to the mean. For a given set of data points (m), skewness is given by:

$$s_i = \frac{\Sigma_{j=1}^{m}(Y_j - \bar{Y})^3}{\sigma_i^3(m-1)} \tag{3.6}$$

where σ_i is the standard deviation in the i_{th} direction and $\bar{Y}$ is the mean. The skewness is 0 for a Gaussian/normal distribution which implies that the distribution is symmetric. A negative

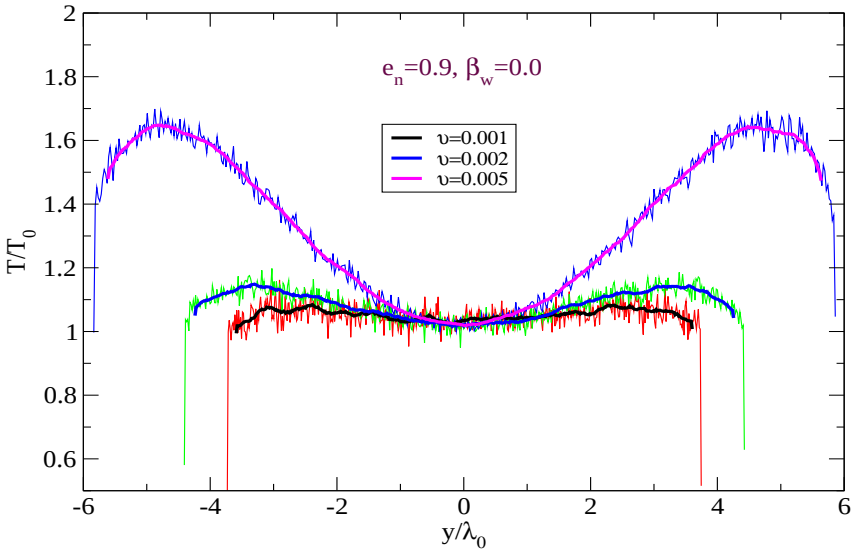

Figure 3.13: Granular temperature at varying volume fraction (ν) for β_w=0.0, e_n=0.9, W/d=1570.0, L/d=1000.

value of s_i tells that the distribution is skewed towards the left side and a positive value - towards the right. The skewness in different bins for x and y-velocity is shown in Figs. 3.18c and 3.18d. The skewness of $P(u_x)$ are all negative; it is maximum at the center of the channel for Kn $\sim$ O(0.01) which tells that the left tails are longer than the right tails. The cross-stream skewness is symmetric around the channel centerline as found previously by Alam & Chikkadi (2010). The high energy tails for both x-velocity and y-velocity for Kn $\sim$ O(0.01) clearly deviate from Gaussian distribution. The tails of the distribution follow a stretched exponential given by -

$$P(u_i) = C \exp^{[-\gamma(u_i/\sigma_i)^\alpha]} \tag{3.7}$$

The exponent α is obtained by taking a double logarithm of Eq. 3.7 as previously done by van Noije & Ernst (1998) and van Zon & MacKintosh (2005). The exponents were calculated separately for the left (Figs. 3.17a, 3.17c) and right (Figs. 3.17b, 3.17d) velocity tails as the distribution is asymmetric. The value of α is slightly higher for the positive velocity tail compared to negative fluctuation velocity tail for the x-velocity. This implies that the there is a higher probability of particles having negative fluctuating velocity. The decrease in e_n from 0.99 to 0.9 decreases the exponent from 1.3-1.4 to $\sim$1.0 in the wall bin, and from $\sim$2.0 to $\sim$1.0 in the center for Kn $\sim$ O(0.01). The value of α for higher Knudsen numbers [Kn $\sim$ O(0.1),Kn $\sim$ O(1)] remains $\sim$2.0 throughout the system, representing a Gaussian.

In the next trial (Figs. 3.19a, 3.19b) the system is made more inelastic by decreasing e_n to 0.85. The exponents of the VDF for Kn $\sim$ O(0.1) and Kn $\sim$ O(0.01) further decrease compared to e_n=0.99 and 0.9 whereas the values of the exponent for Kn $\sim$ O(1) remain almost unaffected throughout the system. The deviations of high energy tails are studied in a manner similar to Figs. 3.17a, 3.17b, 3.17c, 3.17d. The trend of the right velocity tail of $P(u_x)$ with higher exponent for inelastic case persists. It is seen that for Kn $\sim$ O(0.01) the exponent lies at around $\sim$0.85 - 0.96 for both right and left tails. The exponent α is reduced to $\sim$1.3 - 1.5 for VDFs

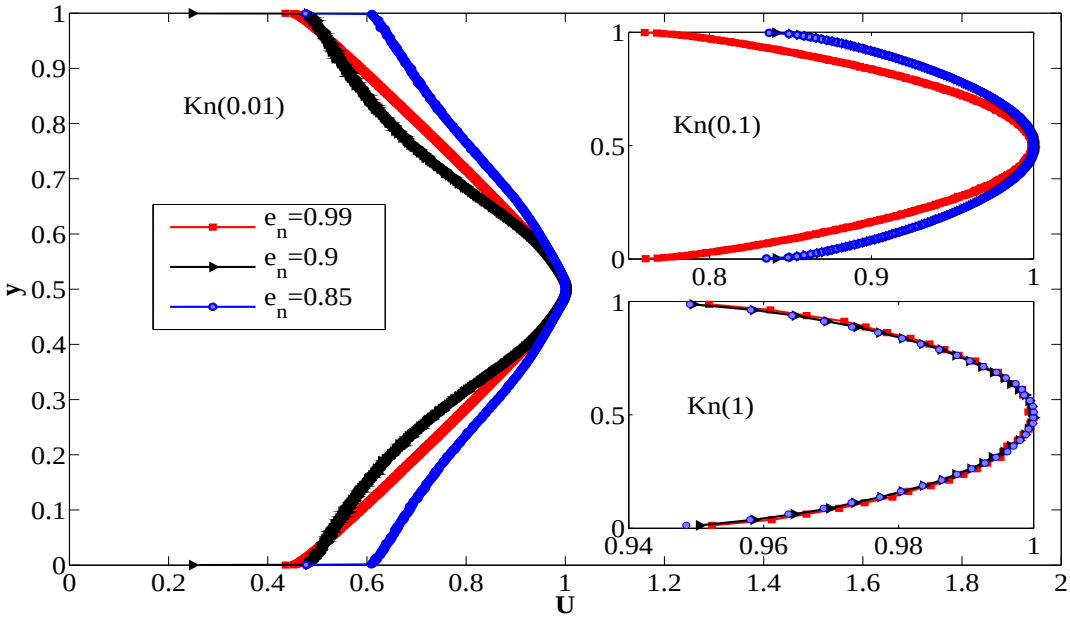

Figure 3.14: Stream-wise velocity for e_n=0.99 (red line); e_n=0.9 (black line); e_n=0.85 (blue line) for Kn $\sim$ O(1) (bottom inset), Kn $\sim$ O(0.1) (top inset), Kn $\sim$ O(0.01) (main panel).

throughout the system for Kn $\sim$ O(0.1).

Thus we can conclude that the exponent α $\sim$2.0 for quasi-elastic system (e_n=0.99) for all orders of magnitude of Knudsen. It decreases with decrease in Knudsen number for inelastic system and also with values of e_n. In other words the distribution becomes broader with decrease in Knudsen number. The asymmetric tails cannot be expressed in terms of a single exponent and hence are studied separately. The high velocity tails for positive velocities have higher exponent than negative velocities for x-velocity. The difference between the exponents of the right and the left tail proportionally increases with the decrease in e_n.

3.3.2 Varying wall restitution coefficients

With the increase in Knudsen number, the wall roughness (β_w) becomes increasingly important. This is because a higher Knudsen number implies lesser W/d which leads to an increase in the ratio of wall-particle to particle-particle collisions. In this section we probe the effect of wall roughness ($\beta_w \leq 0.0$) on the VDF for varying Knudsen number. In order to understand the effect of wall roughness on the system the normal restitution coefficient(e_n) for particles is set to 0.99, the wall-particle normal restitution coefficient (e_w) to 1 and the wall-particle tangential restitution coefficient is varied. The wall restitution coefficient close to no slip boundary condition causes some amount of back flow of particles resulting in reduction of mean free path of particles. This is why we cannot span all three orders of magnitude of Knudsen number (1, 0.1 and 0.01) for very rough walls ($\beta_w \sim 1$).

The plots for velocity distribution at ν=0.01 and for a smoothness β=-0.9 for different orders

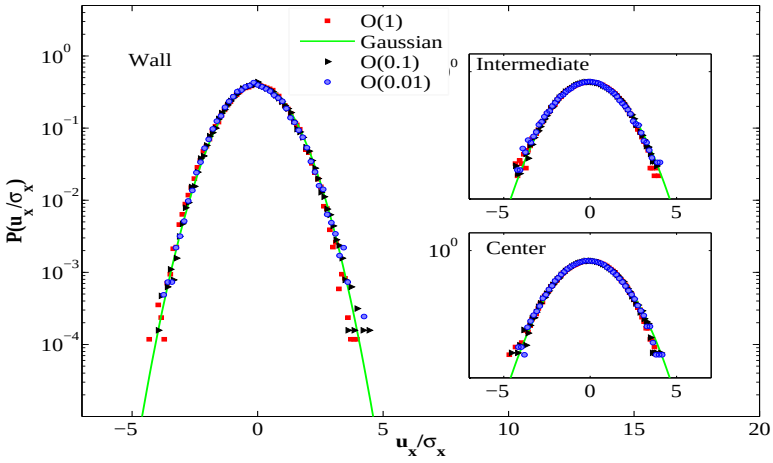

(a)

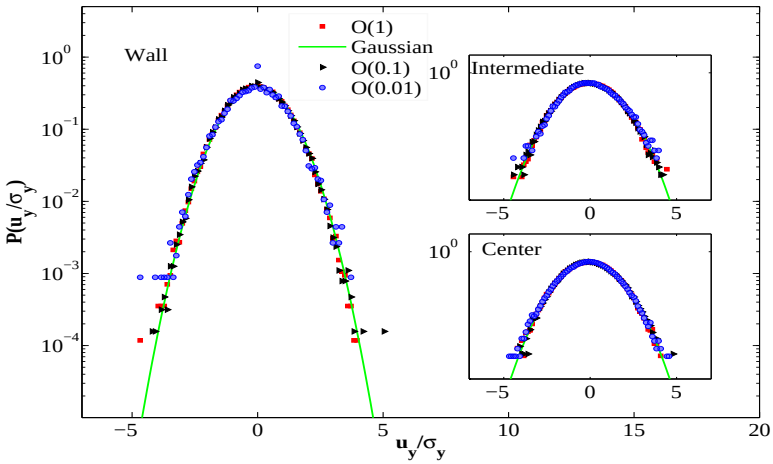

(b)

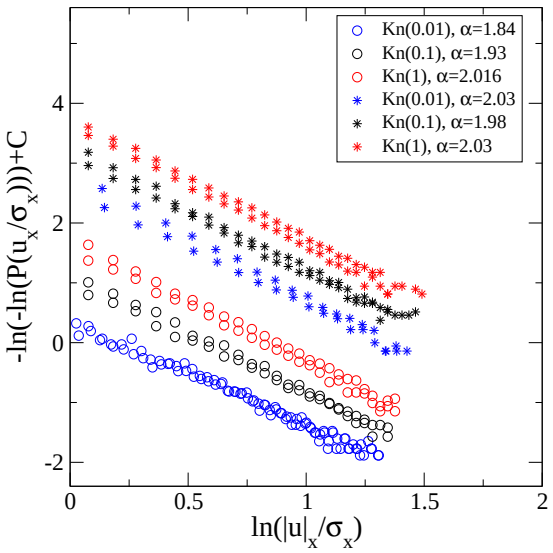

(c)

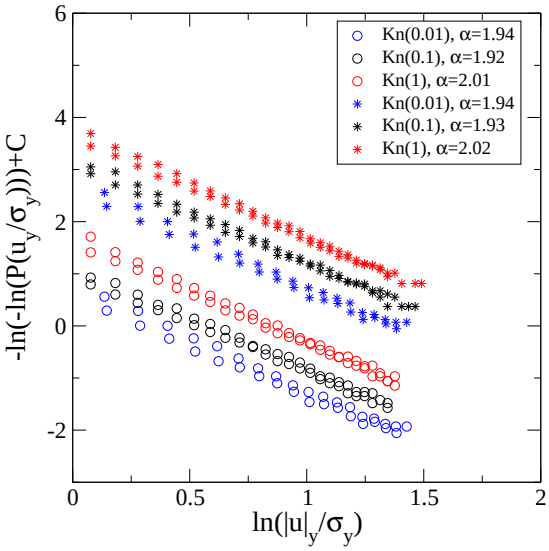

(d)

Figure 3.15: Probability distribution of u_x (a) and u_y (b) fluctuating velocities in wall bin (main panel), intermediate bin (top inset) and center bin (bottom inset). Logarithmic plot for u_x (c) and u_y (d) velocity distribution tail in the center bin (marked in open circles) and wall bin (marked in stars) for e_n=0.99, β=-0.9, ν=0.01.

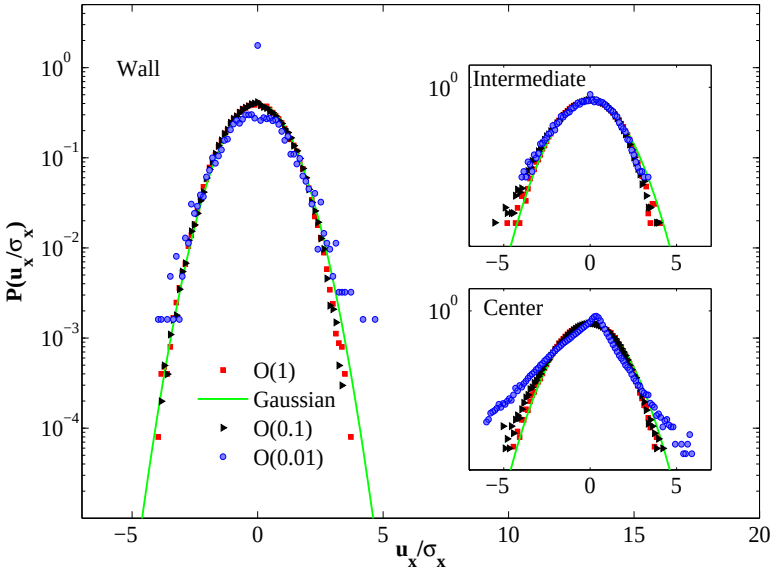

(a) Stream-wise velocity(u_x) distribution function

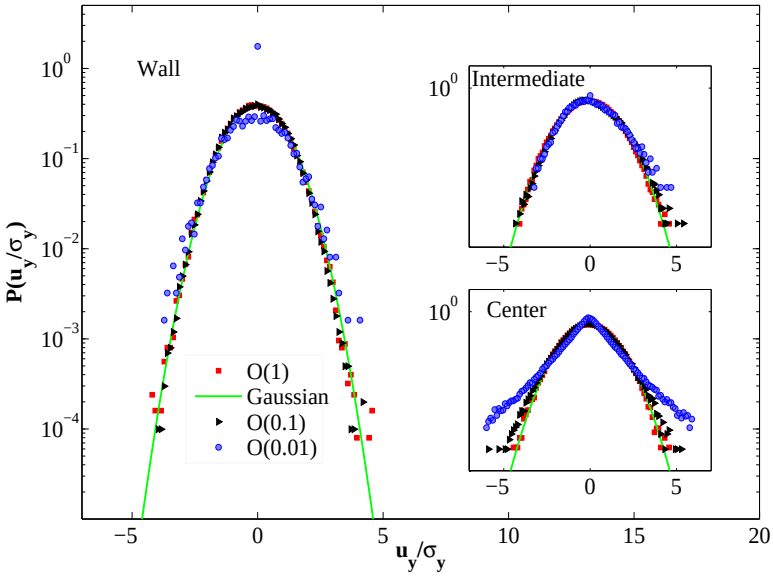

(b) Cross-stream velocity(u_y) distribution function

Figure 3.16: Probability distribution of u_x (a) and u_y (b) fluctuating velocities for e_n=0.90, β=-0.9, ν=0.01 in wall bin (main panel), intermediate bin (top inset) and center bin (bottom inset).

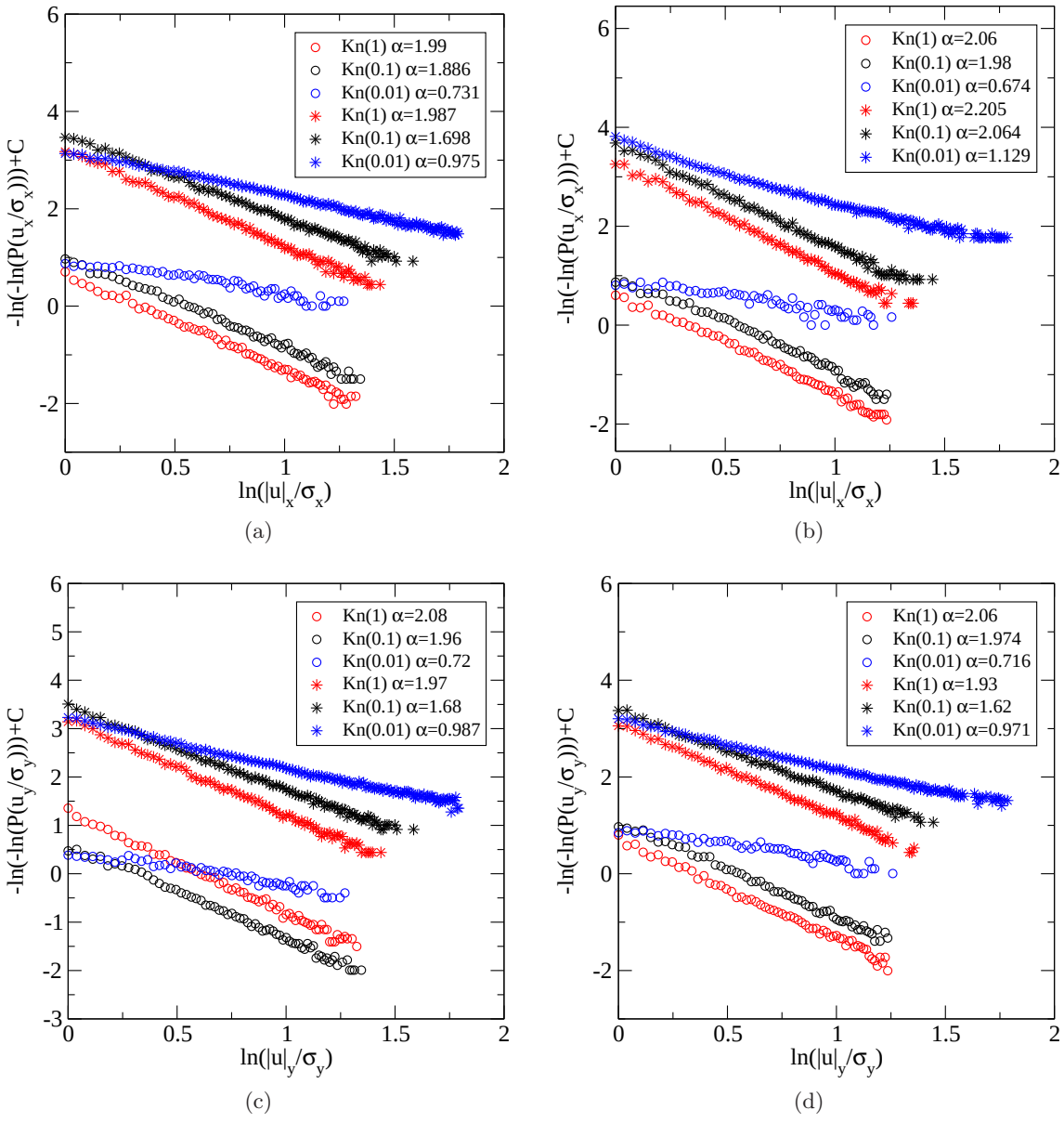

Figure 3.17: Logarithmic plots of negative u_x (a) and u_y (c) velocity tails. Logarithmic plots of positive u_x (b) and u_y (d) velocity tails for e_n=0.9, β=-0.9, ν=0.01. Open circles and stars represent the values in center and wall bin, respectively.

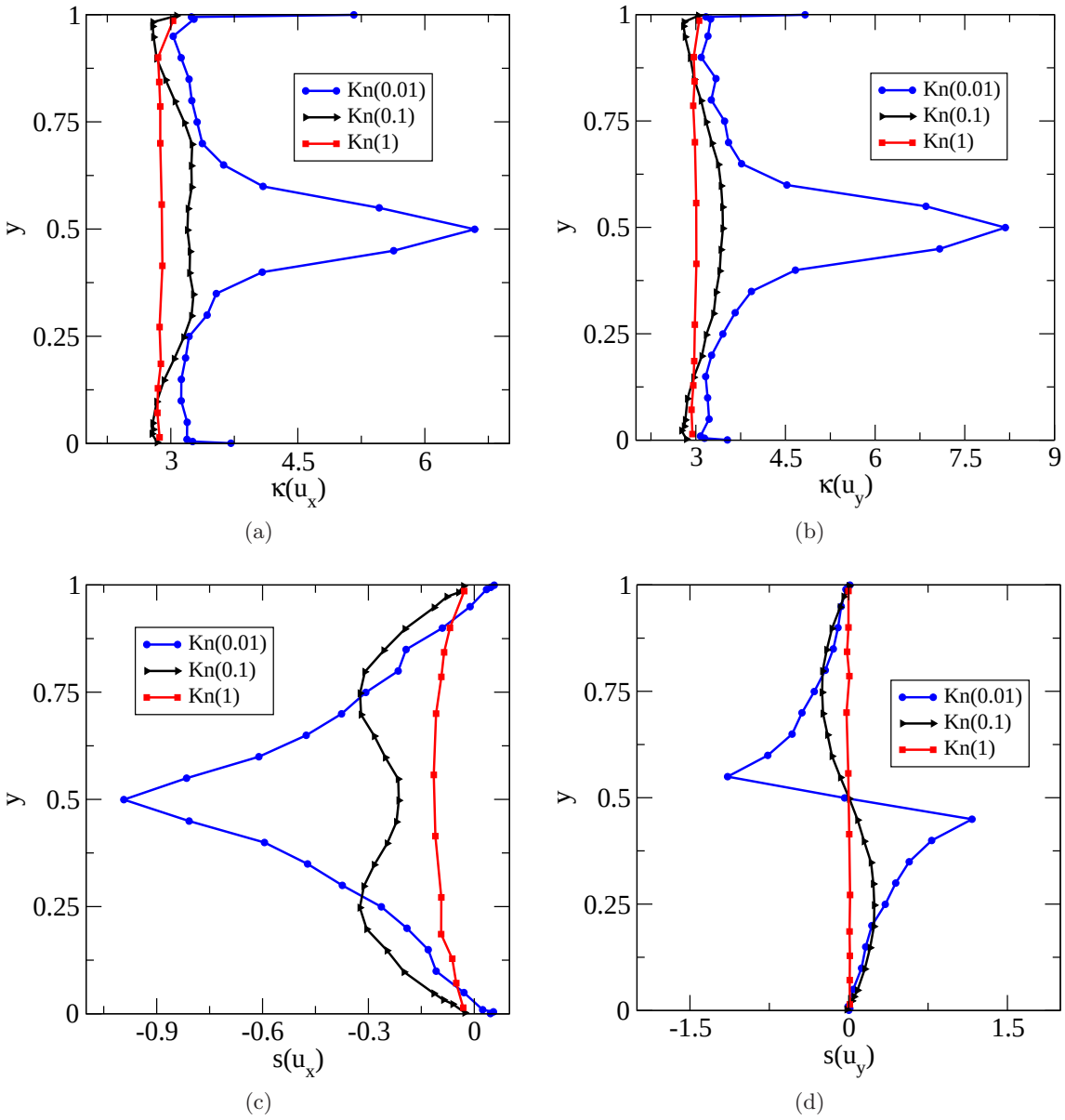

Figure 3.18: Kurtosis (a, b)and skewness (c, d) of u_x and u_y velocities, respectively for e_n=0.9, β=-0.9, ν=0.01.

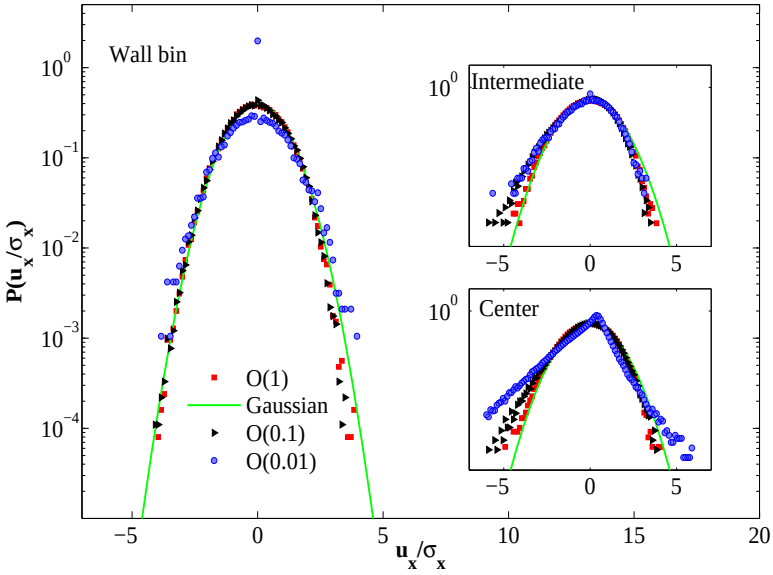

(a) Stream-wise velocity(u_x) distribution function

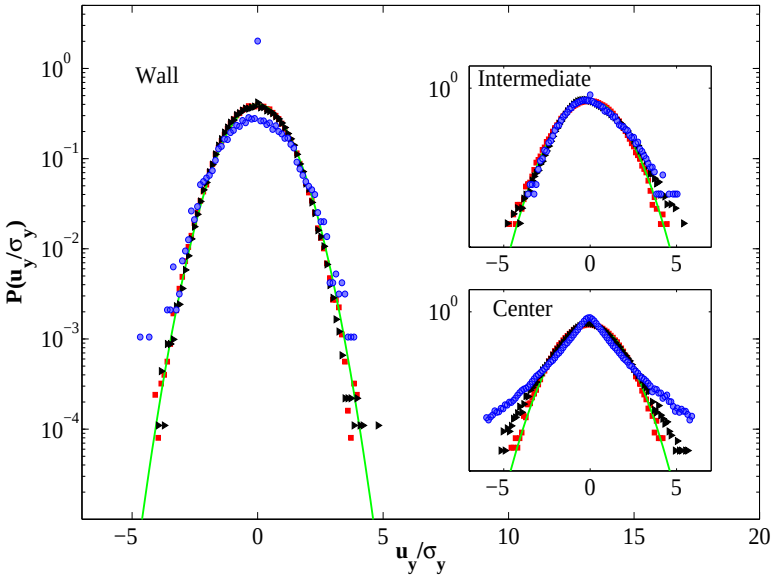

(b) Cross-stream velocity(u_y) distribution function

Figure 3.19: Probability distribution of (a) u_x and (b) u_y fluctuating velocities for e_n=0.85, β=-0.9, ν=0.01 in wall bin (main panel), intermediate bin (top inset) and center bin (bottom inset).

of Knudsen number have already been discussed in the previous section (Figs. 3.15a, 3.15b). It is seen that the exponent is ∼2.0 for all distributions except at the wall for Kn ∼ O(0.01) where the exponent is ∼1.3-1.4. Figures 3.20a and 3.20b show the distribution of velocity in x and y direction for β_w=-0.5 and e_n=0.99. It can be seen that the x-distribution is no longer symmetric and one can no longer describe it with a single exponent. Thus the tails of the distribution are studied separately by logarithmic graphs. The following is inferred : (i) a distinct peak appears at all orders of Knudsen number in the negative velocity tail which is discussed in detail by Alam & Chikkadi (2010). The peak persists throughout the system for Kn ∼ O(1) but diminishes as we move towards the center of the system for Kn ∼ O(0.1) and Kn ∼ O(0.01). (ii)The y-velocity remains close to Gaussian distribution with the exponent lying in the range 1.9-2.0 (iii)The exponent decreases as the Knudsen number is decreased in the wall bin for both distributions (iv) In the x-distribution the left velocity tail has higher exponent than the right velocity which is opposite to what is observed in case of smooth walled (β_w ∼ -1) inelastic systems.

On further increasing the dissipation at the wall to the maximum (β_w=0.0), a distribution of both the velocities is obtained as shown in Fig. 3.21a and Fig. 3.21b. It is seen that the peak in the distribution is enhanced compared to Fig. 3.20a and Fig. 3.20b. The deviation from Gaussian can be analyzed by studying the kurtosis and skewness in each bin as shown in Fig. 3.22. The kurtosis for Kn ∼ O(0.1) and Kn ∼ O(0.01) in the stream-wise velocity is ∼3.0 near the center bin but >3.0 close to the wall bins. The kurtosis for Kn ∼ O(1) is ∼4.9 which indicated peakedness throughout the system. The cross stream kurtosis is ∼3.0 throughout the system for all orders of Knudsen number. Skewness which speaks about the symmetry of the system tells that the stream-wise distribution (P(u_x)) is skewed near the walls for Kn ∼ O(0.1) and Kn ∼ O(0.01) but becomes symmetric as we move away from the wall towards the center. The cross-stream skewness is symmetric with respect to the channel centerline. The peak which appears in the stream-wise velocity in the wall bin is independent of the order of Knudsen number but depends on the dissipation at the wall. The effect of high dissipation on cross-stream distribution is seen distinctly in all bins for Kn ∼ O(1) whereas the effect reduces for lower Knudsen numbers as we move away from the wall. These high velocity tails are described in terms of two exponents- one for the left tail and the other for the right.
The P(u_y) exhibits bimodal behavior for higher Knudsen number (see main panel in Fig. 3.23). The bimodality is due to the dissipation at the walls [Alam & Chikkadi (2010)] and as the ratio of wall-particle to particle-particle collision becomes higher in case of high Knudsen numbers the bimodality gets pronounced as seen in Fig. 3.23. The top left inset which shows heights of the peak (H) as a function of Knudsen number exhibits a linear increase. The top right inset which shows that there is a increase in the distance between the peaks (P) with the increase in Knudsen number.

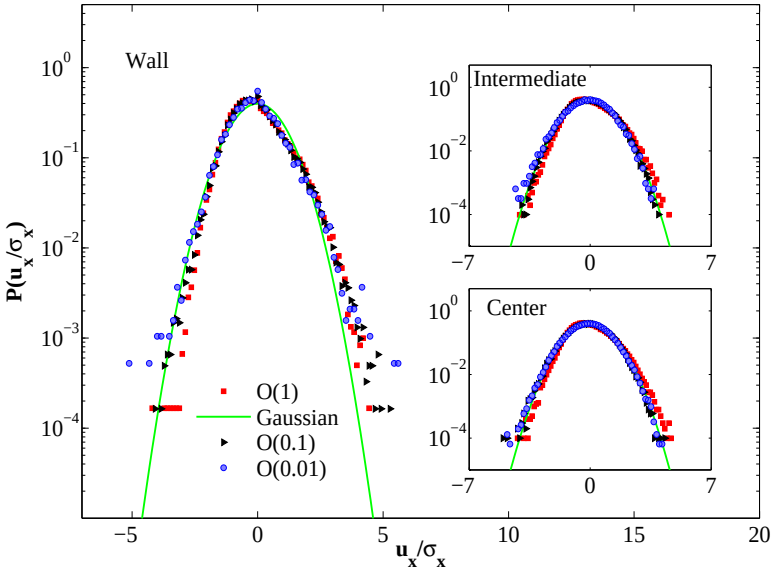

(a) Stream-wise velocity(u_x) distribution function

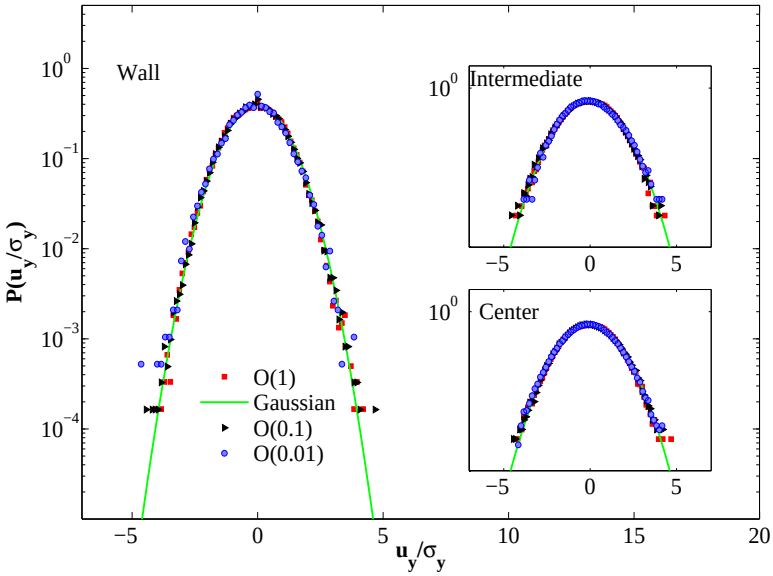

(b) Cross-stream velocity(u_y) distribution function

Figure 3.20: Probability distribution of (a) u_x and (b) u_y fluctuating velocities for e_n=0.99, β=-0.5, ν=0.01 in wall bin (main panel), intermediate bin (top inset) and center bin (bottom inset).

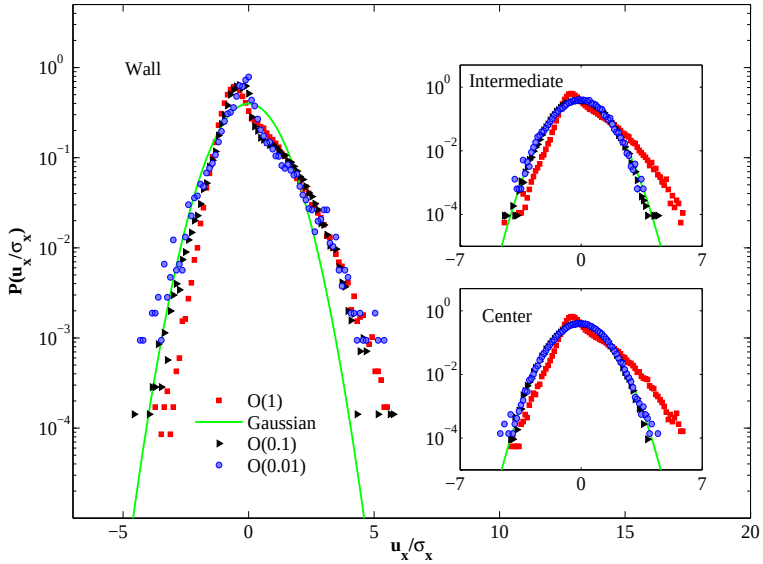

(a) Stream-wise velocity(u_x) distribution function

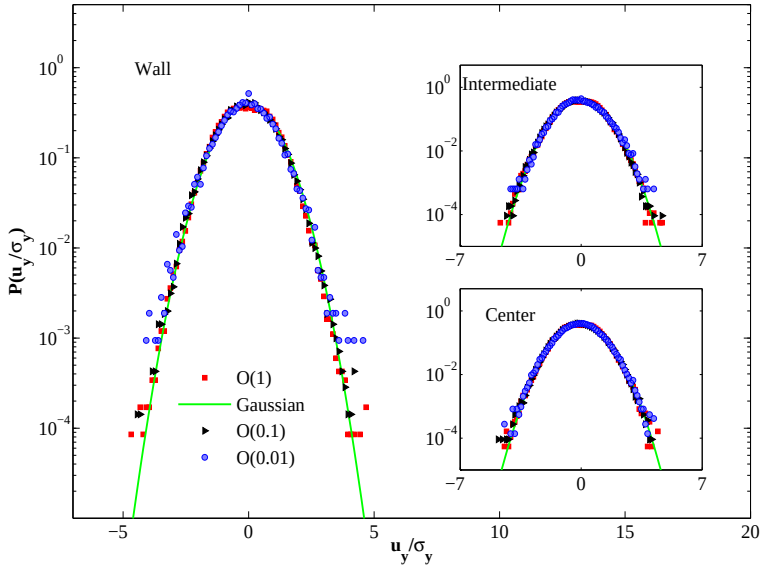

(b) Cross-stream velocity(u_y) distribution function

Figure 3.21: Probability distribution of (a) u_x and (b) u_y for e_n=0.99, β=0.0, ν=0.01 in wall bin (main panel), intermediate bin (top inset) and center bin (bottom inset).

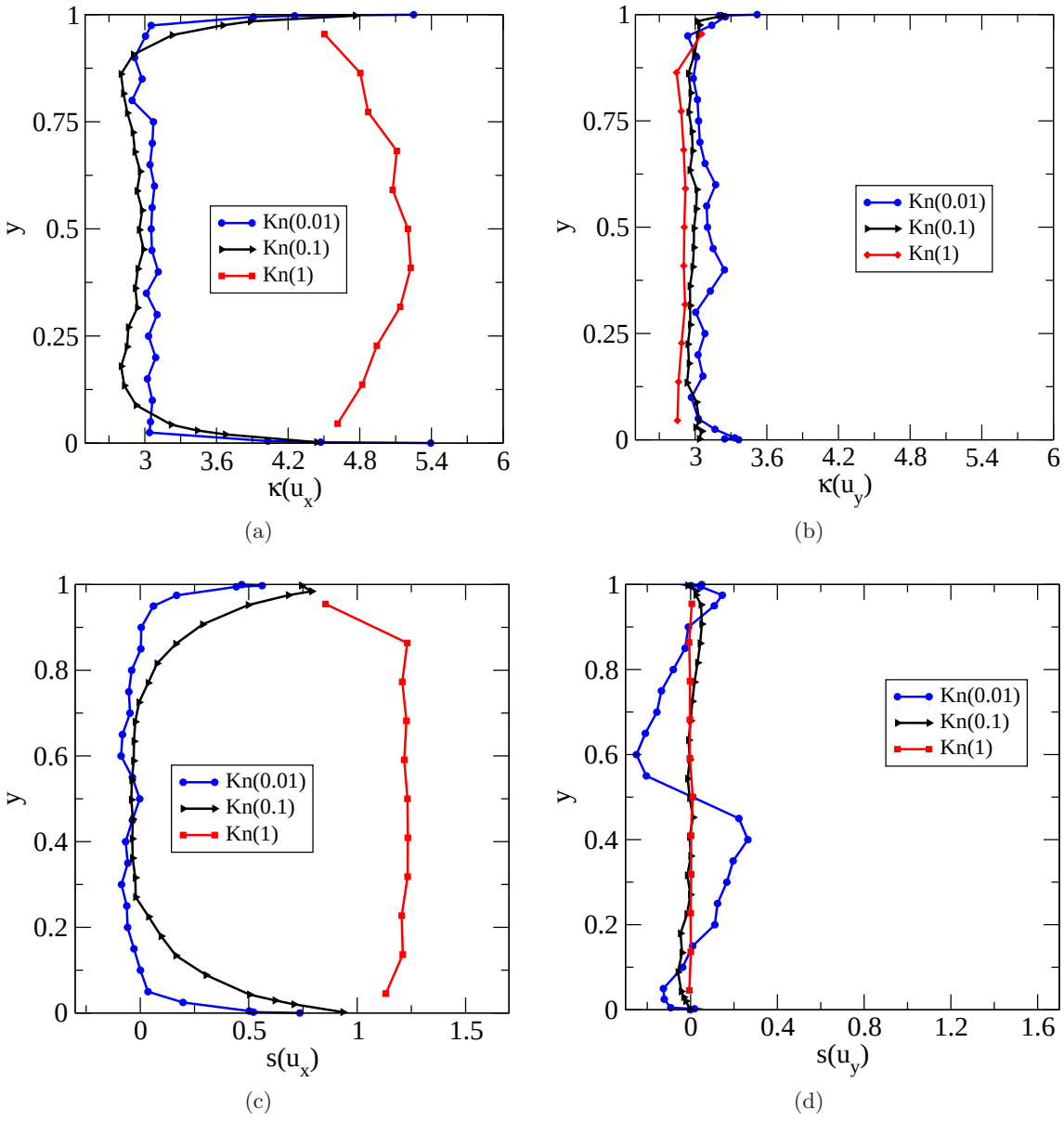

Figure 3.22: Kurtosis (a, b)and skewness (c, d) of u_x and u_y velocities, respectively for e_n=0.99, β=0.0, ν=0.01.

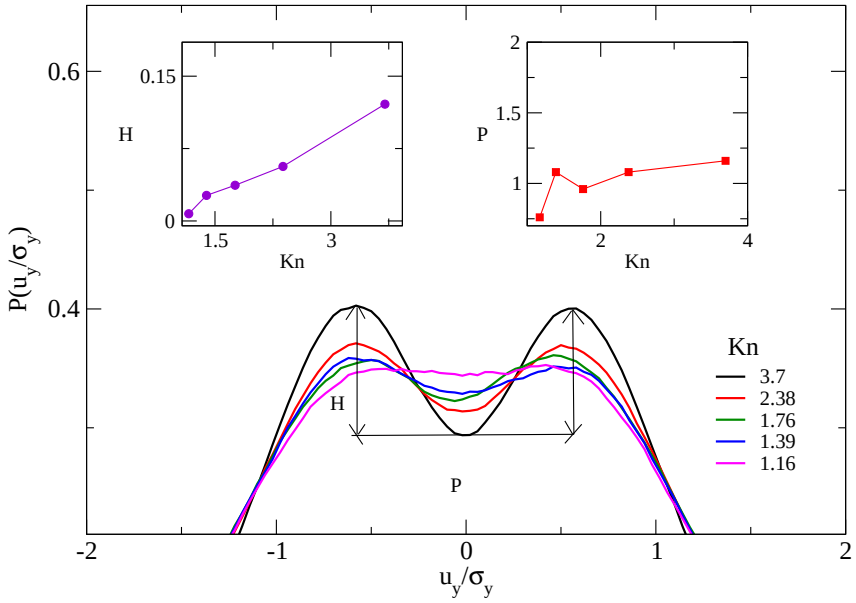

Figure 3.23: Distribution function for u_y velocity showing decrease in bimodal behavior with decrease in Knudsen number. Peak value (top left inset) and position of peak (top right inset) of P(u_x) in the wall bin (bin = 1). Parameter for the system are - L/d = 1000.0, e_n = 0.99, β_w = 0.0, ν = 0.01. The width of the system (W/d) is varied from 3.92 to 19.63 to span Knudsen number from 3.7 to 1.16.

Chapter 4

Slip velocity and wall temperature

Incompressible Navier-Stokes equation is given by:

$$\nabla.v = 0 \tag{4.1}$$

$$\rho\frac{Dv}{Dt} = -\nabla p + \nabla.[\mu[\nabla v + (\nabla v)^T]] \tag{4.2}$$

where v is velocity, p is pressure, μ is viscosity and t is time. No-slip boundary condition corresponds to the velocity of the liquid at the wall is same as the wall velocity. Though theoretically no-slip seems to be the best answer for what happens near the wall, but some non-Newtonian fluids like polymer melts [Denn (2001)] and rarefied gases [Knudsen (1909), Porodnov *et al.* (1974)] exhibit significant slip at the solid boundaries. Lauga *et al.* (2005)] describes the reviews the experimental, theoritical and computational research done on slip flows.
The Navier-Stokes equation holds good only in the continuum regime [Kn $<$ 0.01]. In the slip flow regime [0.01 $<$ Kn $<$0.1], the Maxwell's velocity slip and von Smoluchowski's temperature jump can be used as boundary conditions in the NS equation to solve for the flow [Karniadakis *et al.* (2005)].

$$U_w - U = \frac{(2-\sigma_v)}{\sigma_v} Kn \frac{\partial U_w}{\partial y} \tag{4.3}$$

$$T_w - T = \frac{(2-\sigma_T)}{\sigma_T} \frac{2\gamma}{\gamma+1} \frac{Kn}{Pr} \frac{\partial T}{\partial y} \tag{4.4}$$

where U_w, T_w are the velocity and temperature of the liquid close to wall; U and T are the velocity and temperature of the solid boundary; Pr is the Prandtl number; σ_v and σ_T are the tangential and thermal accommodation coefficients. Thermal accommodation coefficient gives the exchange of heat fluxes of incoming and outgoing molecules with respect to time. σ_T = 1 implies total heat exchange. Tangential accommodation coefficient gives the amount of tangential momentum exchange between the incoming and outgoing molecules. $\sigma_v = 0$ implies specular reflection, where the normal velocity component is reversed. $\sigma_v = 1$ signifies diffuse reflection where on collision with the wall all the tangential velocity is absorbed by the wall. For Kn $>$ 0.1, higher order corrections need to be applied to describe the stress tensor and heat flux vectors. The higher order corrections are given by Burnett and Woods equation which are derived from Boltzmann equation based on Chapman-Enskog expansion of the velocity distribution function (f).

$$f = f_0(1 + aKn + bKn^2) \tag{4.5}$$

where f_0 is Maxwell distribution function; a and b are functions of density, temperature and velocity. Zeroth order solutions give the Euler equation, first order gives the Navier-Stokes equation and the second order gives the Burnett equations. Karniadakis *et al.* (2005) gave a

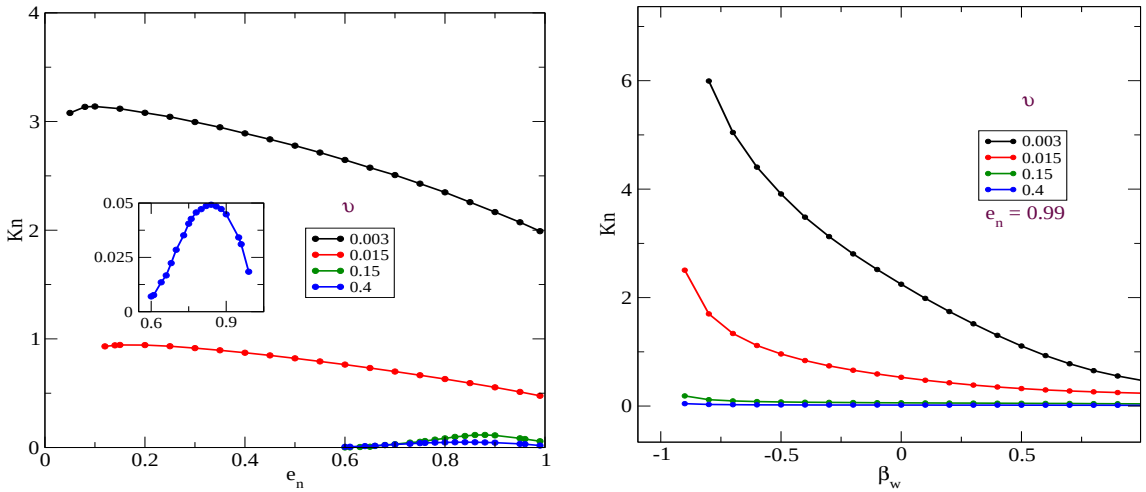

(a) (b)

Figure 4.1: Variation of Knudsen number with e_n (a) and β_w (b) at different volume fractions.

generalized velocity boundary condition which incorporates the second order correction as

$$U_w - U = \frac{(2-\sigma_v)}{\sigma_v}\frac{Kn}{(1-bKn)}(\frac{\partial U}{\partial n})_w \tag{4.6}$$

Chikkadi & Alam (2009) have studied the variation slip velocity and gradient of slip with Knudsen number for granular Poiseuille flow through event driven simulations. They assumed a relationship as $U_w \propto Kn^{\gamma}\ \frac{dU_w}{dy}$ and determined the value of γ for different values of e_n near elastic limit. Here the Knudsen number was varied by changing the volume fraction of the system. In the present study, the volume fraction (ν) in the system is kept constant and the Knudsen number is varied by varying the width (W/d) of the channel. In Sec. 4.1, the slip velocity and its gradient are discussed; and in Sec. 4.2 the wall temperature and its gradient are looked into.

4.1 Slip velocity and gradient of slip velocity

The domain under consideration is divided into bins as per Eq. 2.22. The velocity in the wall bin is considered to be the slip velocity. The effects of Knudsen number, e_n and β_w on slip velocity are studied. Later, an effort is made to explain the slip velocity in terms of Knudsen number and gradient of slip velocity. All simulations are done for Kn $>$ 0.01, ν = 0.01 and e_w=1.0.

Fig. 4.1a shows the variation of Knudsen number with the normal restitution coefficient (e_n) at β_w = -0.1 and W/d = 31.0 at four different values of ν - 0.003, 0.015 ,0.1 and 0.4. For volume fraction of 0.015 and 0.003 one can simulate the flows up to $e_n \sim 0.1$. As the system is made more denser, there is an increase in particle-particle interaction leading to clustering and thus inelastic collapse occurs. Though the TC-rule described in Chapter 2 is applied, beyond a certain dissipation it becomes invalid. The inset in Fig. 4.1a shows the variation of Knudsen number with restitution coefficient for ν = 0.4. It is seen that with the decrease in restitution coefficient the Knudsen number increases, reaches a maximum and finally decreases. The posi-

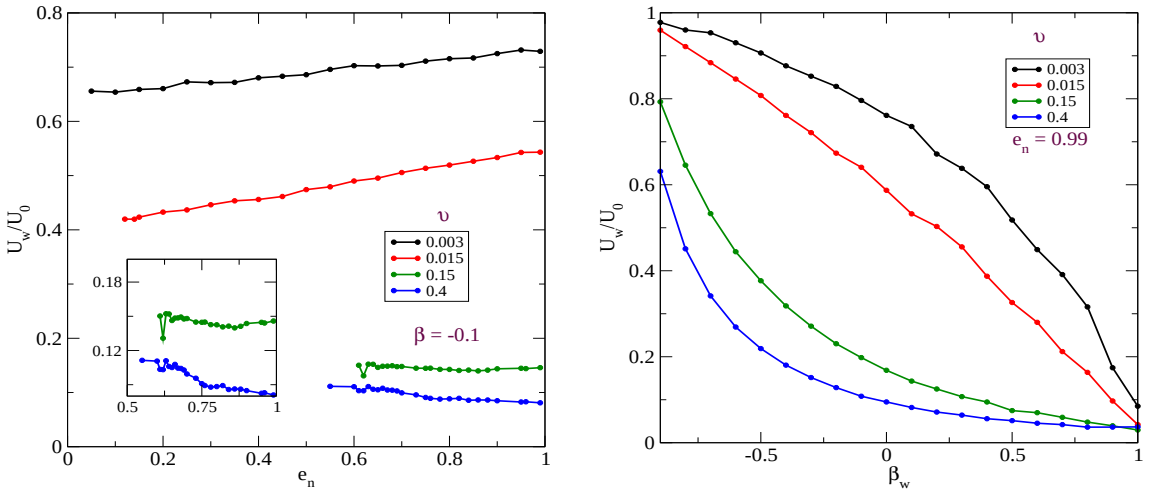

Figure 4.2: Variation of slip velocity (U_w) with e_n (a) and β_w (b) at different volume fractions.

tion of this maximum depends on ν. This is due to the transition of the flow from plug to slug as the restitution coefficient is reduced as described in detail in section 3.2.2. As the mean free path is inversely related to the system density, the decrease in the volume fraction leads to an increased Knudsen number.

Fig. 4.1b shows the variation of Knudsen number with wall restitution coefficient (β_w) at e_n = 0.99, W/d = 31.0. Rough walls ($\beta_w \sim 1$) have low Knudsen number and smooth walls ($\beta_w \sim$ -1) have high Knudsen numbers for all volume fractions. Since the mean free path (λ) is inversely proportional to the density of the system, for a given value of β_w the Knudsen numbers of dilute flows are larger than those of moderately dense (ν = 0.15) and highly dense granular flows (ν = 0.4). It is interesting to see the evolution of the graph as the β_w is decreased from 1 to -1. For low ν (0.015, 0.003), a small decrease in roughness of the wall leads to a large increase in Knudsen number.

Fig. 4.2a shows the variation of slip velocity (U_w) with restitution coefficient at different volume fractions for β_w = -0.1, W/d = 31.0. The slip velocity decreases with the increase in dissipation (1-e_n^2) for dilute flows as seen in ν = 0.015 and 0.003. The inset shows the variation of U_w with e_n for moderately dense flow (ν = 0.15) and highly dense flows (ν = 0.4). It shows a slight but insignificant rise in the slip velocity with decrease in e_n.

Fig. 4.2b shows the effect of wall roughness on the slip velocity (U_w) at e_n = 0.99, W/d = 31.0. The flow slips the least for rough walls ($\beta_w \sim 1$) and most for smooth walls ($\beta_w \sim 1$). The curves of U_w versus β_w are concave for very dense systems as seen for ν = 0.4. As the density is decreased, the trend of the curve gradually changes from concave to convex as seen for ν = 0.003. At a given β_w, the slip is maximum in dilute flows.

Fig. 4.3a shows the variation of gradient of slip as a function of normal restitution coefficient (e_n) for β_w = -0.1, W/d = 31.0 at four different volume fractions. The gradient of slip initially decreases with the decrease in e_n, reaches a minima and further increases as seen for ν = 0.4. Though not significant, a slight increase in the gradient of slip near the wall is observed in dilute flows (ν = 0.015 and 0.003). Gradient of slip velocity as a function of β_w is shown in Fig. 4.3b for quasi-elastic system (e_n = 0.99), W/d = 31.0. The gradient of slip is minimum for smooth

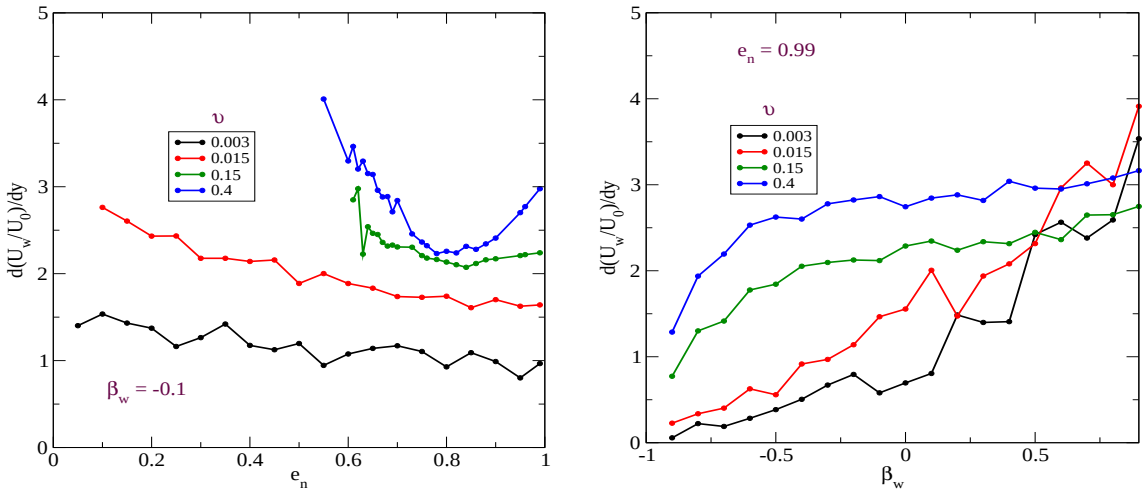

(a) (b)

Figure 4.3: Variation of gradient slip velocity (dU_w/dy) with e_n (a) and β_w (b) at different volume fractions.

walls and increases with the increase in the roughness of the walls.

Till this section variation of slip and its gradient is studied with respect to the input parameters - e_n, β_w and ν. The width of the system was kept constant and the length (L/d) was varied to change the volume fraction. In the next section, we study the variation of slip and its gradient with respect to the Knudsen number. For a given volume fraction, the L/d is fixed and the Knudsen number is changed by varying the width (W/d) of the channel. Most of the simulations in this section are done for $\nu = 0.01$. For low Knudsen number trials the curve raw data fluctuates as shown in Fig. 4.4a. The data is smoothened by the following equations -

$$U_i = \frac{\sum_{j=i}^{i+n} U_j}{n} \qquad y_i = \frac{\sum_{j=i}^{i+n} y_j}{n} \tag{4.7}$$

where n = 1.5% of the total number of bins initially present, i.e if a trail has 1000 bins then running average is taken over 15 points. The smoothened curve is shown in red line.
Slip velocity as a function of Knudsen number is shown in main panel of Fig. 4.4b for e_n = 0.99, 0.9, 0.8 and 0.7 with ν set to 0.01. At low Knudsen number the slip velocity drastically increases. The slope of the curve decreases for higher Knudsen number and finally reaches a constant slope at high Knudsen number (Kn > 1). For a given width of the channel, Knudsen number is higher for lower values of e_n. The slip velocity is higher for quasi-elastic ($e_n \sim 1$) trials than for inelastic systems ($e_n < 1$). The gradient of slip is plotted as a function of Knudsen number for different values of e_n in Fig. 4.7b.

In order to derive the relationship between of slip velocity, gradient of slip velocity and Knudsen number, we restrict the normal restitution coefficient to 0.9< e_n <1 and try to derive a relation between them. Inset in Fig. 4.5 is a plot of $\log_{10}(U_w)$ versus $\log_{10}(Kn)$. In the region between Kn $\sim$ [0.01, 0.32] a power-law ($U_w \propto Kn^{\alpha}$) behavior is observed. The exponent α = 0.87, 0.83 and 0.73 for e_n = 0.99, 0.95 and 0.9, respectively. The residuals for these power law

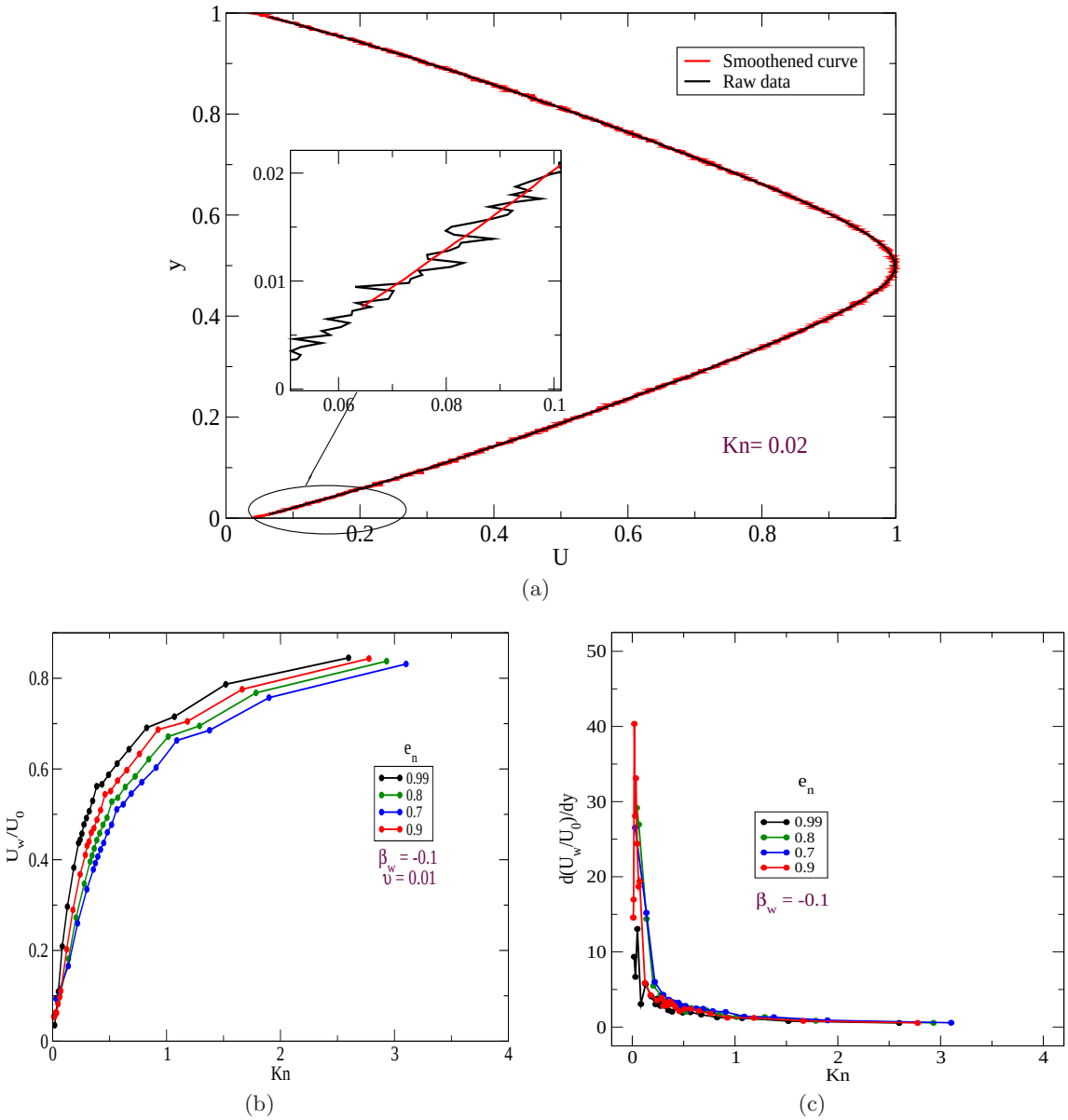

Figure 4.4: (a) Stream-wise velocity (U) showing the raw data and smoothened data for Kn=0.02, $\nu = 0.01$. Variation of slip velocity (b) and gradient of velocity (b) with Knudsen number at different values β_w for $\nu = 0.01$.

fits are < 0.005. Beyond Kn ~ 0.32 all the points at different values of e_n merge and the value of the α decreases. Below Kn ~ 0.01, the slip velocity shows different values of exponent for different restitution coefficients.

From the main panel of Fig. 4.6, it is difficult to predict the behavior of gradient of slip with Knudsen number. Hence, a logarithm plot is shown in the inset of this figure. If one assumes that the curve behaves as per power-law ($dU_w/dy \propto Kn^{\bar{\alpha}}$), then depending on the value of $\bar{\alpha}$ three regimes can be outlined - Kn > 0.1 where $\bar{\alpha} < 0$, Kn < 0.07 where $\bar{\alpha} > 0$ and the intermediate regime [$0.07 <$ Kn < 0.1] where $\bar{\alpha} \sim 0$.

Fig: 4.7a shows the behavior of slip velocity as a function of Knudsen number at different wall restitution coefficient (β_w) in dilute flows. Slip velocity increase with the decrease in wall roughness. It varies largely with Knudsen number for smooth walls ($\beta_w \sim$ -1) rather than rough

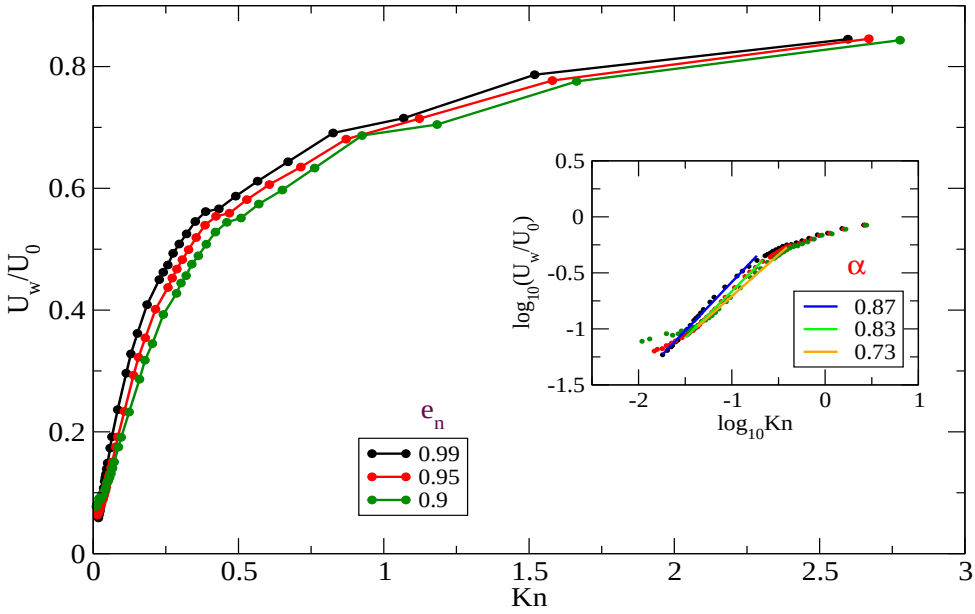

Figure 4.5: Variation of slip velocity with Knudsen number at different values e_n for $\nu = 0.01$.

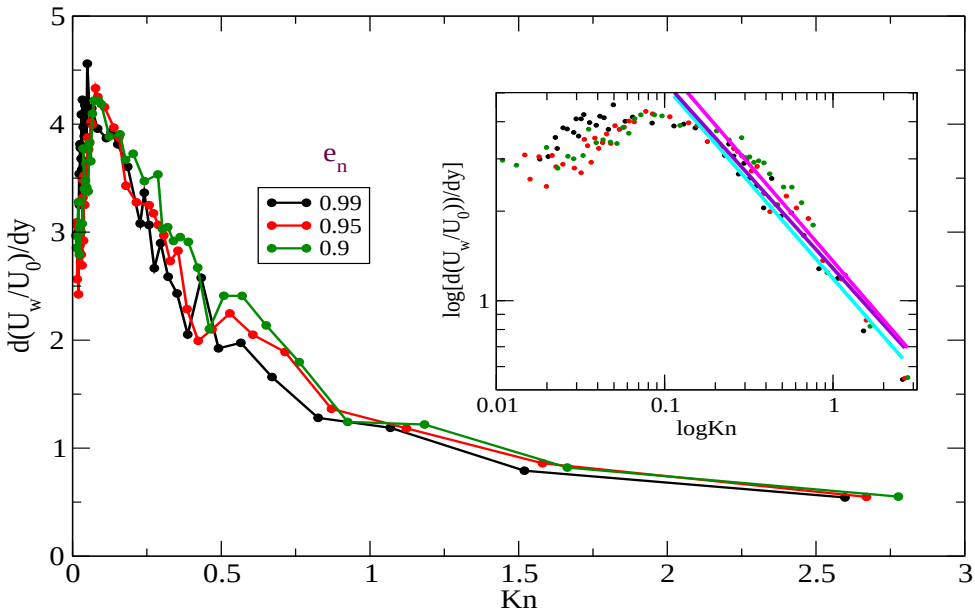

Figure 4.6: Variation of slip velocity with Knudsen number at different values e_n for $\nu = 0.01$.

walls ($\beta_w \sim 1$) as previously predicted by Chikkadi & Alam (2009). For smooth walls, the slip velocity reaches a constant value at high Knudsen numbers.

To understand the effect of wall roughness on gradient of slip velocity with Knudsen number, a logarithmic plot of slip velocity (U_w) versus Kn is shown in Fig. 4.7b. Roughness does not significantly affect the gradient of slip. It indicates that at low Knudsen number the gradient of slip increases, reaches a maximum (Kn $\sim$ 0.1) and later decreases for higher Knudsen number.

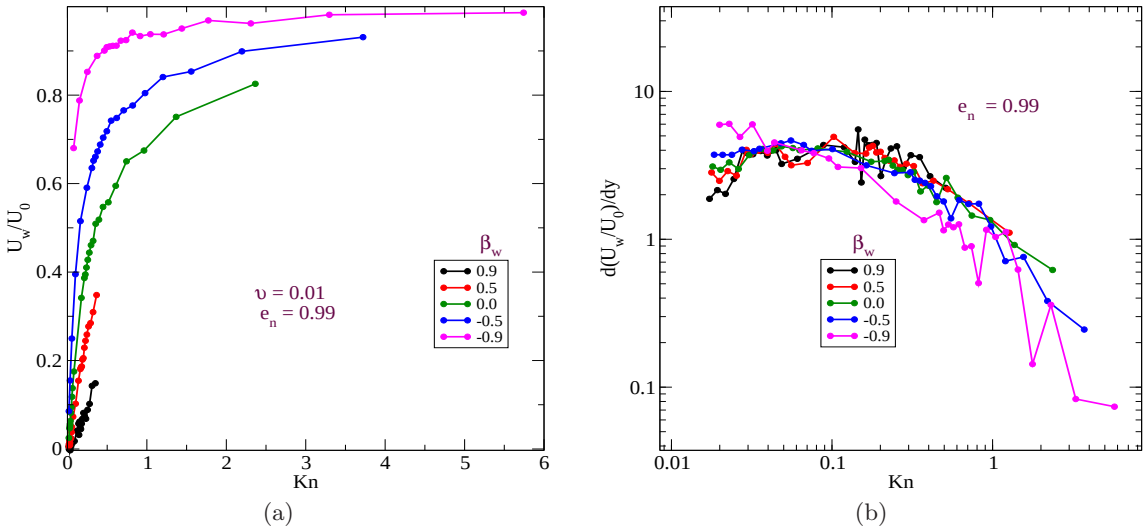

(a) (b)

Figure 4.7: Variation of slip velocity (a) and gradient of velocity (b) with Knudsen number at different values β_w for $\nu = 0.01$.

4.2 Wall temperature and gradient of wall temperature

Wall temperature decreases with decrease in e_n close to elastic limit ($e_n \sim 1$), reaches a minima and later increases as shown in Fig: 4.8a. This decrease is not significant in dilute systems ($\nu =$ 0.003 and 0.015). The magnitude of increase of T_w is proportional to the volume fraction of the system. The blue line which represents $\nu = 0.4$ shows a large increase as compared to others. No relationship was found between the magnitude of wall temperature and the volume fraction from these results.

The variation of wall temperature with β_w at different volume fractions (ν) is shown in Fig.

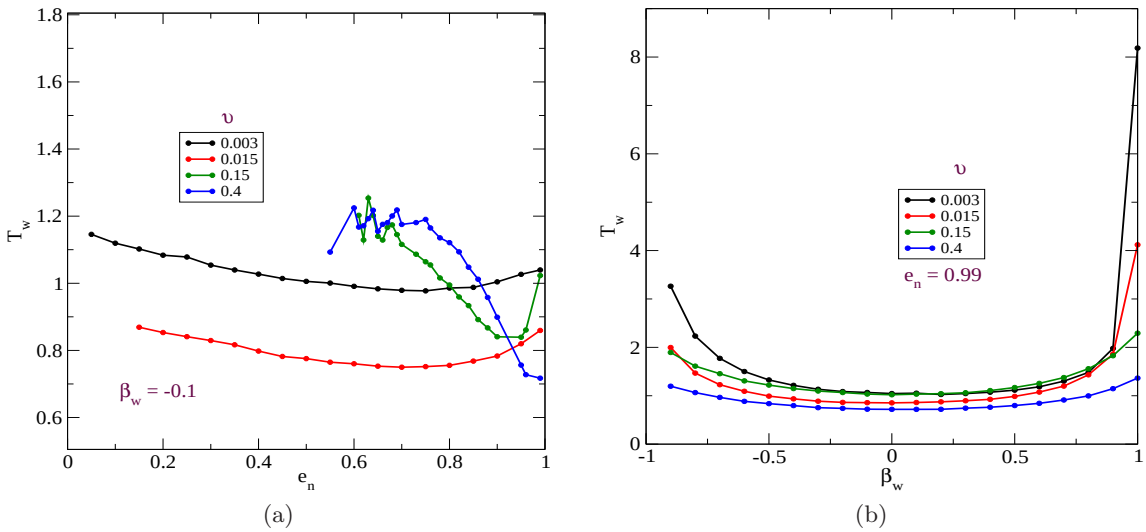

(a) (b)

Figure 4.8: Variation of wall temperature (T_w) with e_n (a) and β_w (b) at different volume fractions.

4.8b. The wall temperature is minimum at $\beta_w \sim 0$ which corresponds to maximum dissipation. T_w gradually increases with increase in $\mid \beta_w \mid$.

Next we study gradient of granular temperature (dT_w/dy) as a function of e_n at different volume

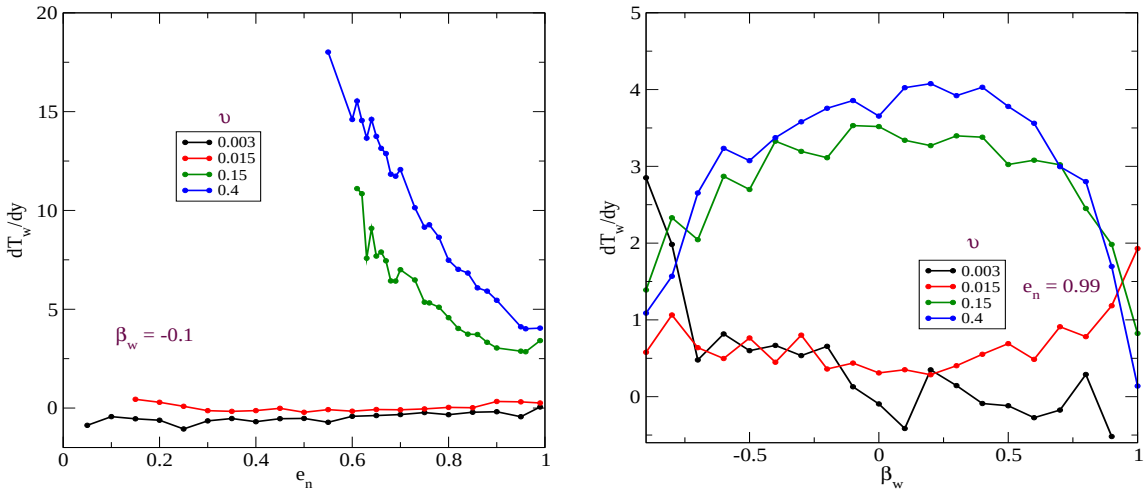

(a) (b)

Figure 4.9: Variation of gradient wall temperature (dT_w/dy) with e_n (a) and β_w (b) at different volume fractions.

fractions for β_w = -0.1 in Fig. 4.9a. There is almost no change in dT_w/dy with e_n in dilute flows ($\nu = 0.003$ and 0.015) whereas one can see a significant appreciation in denser systems as e_n is decreased. By observing the plot 4.9a, one might think that the magnitude of the gradient of temperature increases with volume fraction. But Fig. 4.9b shows that the value of gradient depends on β_w. At high dissipations ($\beta_w \sim 0$) there is no significant increase in the gradient in dilute flows but it reaches a maximum for dense flows.

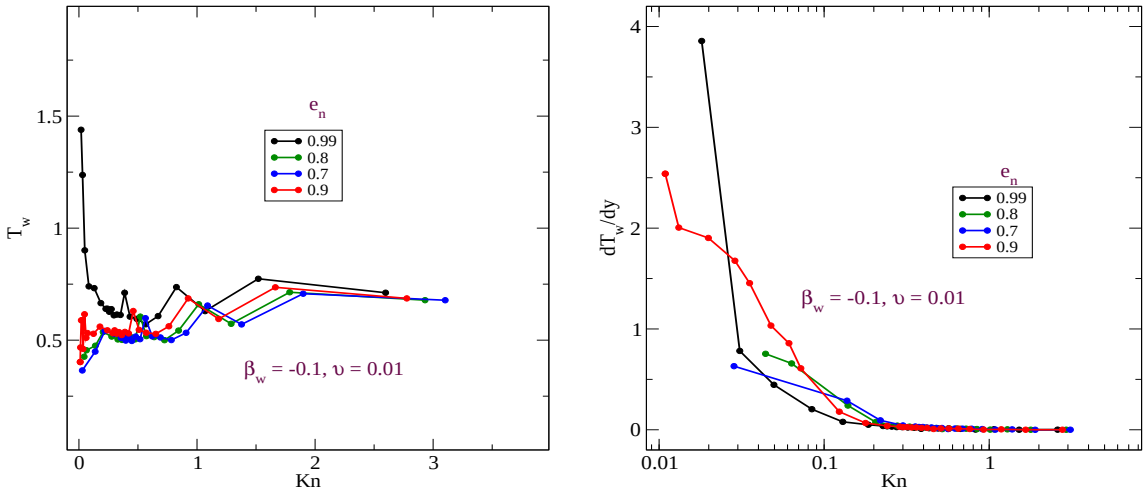

(a) (b)

Figure 4.10: Variation of wall temperature (a) and gradient of wall temperature (b) with Knudsen number at different values e_n for $\nu = 0.01$.

Fig. 4.10a shows the change in T_w with Knudsen number at different densities. For low Knudsen number (Kn $\sim 10^{-2}$) the behavior is unpredictable. With the increase in Knudsen number the wall temperatures for all values of e_n become equal to ~ 0.6. The gradient of wall temperature is maximum for lower Knudsen number and reduces to 0 as Kn ~ 1 (Fig. 4.10b. For a given width of the channel this gradient has a higher value for a less dissipative system. Fig. 4.11a and Fig. 4.11b show the variation of wall temperature and its gradient with Knudsen

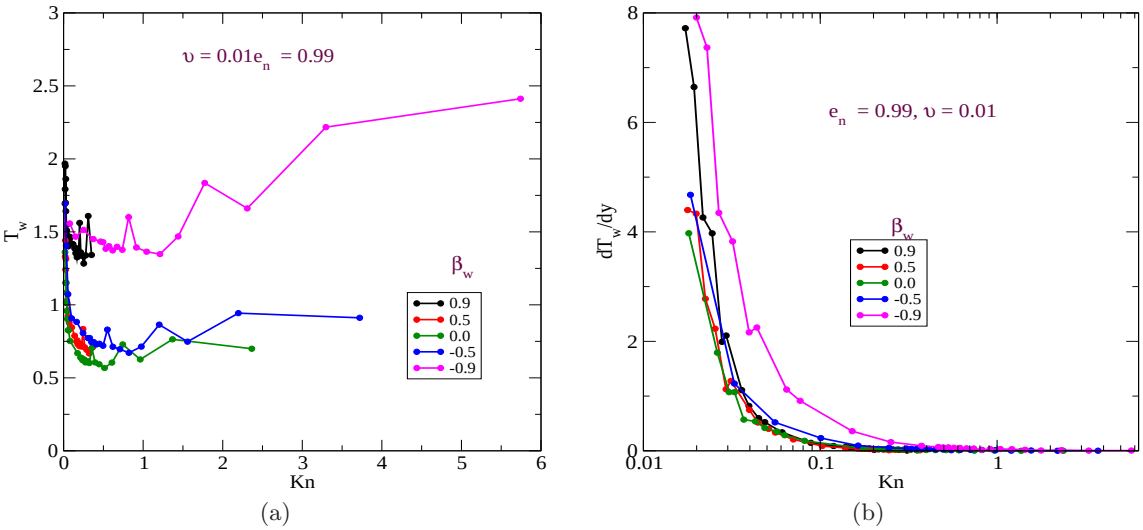

(a) (b)

Figure 4.11: Variation of wall temperature (a) and gradient of wall temperature (b) with Knudsen number at different values β_w for $\nu = 0.01$.

number at different values of β_w. We do not observe any particular trend Fig. 4.11a. The gradient of wall temperature decreases to 0 with increase in Kn $\sim$ O(1) (Fig. 4.11b).

Chapter 5

Granular flow in 3-dimensions

Density waves are one of the most intriguing phenomenon observed in granular flows. Ample experiments have been conducted on about granular flow in a vertical pipe. Horikawa *et al.* (1995) studied the density waves in a vertical pipe attached below a conical hopper. The patterns were analyzed by measuring the intensity of light transmitted across the pipe. An FFT analysis of the intensity of the light recorded showed that the power spectrum decays as $1/\ f^{\alpha}$ where $\alpha \approx 1.5$. Later Peng & Herrmann (1994), Ichiki (1995) and Moriyama *et al.* (1998) conducted similar experiments and found this value to be 4/3. All the experiments find formation of density waves at a certain distance below the hopper outlet. Raafat *et al.* (1996) found that increase in the size of the grain leads to formation of waves farther away from the inlet. Experiments also show multiple clumps in the vertical pipe. The effect of surrounding medium is studied theoretically by Ichiki (1995) and experimentally by Horikawa *et al.* (1995), Moriyama *et al.* (1998) and Ellingsen *et al.* (2010).

Some of the extensive simulations on density waves for 2D Poiseuille flow have been reported by Liss *et al.* (2002); Alam *et al.* (2009). Density waves in 2D and 3D Couette flow is studied by Conway & Glasser (2004). Effect of system dimensions on the wave pattern is investigated in detail in their work. They also report formation of double waves in Couette flows in very dense regimes and also explain the absence of hexagonal close packing for polydisperse systems. It is reported that addition of gravity in the Couette flow leads to shift of density waves towards the wall which moves along the direction of gravity. Simulations by Liss *et al.* (2002) and Conway & Glasser (2004) broadly classify the structures in density waves into 3 groups - plug, wave and slug/clump. Later, Alam *et al.* (2009) reports an additional structure called the varicose mode. The effects of system dimensions, volume fraction (ν), particle-particle restitution (e_n) and walls are studied. It is seen that particle-particle restitution coefficient (e_n) plays a more important role than the wall boundary conditions in the formation of density waves. Theoretical work on granular Poiseuille flows have been done by Riethmüller *et al.* (1997), Wang *et al.* (1997), Alam *et al.* (2009) and Khain (2011).

In the present chapter the density waves in 3D Poiseuille flow are studied for moderately dense ($\nu = 0.15$) system. One of the major problems encountered in simulations of inelastic system is inelastic collapse. It is a condition where there are infinite number of collisions in a short period of time. This problem is overcome by adopting the TC model suggested by Luding & McNamara (1998) as described in Sec. 2.3. In Sec. 5.1, mean field results are shown. Velocity distribution function is studied in Sec. 5.2 for varying e_n. In Sec. 5.3 we deal with the method used to systematically analyze density waves. In 5.4, transient and steady state behavior of density waves formed in flow between two plates and flow in a square duct are examined. In all cases, a square duct (W=D) is considered to remove the complexity associated with asymmetry of the system. The last section (Sec. 5.5) deals briefly with the effect of asymmetry (W≠D) on

the flow profiles in a closed duct.

5.1 Mean Fields

The flow between two parallel plates and in a square duct are discussed below. All the simulations are done for N=125000 and ν=0.15. The ratio of system dimensions is L:W:D=2:1:1 where W/d =60. Trials are done for three different values of e_n = 0.99, 0.9 and 0.8. In this section, we discuss the mean fields (granular temperature (T), volume fraction (ν), stream-wise velocity profile (U)). Averaging is done as discussed in Sec. 2.5. The system is divided into bins in the y-direction as given in Eq. 2.22.

5.1.1 Flow between 2 parallel plates

The walls are present in the y-direction and the other two directions, x and z, are periodic. All mean field profiles are translated along the y-axis for clear visualization of the surface plots. The wall boundary conditions are - $\beta_x = 1.0$, $\beta_z = 1.0$ and $e_w = 1.0$ which corresponds to perfectly rough walls. The number of bins along the y-direction is fixed to 50. The normalized velocity in Fig. 5.1a shows that the profile becomes flatter at the center of the system as the e_n is decreased. The particles in the system lose their energy leading to accumulation in the center of the system. Thus, an inelastic system has dilute regions surrounding a central dense core. The same can be interpreted from the volume fraction (ν) profile as shown in Fig. 5.1b. In extremely inelastic system these particles arrange themselves into a compact crystalline (hexagonal in 2D) structures. The reduction in the local mean free path of the particles due to accumulation leads to reduction in the granular temperature (Fig. 5.1c) at the center, in dissipative systems. Hence, the granular temperature surface plot is flatter for e_n=0.99 compared to e_n=0.80. In inelastic systems ($e_n < 1$), farther from the dense center, the particles are relatively free to move and hence have higher mean free path. This explains the rugged profile in the granular temperature plot (Fig. 5.1c) close to the wall.

5.1.2 Flow in a square duct (4walls)

The walls are present in both y and z-directions, and the system is periodic in the x-direction. The system is divided into 50×50 bins along y and z-direction. The density profile (Fig. 5.2b) shows that with the increase in inelasticity, particles cluster more near the corners and the center. At high dissipation (e_n=0.8), the corners are as dense as the center of the system. The normalized velocity profile in Fig. 5.2a shows that the velocity is minimum near the walls and the corners. The velocity profile is flattened in systems with higher dissipation due to accumulation of particles. As explained previously, regions of low density have high granular temperature and vice-versa and thus, the granular temperature is minimum at the walls and center as shown in Fig. 5.1c.

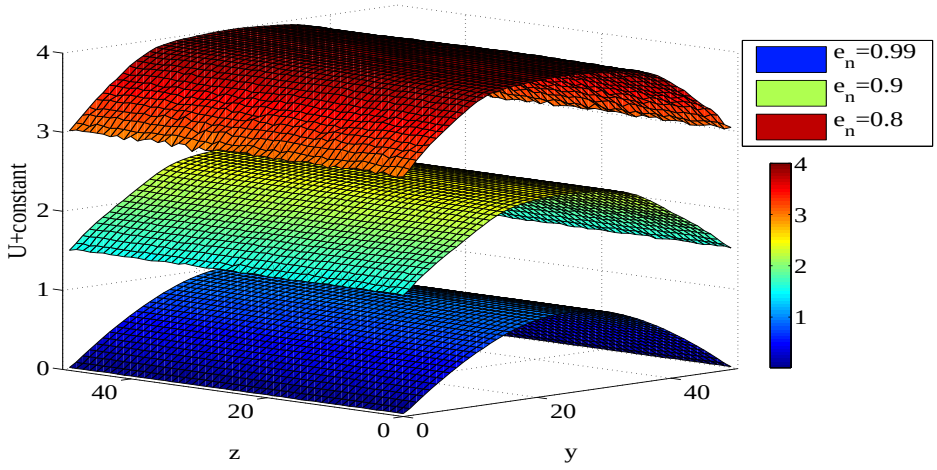

(a)

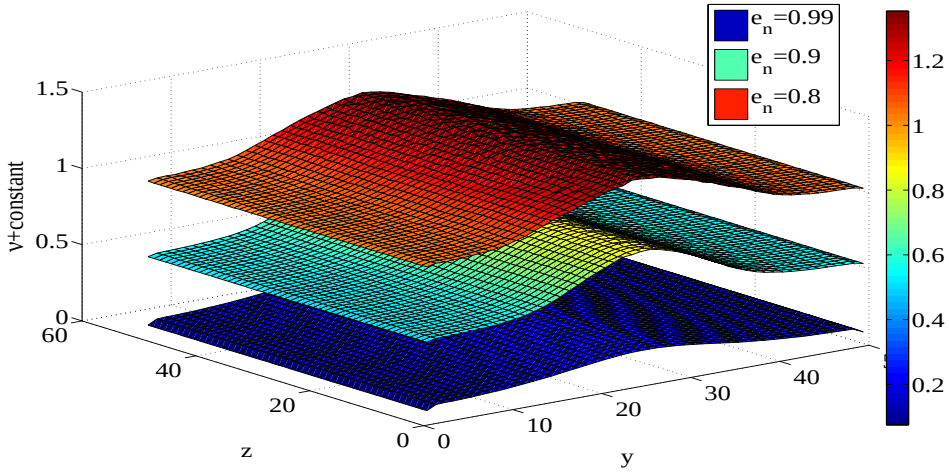

(b)

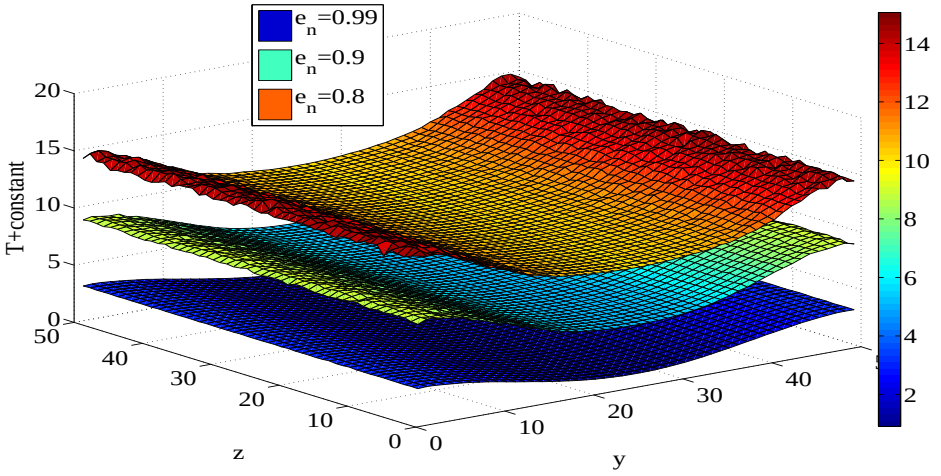

(c)

Figure 5.1: Stream-wise mean velocity (a), volume fraction (b) and granular temperature (c) in different bins at different e_n for flow between two parallel plates. N = 125000, $\beta_x = \beta_z = 1.0$, W/d = 60.0, L:W:D = 2:1:1 and $\nu = 0.15$.

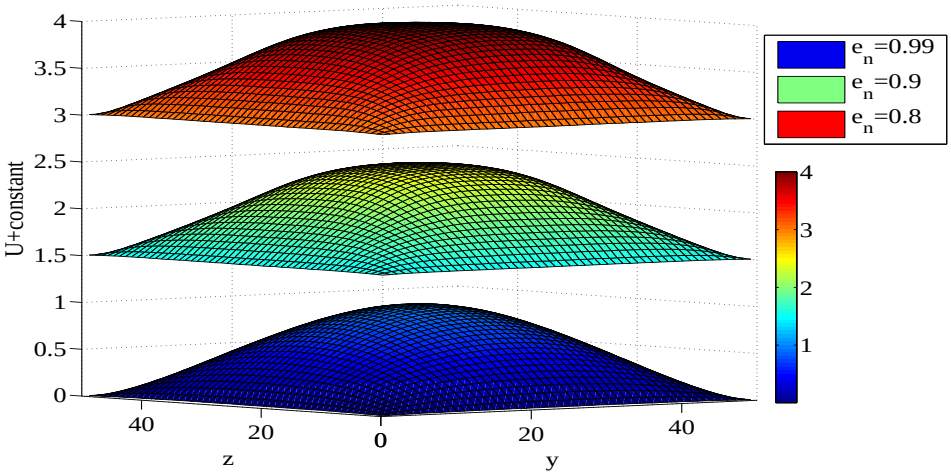

(a)

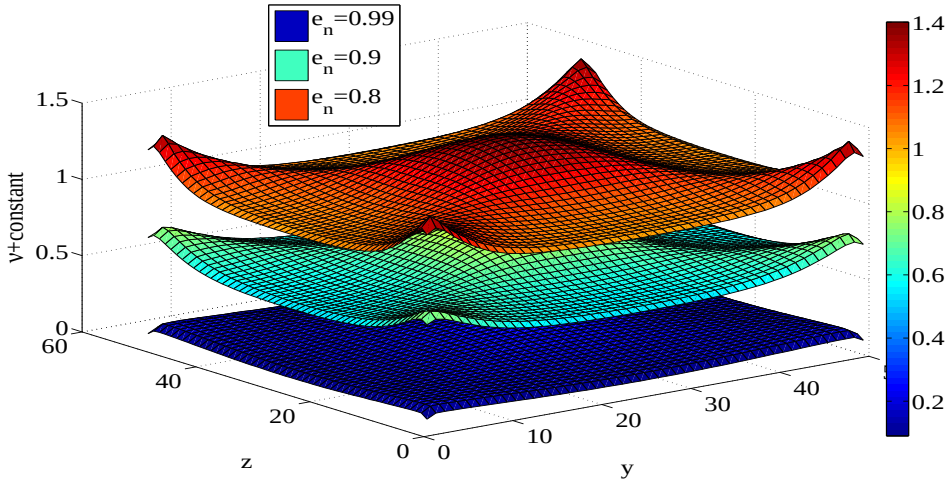

(b)

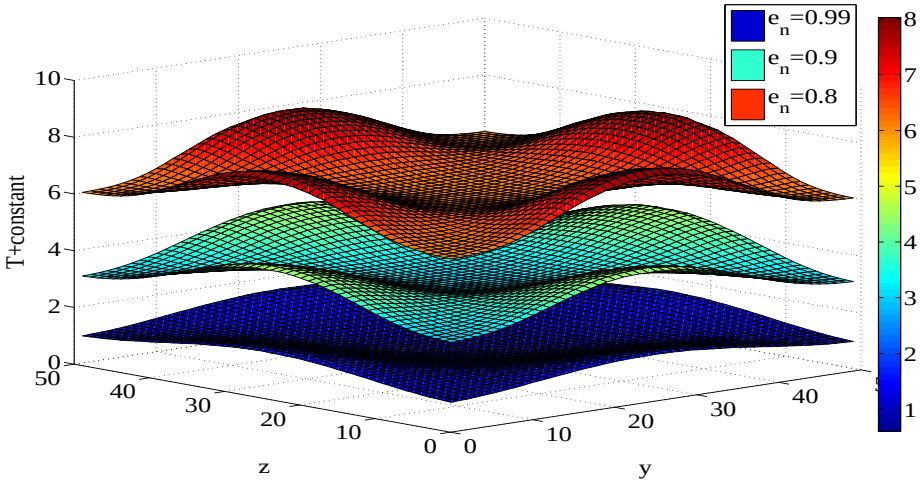

(c)

Figure 5.2: Flow in square duct: Stream-wise mean velocity (a), volume fraction (b) and granular temperature (c) in different bins at different e_n. N = 125000, $\beta_w = 1.0$, W/d = 60.0, L:W:D = 2:1:1 and $\nu = 0.15$.

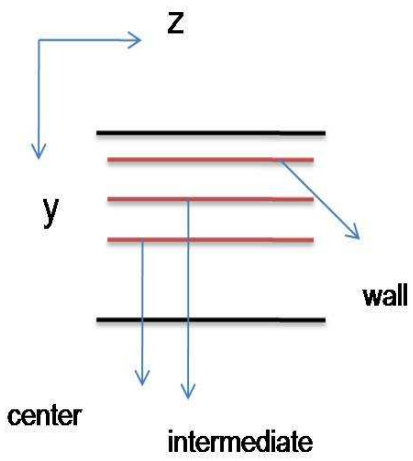

Figure 5.3: Flow between 2 plates: Schematic of the positions of the bins where the VDF is calculated.

5.2 Velocity distribution function (VDF)

5.2.1 VDF: Flow between two parallel plates

The VDF is calculated for 3 different values of normal restitution coefficient - 0.99, 0.9 and 0.8. The system is divided into different bins along the direction of the wall. The positions of the bins is shown in Fig. 5.3. The probability distribution of the bin near the wall (bin=1), the center (bin=25) and the intermediate (bin=12) for x, y and z fluctuating velocity are shown in Figs. 5.4a, 5.4b and 5.4c, respectively. In all these figures, the main panel shows the velocity distribution for the wall bin. The top and bottom insets show the distribution in the intermediate and center bins, respectively. The green line in all figures is a Gaussian curve which helps in comparing the deviation of the distribution. The following general observations can be made from the distribution functions: (i) the distribution in all the bins for x, y, and z fluctuating velocities obey Gaussian distribution in the quasi-elastic limit (e_n=0.99), (ii) the velocity distribution obeys almost Gaussian distribution in the wall bin for all values of e_n, (iii) decrease in e_n leads to a broader distributions in bins farther from the walls. The tails of the distribution tend behave like stretched exponential. The tails also become denser as we move from the wall towards the center of the system as most clumping happened in the center bin, (iv) the distributions of y and z-velocity are similar in almost all the bins. On comparing the y and z fluctuating velocity distributions in the intermediate bin we see that P(u_y) has a higher range [-10, 10] (see top inset of Fig. 5.4b) compared to P(u_z) (see top inset of Fig. 5.4c) , (v) P(u_x) distribution in the intermediate and center bin is asymmetric unlike the y and z-distribution. Its negative tail deviates dramatically from a Gaussian.

5.2.2 VDF: Flow in a square duct

The ratio of L:W:D is 2:1:1 with W/d=60. The fluctuating velocities of the particles at different bins are found out and the velocity distributions are separately calculated in every bin. In order to calculate the probability distribution, the system is divided into 50 $\times$ 50 bins in x and

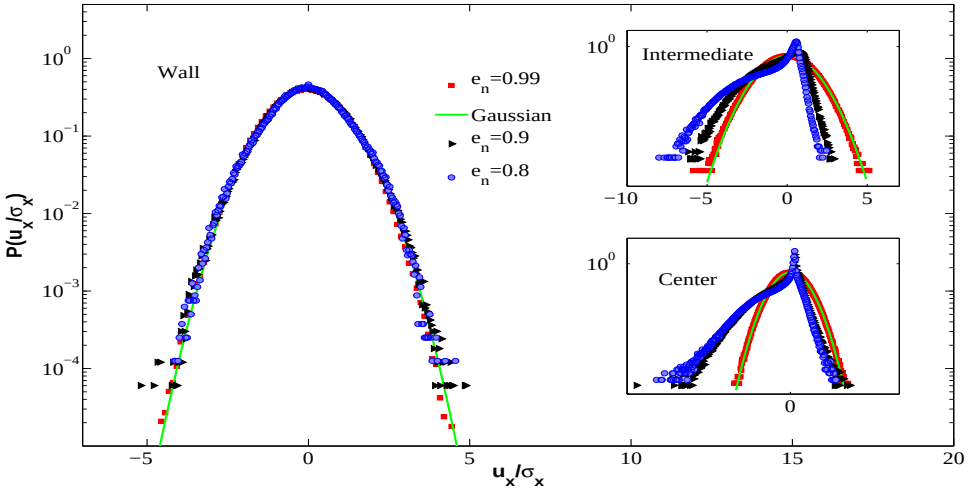

(a)

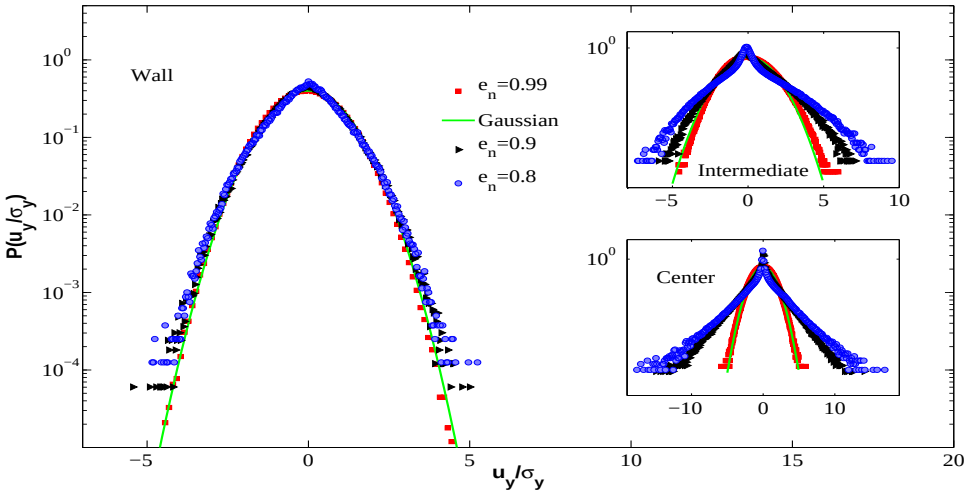

(b)

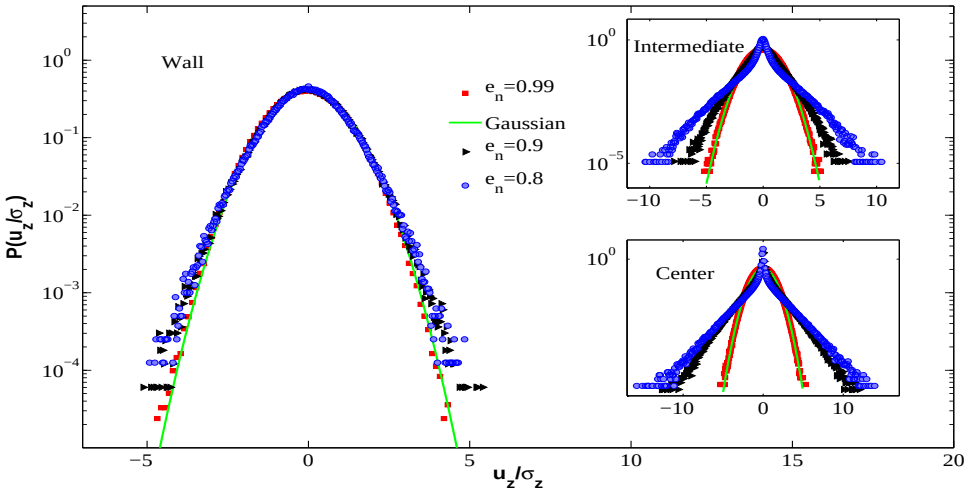

(c)

Figure 5.4: P[u_x] (a), P[u_y] (b) and P[u_z] (c) velocity distribution function for flow between two-parallel plates for different values of e_n (0.99, 0.9 and 0.8), in wall bin (main panel), intermediate bin (top right inset) and center bin (bottom right inset). Gaussian distribution is shown by the solid green line

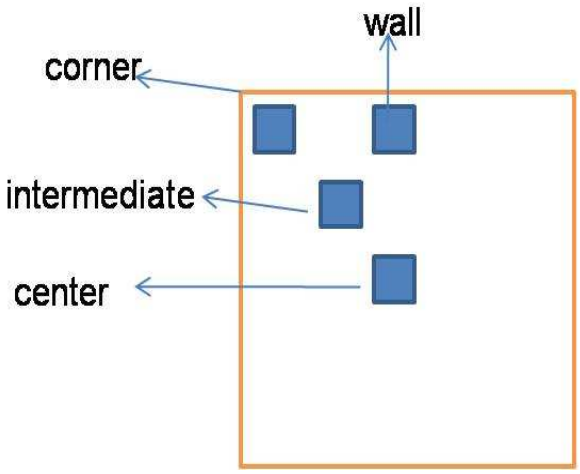

Figure 5.5: Flow in square duct: Schematic of the positions of the bins where the VDF is calculated.

z-direction. Trials are done for three values of e_n - 0.99, 0.9 and 0.8. The value of $e_{wy} = 1.0$, $e_{wz} = 1.0$ and $\beta_w = 1.0$ which corresponds to perfectly rough walls.
The VDF for x, y and z velocities are shown in Figs. 5.6a, 5.6b and 5.6c, respectively, in which the main panel shows the distribution in the corner bin [(n_x,n_z)=(1,1)], the upper left inset shows the center bin [(n_x,n_z)=(25,25)], upper right inset shows the wall bin [(n_x,n_z)=(25,1)] and the lower right inset shows the intermediate bin [(n_x,n_z)=(12,12)]. The green line in the figures indicates Gaussian distribution. The positions of all the bins is shown in Fig. 5.5. The following observations are made from the probability distribution plots - (i) the corner bin distribution is symmetric for all velocities, (ii) decrease in e_n leads to longer and denser tails in the corner and the central bin as the particles tend to accumulate, but the same is not seen the wall bin, (iii) inelastic systems ($e_n < 1.0$) have distribution which deviate from the Gaussian distribution. (iv) the distribution in the stream-wise direction is different in the intermediate bin for high inelasticity, there is a dominant peak in the positive direction. (v) the x-distribution in the center bin for lower e_n is asymmetric and has a flatter tail for the negative velocity. This is due to the dense arrangement of the particles in the center of the system.

5.3 Density waves: Method of analysis

As already mentioned, the density waves have been studied previously by Liss *et al.* (2002); Conway & Glasser (2004) and Alam *et al.* (2009). We use the same approach and analyze density waves in 3D Poiseuille flow. In 5.4.1 density waves formed in the flow between parallel plates is studied. Section 5.4.2 deals with density waves formed in flow in a square duct. Transient and steady state behavior is studied under separate subsections.
In case of 2D Poiseuille flows, snapshots are taken at different intervals of time to analyze the different modes of density waves. The system is divided into $N_1 \times N_2$ cells and the density in each cell is found. This density is stored in a matrix ($N_1 \times N_2$).The FFT is applied on this matrix and Fourier coefficients [a(k_x,k_y)] of the Fourier series a(k_x,k_y)exp[$i2\pi([k_x x/L][k_y y/W]$ are found and stored in the matrix X. The power spectrum (P) is obtained from the following

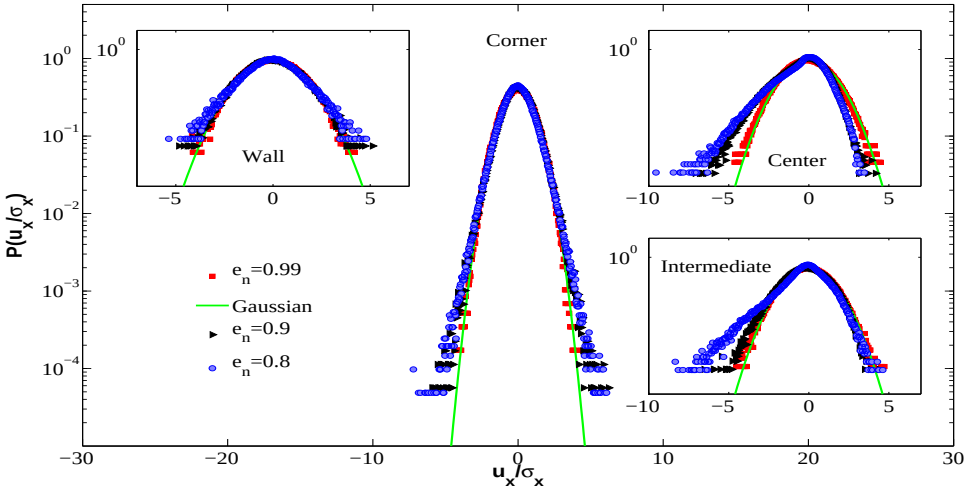

(a)

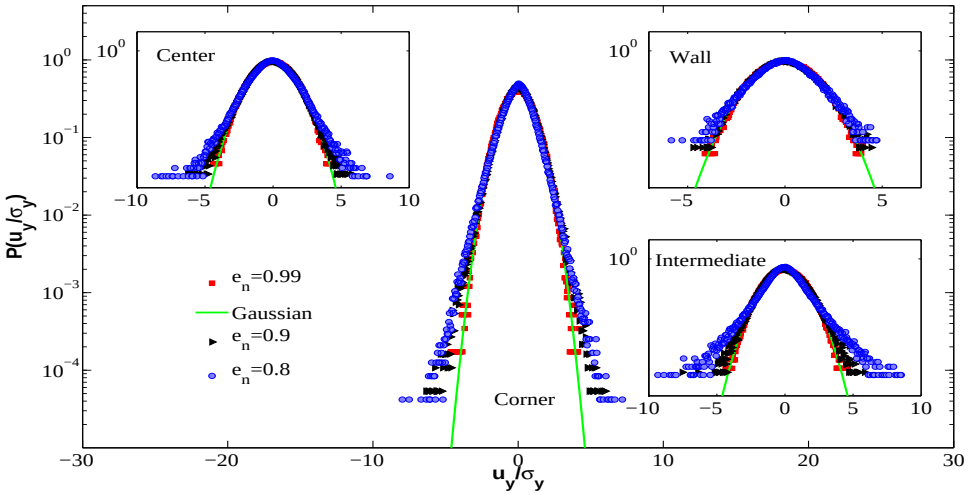

(b)

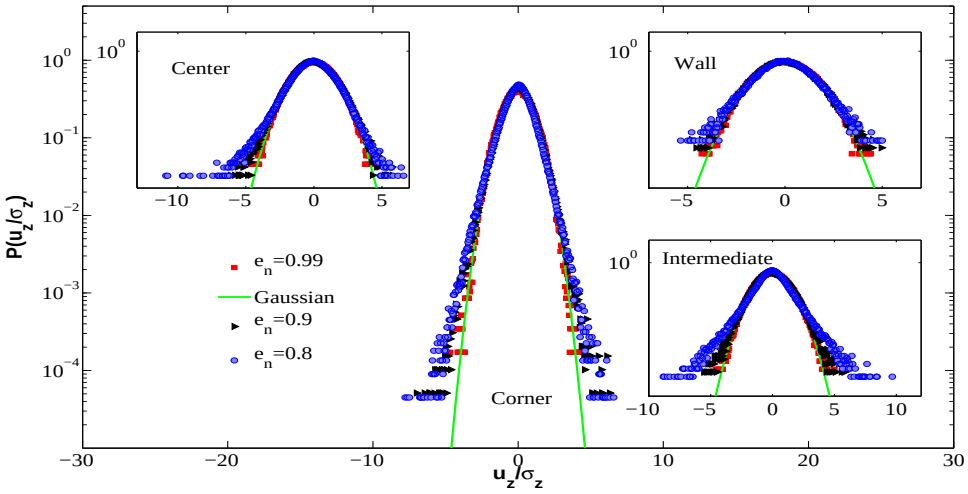

(c)

Figure 5.6: P[u$_x$] (a), P[u$_y$] (b) and P[u$_z$] (c) velocity distribution function for flow in a square duct, for different values of e_n (0.99, 0.9 and 0.8), in corner bin (main panel), wall bin (top right inset), intermediate bin (bottom right inset) and center bin (top left inset). Gaussian distribution is shown by the solid green line

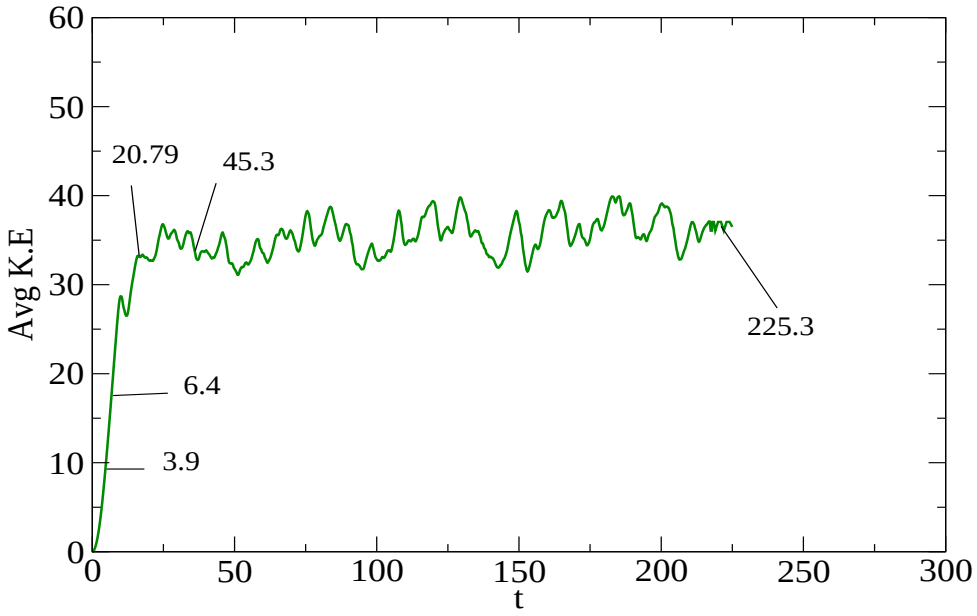

Figure 5.7: Flow between 2 plates: Average kinetic energy versus time curve for e_n=0.85, β_{wz}=-0.6, W/d=60, L/W=2.0, D/W=1.0, N=125000

equation :

$$P = \frac{2X.conj(X)}{(N_1 N_2)^2} \tag{5.1}$$

The power spectrum is normalized by the size of the matrix to remove the dependence of the chosen mesh. To eliminate the large peak obtained by the mean density of the system, the (0,0) coefficient of the FFT matrix X is set zero. The primary peaks of the power spectrum are shown in the results. The secondary peaks are ignored since they could be noise.
In order to use the above method in 3D flows, the channel was divided into slices in all three directions. The width of the slice is as per Eq. 2.22. If the flow is symmetric around the central axis as in Fig. 5.9a then the slices can be taken in any part of the channel. But if the flow is asymmetric (Fig. 5.13a) then three slices (one center and two intermediate) equidistant from each other are taken.

5.4 Results on density waves

5.4.1 Flow between two parallel plates

The ratio of L:W:D is set to 2:1:1 in the present section. The width (W/d) is 60.0 and restitution coefficient e_n is 0.85. The walls are present in the y-direction and its properties - β_w, e_w are set to -0.6 and 1.0, respectively. This corresponds to smooth walls. The volume fraction is 0.15 and the number of particles (N) is 125000. Particles are initially positioned in a cubic lattice and the initial velocities in all directions are set by a random number generator. The system evolves with time and finally reaches a steady state when the dissipation in the system is balanced by the external body force (gravity). Fig. 5.7 shows the evolution of average kinetic energy with time. Snapshots of the density waves are taken at various times as indicated in the figure and

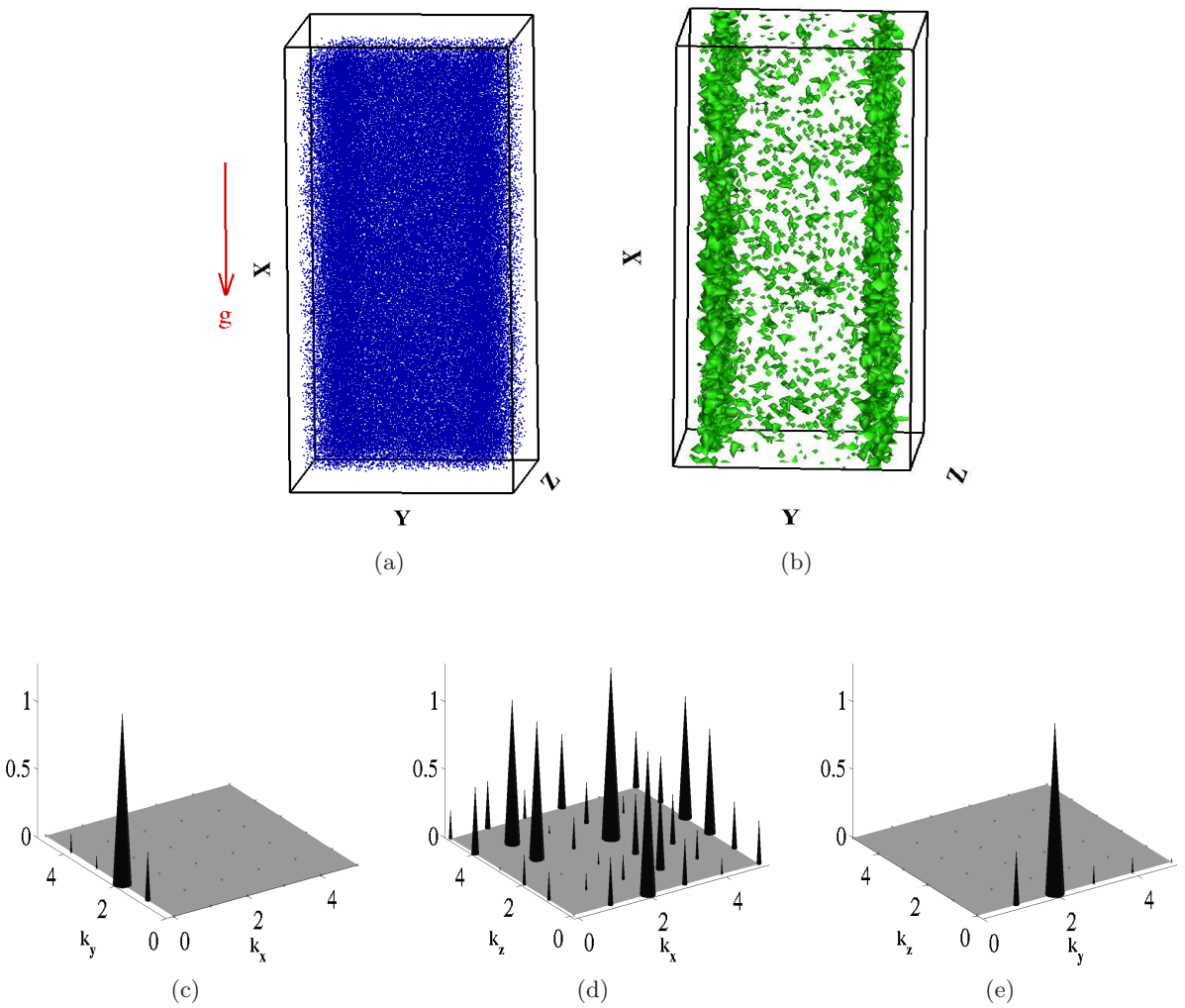

Figure 5.8: Flow between 2 plates: (a) Instantaneous particle positions and (b) density isocontours of a DOUBLE WAVE formed in transient conditions corresponding to t=3.9. Power spectrum of density fluctuations in the central slice taken parallel to XY-plane (c), XZ-plane (d) and YZ-plane (e)

analyzed. 3D isocontours indicating surface of constant density are shown in Figs. 5.8b, 5.9b, 5.10b, 5.13b, 5.14b for better visualization of the structures. All the isocontours are shown for $\sim 0.5 \times \nu_{max}$.

Transient behavior

In this section we will discuss the different density waves formed before the average kinetic energy of the system stabilizes.

t=3.9

Initially, it is seen that upon collision, particles clump up near the walls. Thus, two clumps are formed near the wall as seen in the instantaneous particle positions (Fig. 5.8a) and density-isocontours (Fig. 5.8b). In order to analyze the system in detail the channel is divided into various slices in all three direction. As the system is symmetric along all directions, we can analyze any one slice taken at any distance from the origin. Hence, for this snapshot, the power spectrum of the x, y and z-slices are calculated in the center of the channel. A slice taken parallel to XZ-plane, yields a power spectrum with no dominant peak as shown in 5.8d. This tells that

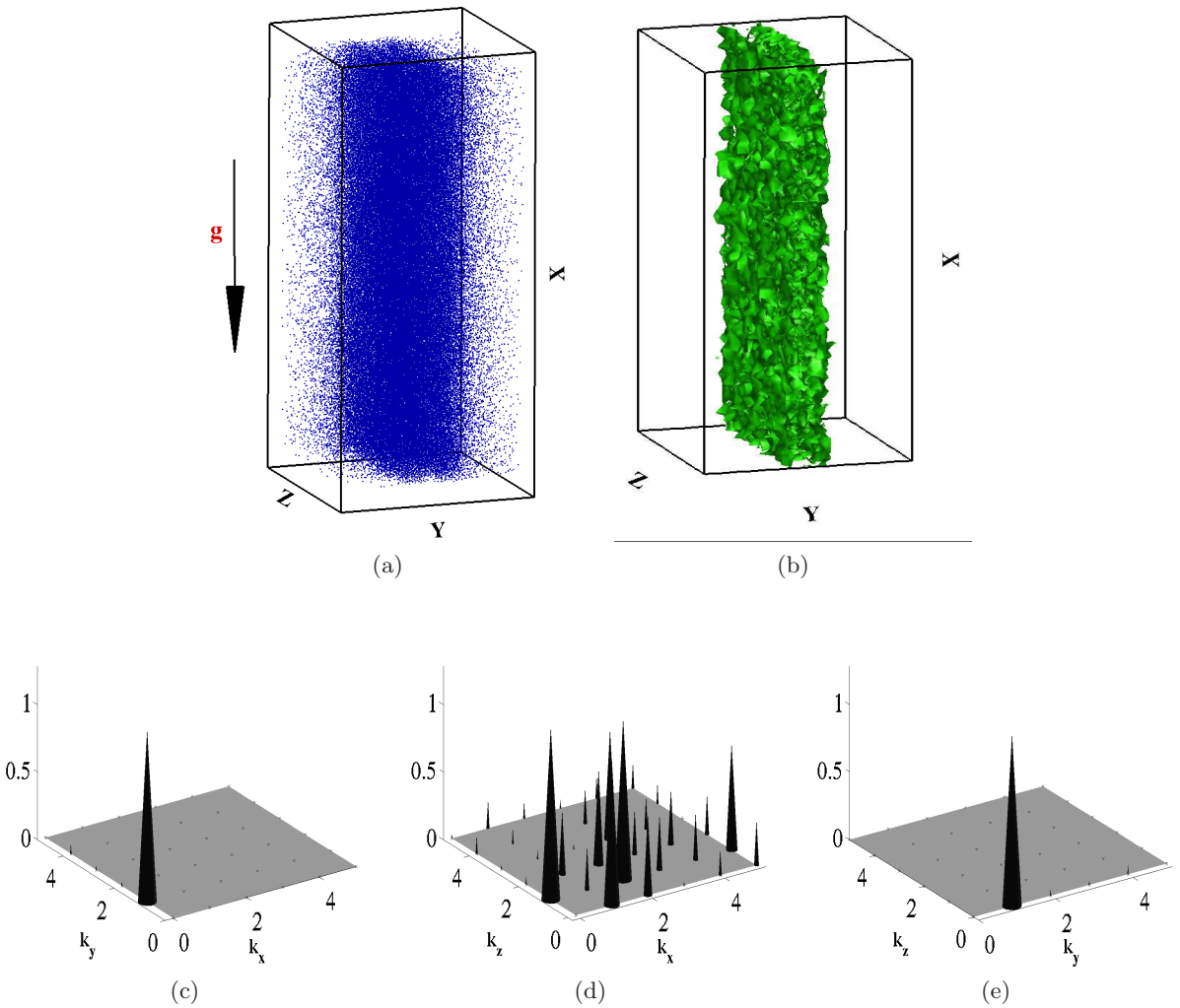

Figure 5.9: Flow between 2 plates: (a) Instantaneous particle positions and (b) density isocontours of PLUG FLOW formed in transient conditions corresponding to t=6.4. Power spectrum of density fluctuations in the central slice taken parallel to XY-plane (c), XZ-plane (d) and YZ-plane (e).

the system is homogeneous in all slices taken along the y-direction. The power spectrum of a slice parallel to XY-plane (Fig. 5.8c) shows a dominant peak at (k_x,k_y)=(0,2) which correspond to the double wave. A slice taken parallel to the YZ-plane also shows a similar second mode (k_z, k_y)=(0,2) as seen in Fig. 5.8e.

t=6.4

It is seen that as the system evolves further, there is gradual migration of both these density structures from the wall towards the center to form a single dense plug. It is also observed that the density structures which originate from the wall, grow in size as they move towards the center of the system. The instantaneous particle positions and the density-isocontours are shown the Figs. 5.9a and 5.9b. Both these figures show that the system is symmetric along the all planes drawn in the center of the system. Thus, this makes the analysis simpler as we can take a slice in any part of the system. For uniformity in analysis we consider the central slice. Power spectrum of the slice taken parallel to YZ-plane (Fig. 5.9e) shows a peak at (k_y=1,k_z=0) which is characteristic of plug flow. Similarly a slice parallel to XY-plane shows a peak in the

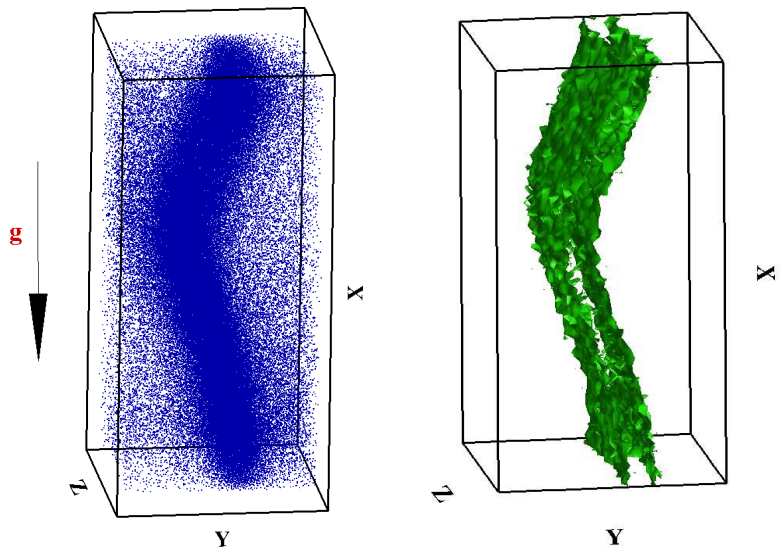

(a) (b)

Figure 5.10: Flow between 2 plates: Instantaneous particle positions (a) and density isocontours (b) in a SYMMETRIC wave at t = 20.79

y-direction (k_y=1,k_x=0) as shown in Fig. 5.9c. A bin parallel to XZ-plane shows no distinct peak which tell that system is homogeneous in the bins along y-direction (Fig. 5.9d).

Steady state behavior

t=20.79

We have seen till now that particles accumulate in the center of the system in the form of a thick dense sheet which is symmetric in all direction. As the simulation progresses, this dense sheet of particle in the center deforms as shown in Figs. 5.10a and 5.10b. If an XY-plane is drawn in the center of the system then we see that the density wave is symmetric across the plane (Fig. 5.11a). So, we analyze the power spectrum in the central slice only (Fig. 5.11c). It indicates a dominant peak at (k_y,k_x)=(1,0) and a small peak at (k_y,k_x)=(1,1) which corresponds to the symmetric wave as reported by the previous works. The density profile of the slices taken parallel to YZ-plane is shown in Fig. 5.11b. The power spectrum of the central slice (Fig. 5.11d) shows a dominant peak at (k_y,k_z)=(1,0) and a small peak at (k_y,k_z)=(2,0). Finally, as the system is asymmetric across the central XZ-plane (Fig. 5.12a), power spectrum is calculated in two intermediate (bin=7 and 22) bins and a central bin (bin=15). The power spectrum in the central slice shows peaks at (k_x,k_z)=(2,0) as we have to cut through the density wave.

t=45.3

Beyond this stage the density wave deforms in all direction leading to asymmetric wave. The particle positions and the density-isocontours in the center of the bin are shown in Fig. 5.13a and Fig. 5.13b. Power spectrum calculated for the center slices are only shown. The slice taken along parallel to XY-plane, shows a dominant peak at (k_x,k_y)=(1,1) and a minor peak at (k_x,k_y)=(0,1) as seen in Fig. 5.13c. The major peak at (k_x,k_y)=(1,1) tells that there is significant density variation in the x-direction as well as y-direction which is characteristic in asymmetric mode. The power spectrum of the slices taken in other two direction (Figs. 5.13d, 5.13e) yield results similar to the symmetric wave.

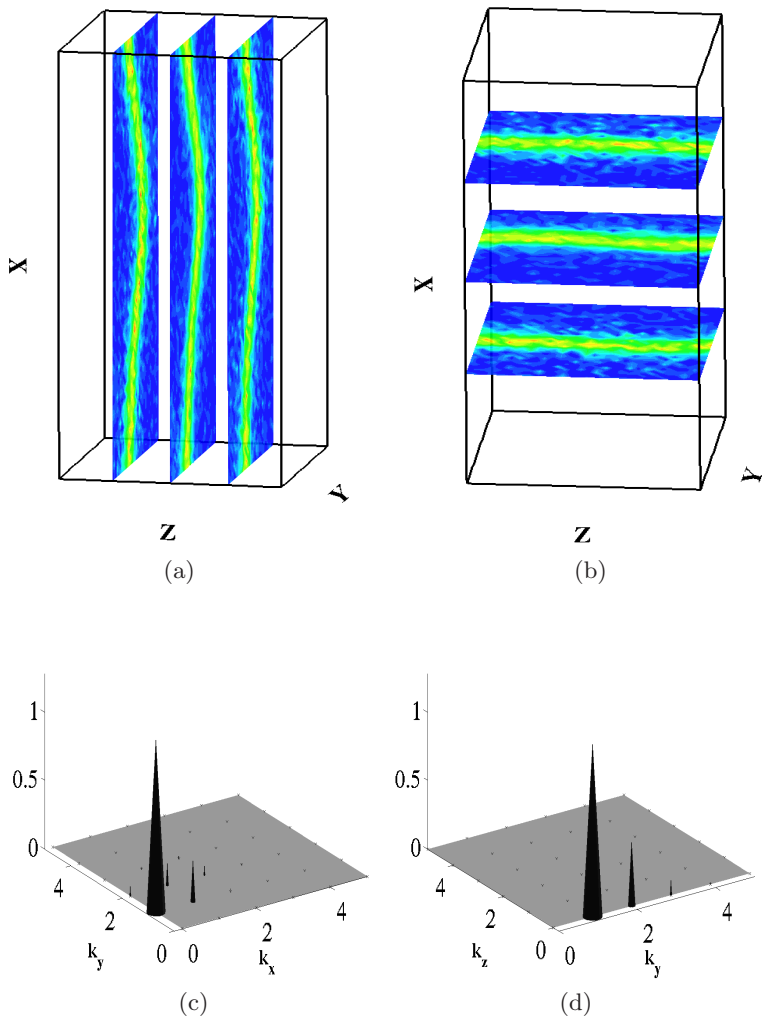

Figure 5.11: Flow between 2 plates: Density profiles in middle and intermediate bins parallel to (a) XY-plane and (b) YZ-plane in SYMMETRIC wave at t = 20.79. The power spectrum of the central slice corresponding to (a) and (b) are shown in (c) and (d), respectively.

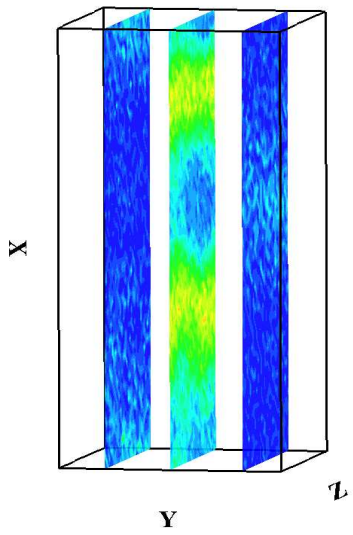

(a)

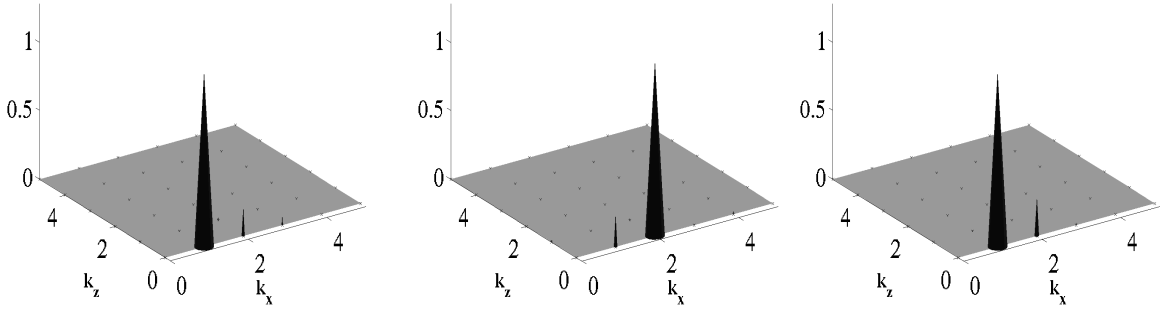

(b) (c) (d)

Figure 5.12: Flow between 2 plates: (a) Slices taken parallel to XZ-plane showing density profile in central (bin=15) and intermediate (bin=7 and 22) bins in SYMMETRIC wave at t=20.79. Power spectrum analysis of the slices taken at bin=7 (a), 15 (b) and 22 (c).

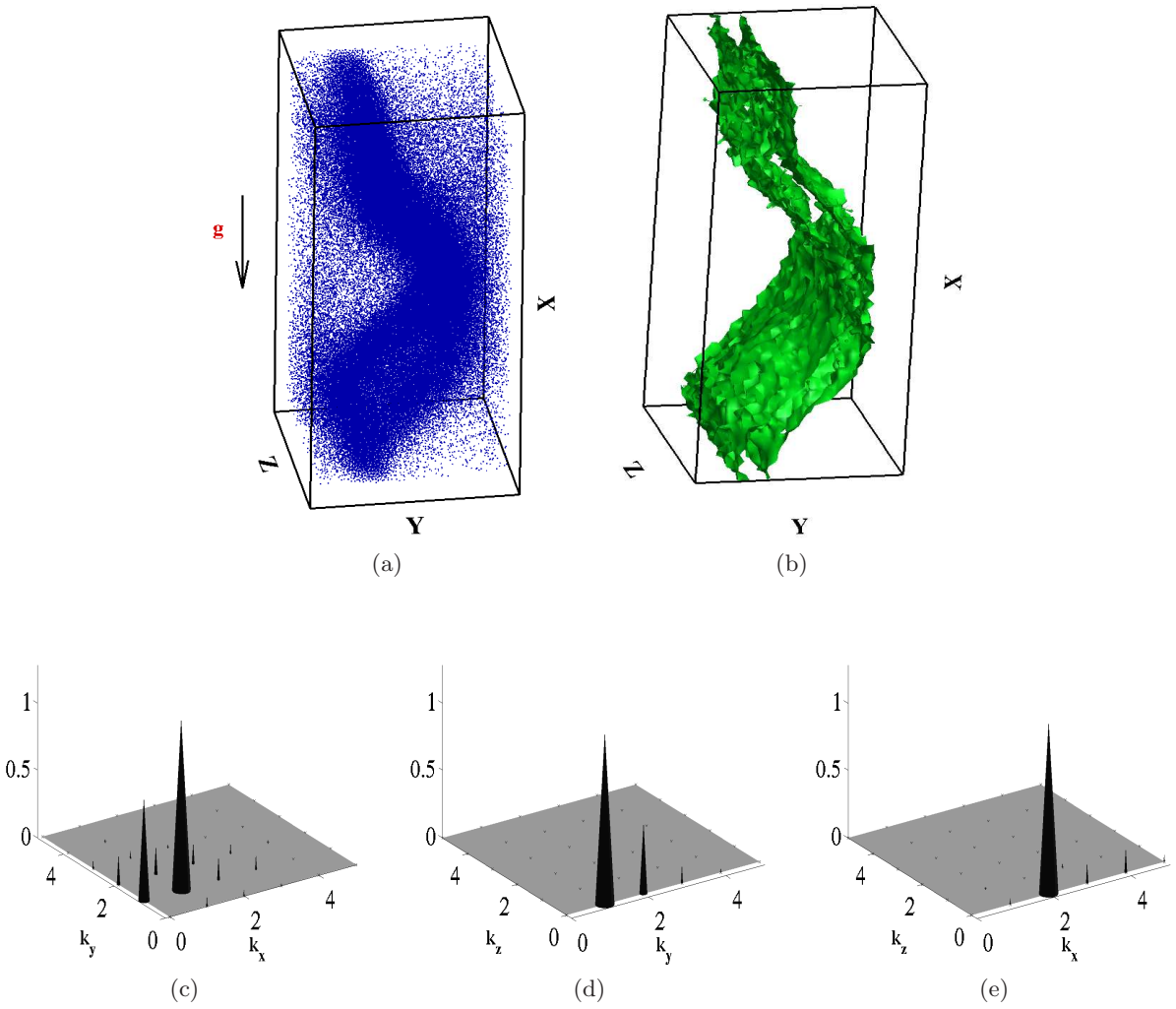

Figure 5.13: Flow between 2 plates: (a) Instantaneous particle positions and (b) density isocontours of ASYMMETRIC WAVE formed in transient conditions corresponding to t=45.3. Power spectrum of density fluctuations in the central slice taken parallel to XY-plane (c), YZ-plane (d) and XZ-plane (e).

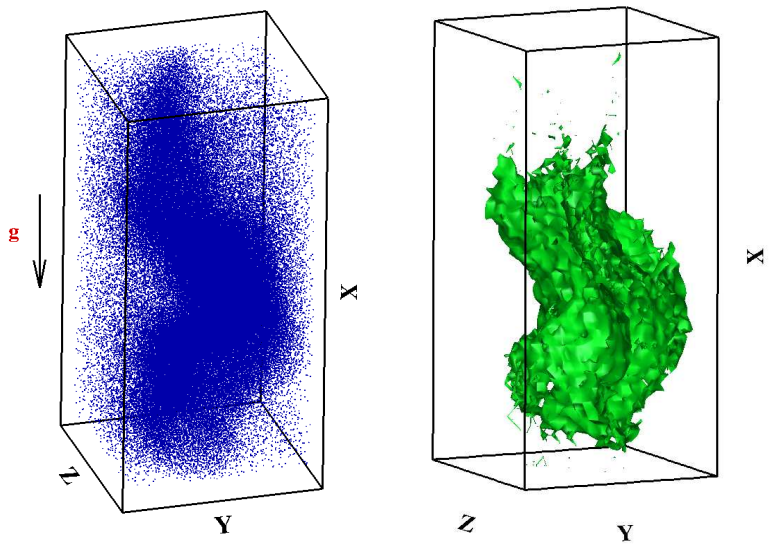

(a) (b)

Figure 5.14: Flow between 2 plates: Instantaneous particle positions (a) and density isocontours (b) in a SLUG flow at t = 225.3.

t=225.3

After a long time all the particles clump at the center of the system and move along the direction of gravity. This kind of flow is called slug flow (Figs. 5.14a and 5.14b). The slices taken parallel to XZ-plane are shown in Fig. 5.15a and their corresponding dominant modes are shown in Figs. 5.15d, 5.15e and 5.15f. The slices taken parallel to XY-plane have a well defined shape. The structure has a dense thick central belly surrounded by a thin but dense head and tail region. Power spectrum analysis reveals similar dominant peaks in all slices. The dominant peaks are (k_x,k_y)=(1,0), (1,1), and (0,1). Density contours of bins parallel to YZ-plane is shown in Fig. 5.15c and the dominant peaks [Figs. 5.15j, 5.15k, 5.15l] in all these slices is (k_x,k_y)=(0,1).

Multiple clumps

In the previous section a single clump is found in the center of the channel. As the length of the system is increased multiple clumps are observed. Instantaneous particle positions are shown for ν = 0.06, N=14000, L:W:D = 1:15:1 and W/d = 20.0. Figure 5.16a shows that at the initial t=22.85, two clumps are seen in the system. These clumps come close to each other (Fig. 5.16b) and merge to form a single dense slug at the center of the channel (Fig. 5.16c). As the simulation progresses, a second dense clump reappears along the channel length (Fig. 5.16d). This process of formation and merging of clumps along the direction of gravity happens constantly throughout the simulations.

5.4.2 Flow through a square duct

The formation of density waves in a square duct is more complicated than flow between two parallel plates. The non-uniformity in the dissipation along the walls due to the presence of four corners is the major reason. The dissipation due to wall collisions in the corner is significantly higher compared to other points along the walls.

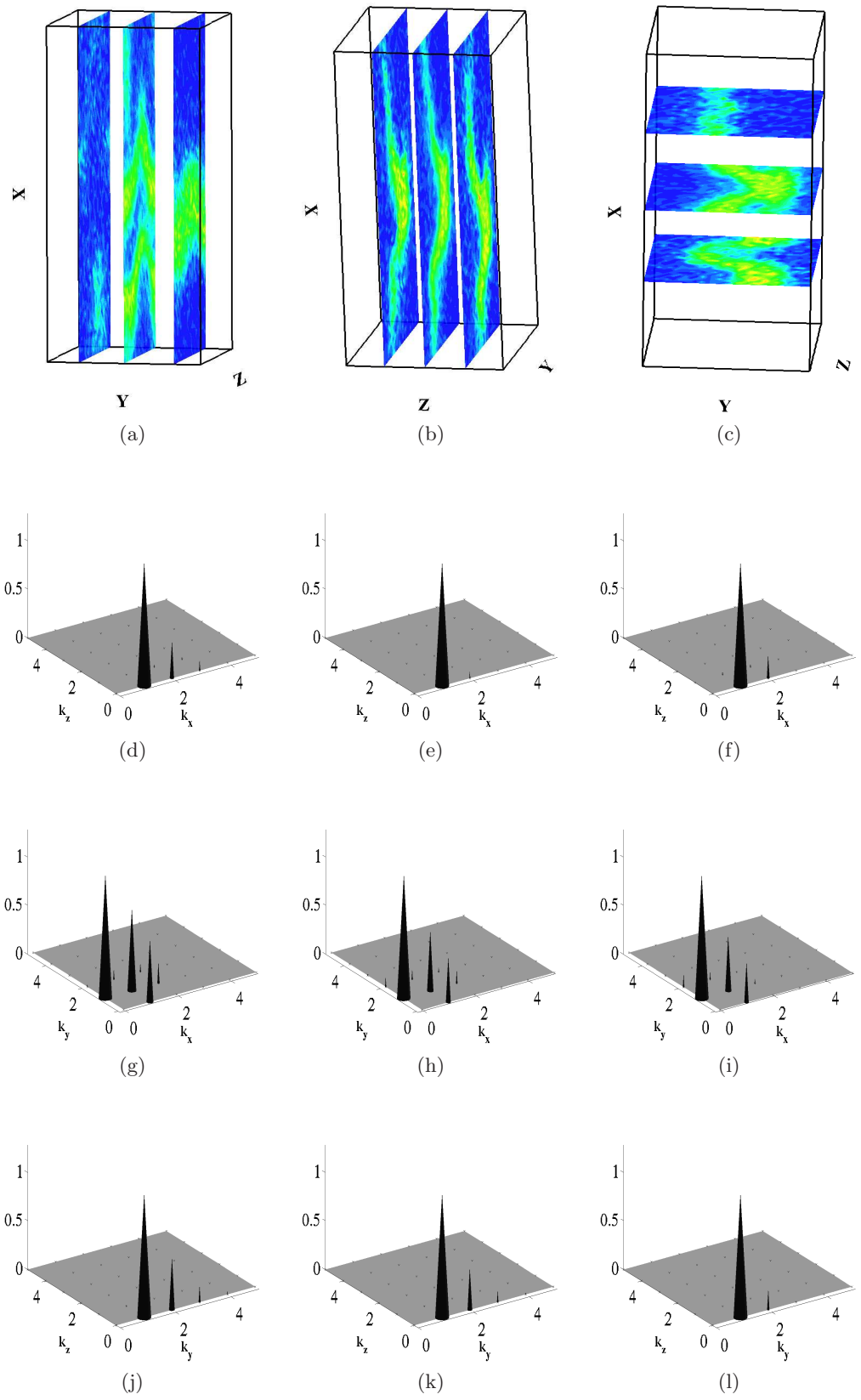

Figure 5.15: Flow between 2 plates: Density profile in central and intermediate slices taken parallel to XZ (a), XY(b) and YZ(c) for SLUG flow at t=225.3. Power spectrum of slices taken parallel to XZ-plane in bin=7,15 and 22 are shown in (d), (e) and (f). Power spectrum of slices taken parallel to XY-plane in bin=7,15 and 22 are shown in (g), (h) and (i). Power spectrum of slices taken parallel to XY-plane in bin=15, 30 and 45 are shown in (j), (k) and (l).

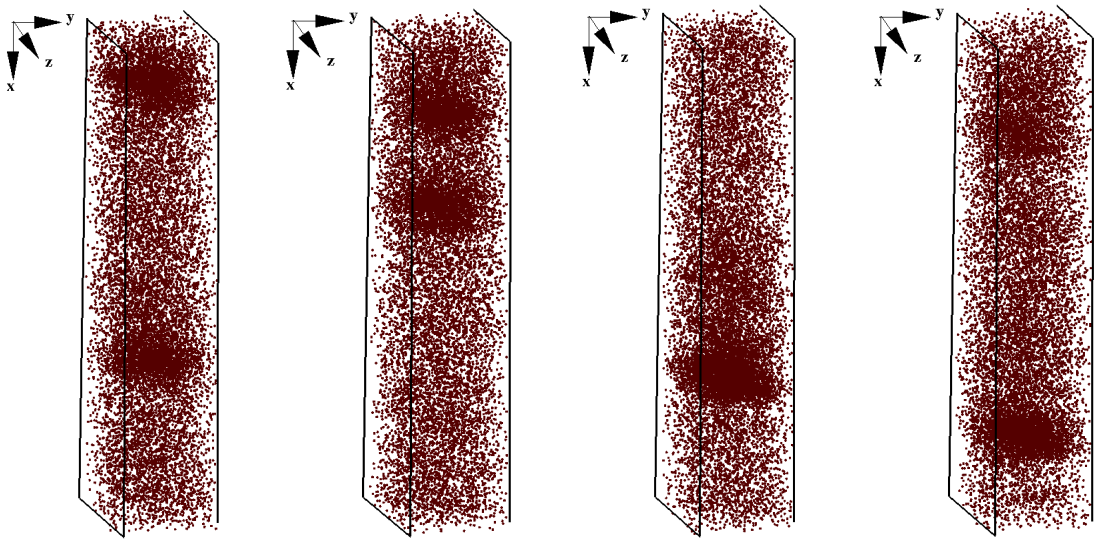

Figure 5.16: Flow between 2 plates: Instantaneous particle positions at (a) t=22.85, (b) t=46.07 (c) t=54.35 and (d) t= 61.5 showing multiple clumps. Parameters are $\nu = 0.06$, L:W:D = 1:15:1, W/d = 20.0 and N = 14000.

The plot of average kinetic energy evolution with time is shown in the Fig. 5.17. The points of investigation are marked on the curve. The ratio of the system dimensions, L:W:D, is set to 2:1:1. The coefficient of particle-particle restitution is set to 0.85, the wall tangential restitution coefficient β_w=-0.6 and the wall normal restitution coefficients (e_{wy} and e_{wz}) are 1.0. The density waves will be studied separately in two different sections - transient and steady state. The initial configuration is set to square lattice. When the system is allowed to evolve it is observed that the average kinetic energy of the system initially changes with time and it later stabilizes. The structures formed when the average kinetic energy is changing is studied under transient behavior and those formed once the average kinetic energy stabilizes is studied under the topic - steady state behavior. The time at which the snapshots are taken are shown in Fig. 5.17. Density-isocontours in Figs. 5.18b, 5.21b, 5.22b, 5.24b, 5.25b are shown for $\sim 0.5 \times \nu_{max}$.

Transient behavior

t=5.9

Similar to flow in parallel plates, density waves originate from the walls. But what is important are the four dense pillar like structures emerging from the corners of the system. The density-isocontours and instantaneous particle positions is shown in Figs. 5.18b and 5.18a. The system is symmetric across XY, YZ and ZX planes drawn at the center of the channel. Slices taken parallel to XY-plane are shown in 5.19a. The power spectrum of center and intermediate bins are shown in Figs. 5.19b and 5.19c, respectively. The central slice shows a dominant mode at (k_x,k_y)=(0,2) and two minor peaks at (k_x,k_y)=(0,1), (0,3). The intermediate bin which includes the waves emerging from the wall, has an additional mode of (k_x,k_y)=(0,3) along with (k_x,k_y)=(0,2). The (k_x,k_y)=(0,3) mode represents a wave having secondary variations across the channel with three spatial periods. This might be related to the secondary instability of

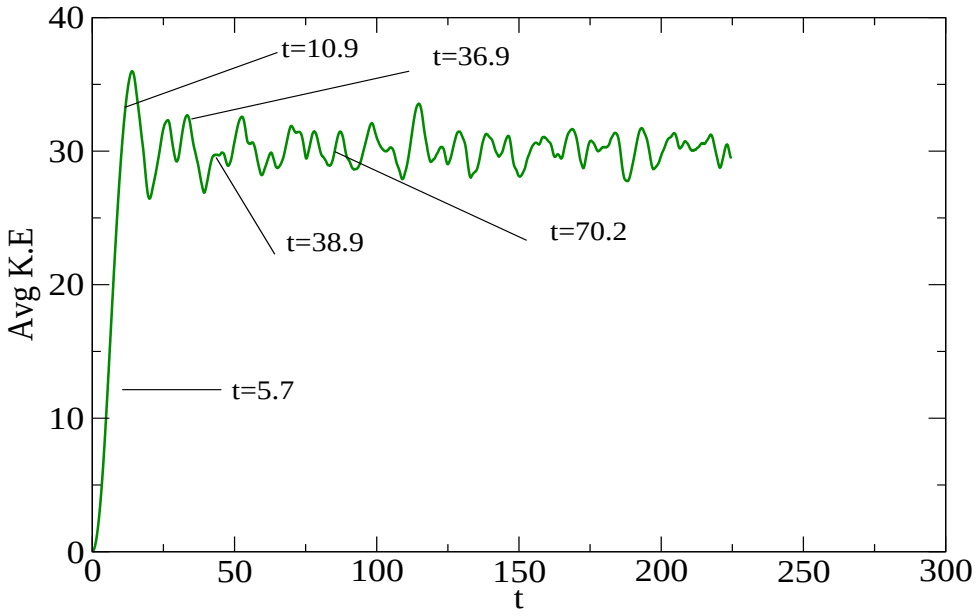

Figure 5.17: Flow in a square duct: Average kinetic energy versus time curve e_n=0.85, β_w=-0.6, W/d=60, L/W=2.0, D/W=1.0

the plug flow. The slice taken in the plane parallel to YZ-plane is shown in Fig. 5.20a and the power spectrum shows peaks at (k_x,k_y)=(0,2) and (2,0) as seen in Fig. 5.20b. These two peaks clearly represent a square-wave.

t=10.9

As the simulation proceeds the density waves emerging from the walls merge in the center of the system to form a cylindrical plug (Figs. 5.21a, 5.21b). As the system is symmetric power spectrum analysis is done for central slices in all direction (Figs. 5.21c, 5.21e and 5.21d). A slice taken parallel to YZ-plane shows a central circular dense region which corresponds to (k_y,k_z)=(1,0), (0,1) in the power spectrum. An additional peak at (1,1) appears in flow in a square duct is an effect of the corners. The slice along the planes parallel to XY and XZ-plane are similar and the power spectrum shows a dominant peak at k_y=1.

Steady state behavior

t=36.9

Further on, the cylindrical plug deforms to form a wavy structure but almost preserving the the diameter of the cylinder. The instantaneous particle positions and density-isocontours are shown in Fig. 5.22a and 5.22b. Slices taken along plane parallel to YZ-plane are shown in Fig. 5.22c. The dense center appears at different positions in the YZ-planes in different slices. The power spectrum of this (Fig. 5.22f) shows a peak at (k_y,k_z)=(1,0), (0,1) and (1,1). This (1,1) peak is a wall effect and is comparatively higher than that seen for a plug flow (5.21c). This is because as the simulation proceeds more and more particles accumulate at the corners leading to increased influence of the corner regions on the power spectrum. The slice taken at the center in the plane parallel to XZ-plane shows a dominant peak at (k_x,k_z)=(1,0) and (1,1) [Fig. 5.22g] which is a feature of a symmetric wave. The central slice in the z-direction shows peak at (k_x,k_y)=(0,1) as seen in Fig. 5.22h.

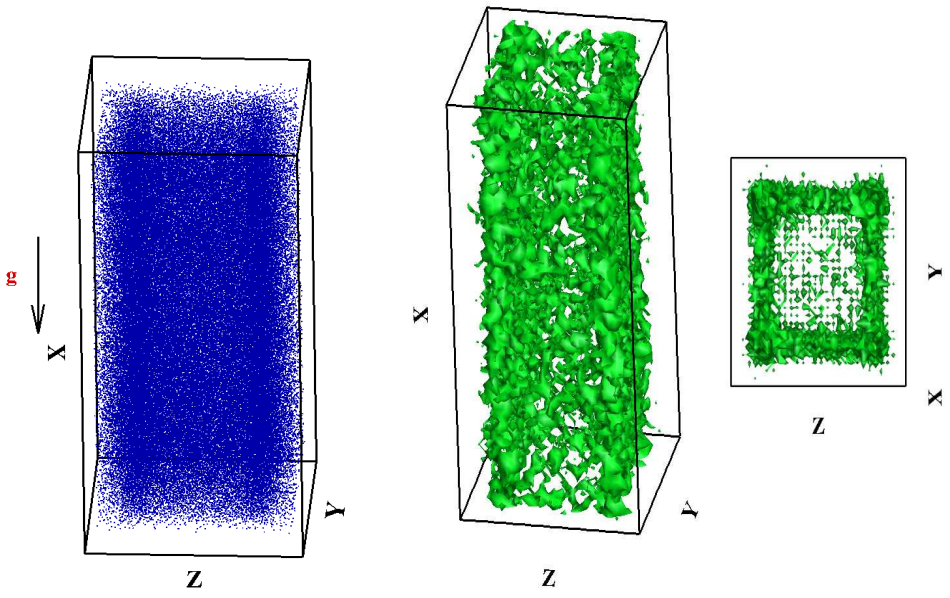

(a) (b)

Figure 5.18: Flow in a square duct: (a) Instantaneous particle positions and (b) density isocontours at t=5.9 for SQUARE wave.

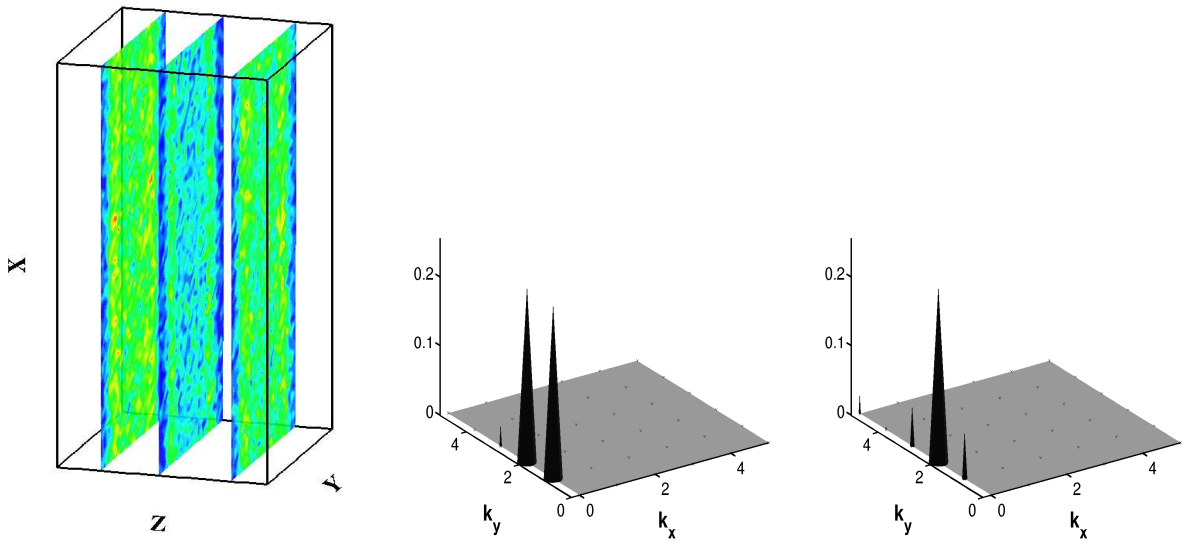

(a) (b) (c)

Figure 5.19: Flow in a square duct: (a) Density profile of slices taken parallel to XY-plane in the intermediate (bin=7 and 22) and central (bin=15) bins at t=5.9. Power spectrum of density fluctuations in bin=7 (b) and bin=15 (c)

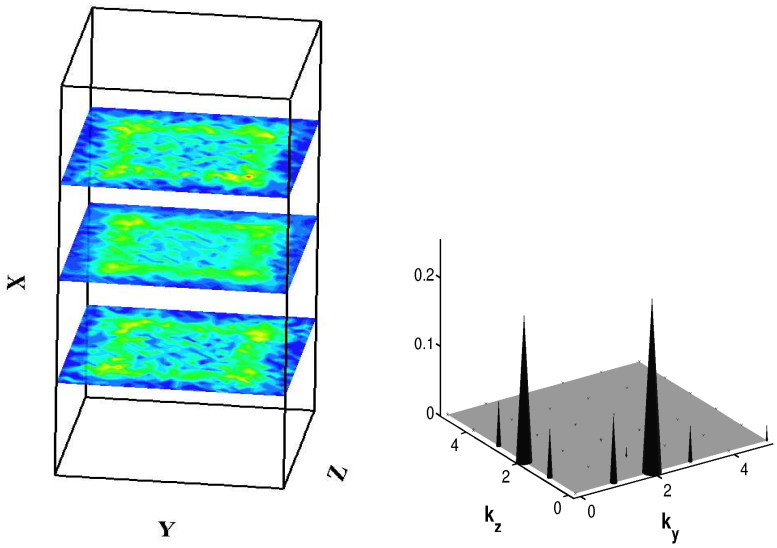

(a) (b)

Figure 5.20: Flow in a square duct: (a) Density profile of slices taken parallel to YZ-plane in the intermediate (bin=15 and 45) and central (bin=30) bins at t=5.9. (c) Power spectrum of density fluctuations in bin=30

t=38.9

The cross section of the cylindrical central plug remains almost constant along x-axis in case of the symmetric wave. When the cross section starts to vary then such a wave is called asymmetric wave. The instantaneous particle positions and density-isocontours in Figs. 5.24a and 5.24b show a flattened density wave. Fig. 5.24c shows that the density center is non-circular and occurs at different positions in the YZ-plane at different positions along x-axis. The density profile in the central XZ-plane is shown in Fig. 5.24d. The corresponding power spectrum is shown in Fig. 5.24g. (k_x,k_y)=(1,1) is enhanced compared to the plug flow which is a feature of asymmetric density wave. The slice taken parallel to XY-plane at the channel center is shown in Fig. 5.24e and the power spectrum of the same is shown in Fig. 5.24h.

Beyond this point, dense corners begin to influence the structures at the center of the system. This can be seen by taking snapshots of particle positions at different times. Top view of the instantaneous particle positions of the system taken at t = 60.8 is shown in Fig. 5.23a. It shows that the density wave at the center is influenced by the corners on the same side whereas, Fig. 5.23b taken at t = 70.2 shows that the diagonally opposite corners influence on the central density wave. The effect of accumulation at the corners can seen more clearly in the next section 5.5.

t=70.2

After a long period of time when the system stabilizes, a density wave exhibits a slug flow as shown in Figs. 5.25a and 5.25b. The slices taken parallel to the YZ-plane (Fig. 5.25c) shows that the high density regions (represented by yellow color) of different sizes at different positions along x-direction. The power spectrum of the central plane parallel to YZ-plane is shown in Fig. 5.25f. The dominant modes are located at (k_y,k_z)=(1,0),(1,1),(0,1). Slices taken in the plane parallel to XY-plane (Fig. 5.25d) do not show any distinct shape but it does indicate that the intermediate bins show regions of high density unlike the previous types of waves. The power

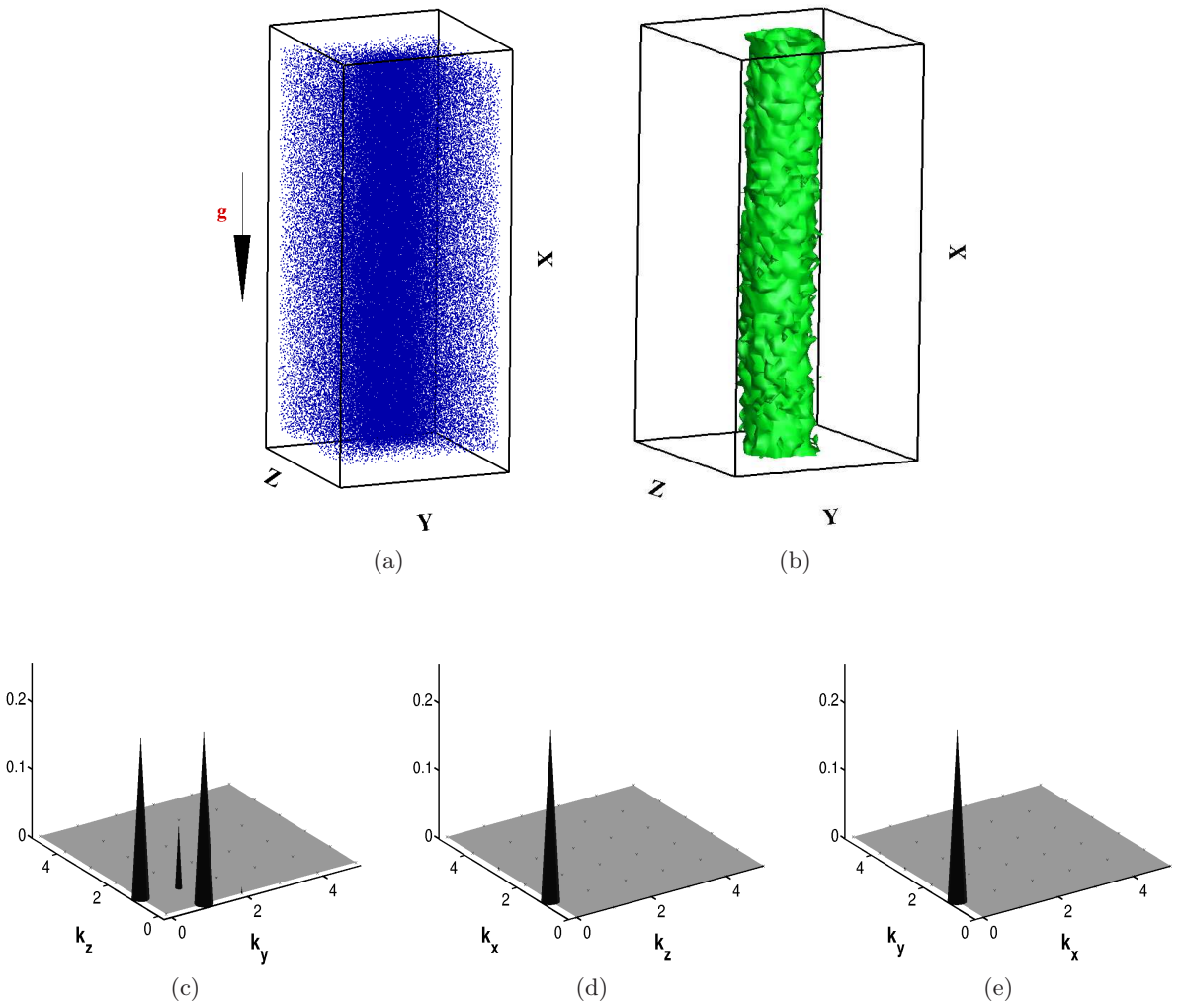

Figure 5.21: Flow in a square duct: (a) Instantaneous particle positions and (b) density isocontours of PLUG flow formed in transient conditions corresponding to t=10.9. Power spectrum of density fluctuations in the central slice taken parallel to YZ-plane (c), XZ-plane (d) and XY-plane (e).

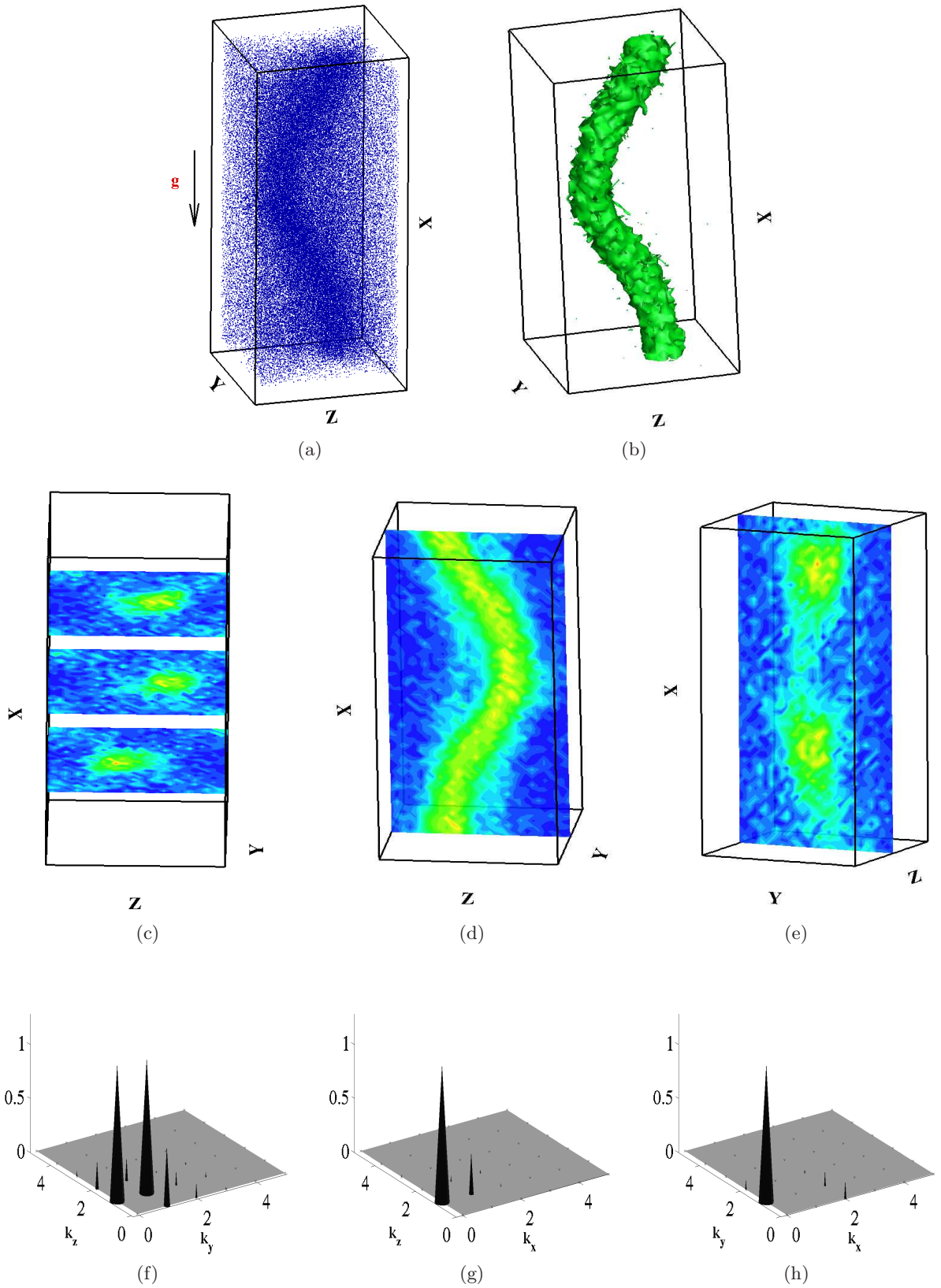

Figure 5.22: Flow in a square duct: (a) Instantaneous particle positions and (b) density iso-contours of SYMMETRIC flow formed at t=36.9. Density profile of slices taken parallel to YZ-plane (c), XZ-plane (d) and XY-plane (e). The corresponding power spectrum of the central slices are shown in (f), (g) and (h).

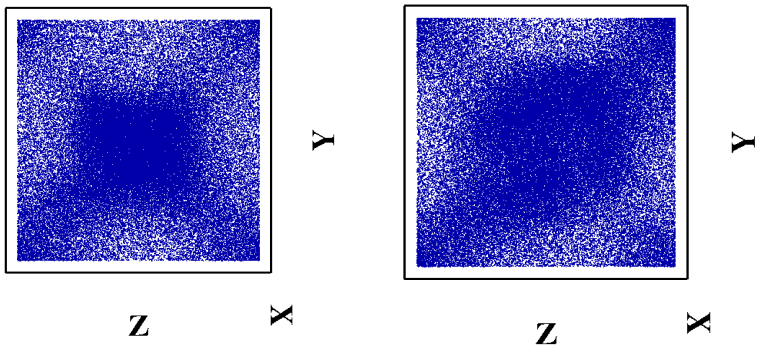

(a) (b)

Figure 5.23: Flow in a square duct: Top view of the system showing instantaneous particle positions at t = 60.8 (a) and 70.2 (b) to indicate that the dense corners interact with the density wave at the center.

spectrum of its central slice is shown in Fig.5.25g. The central slice of the plane parallel to XZ-plane shown in Figs. 5.25e. It shows a definite slug flow with a large dense region surrounded by a head and a tail-like dense regions. The power spectrum (Fig. 5.25h) shows dominant peaks at (k_x,k_z)=(1,0),(1,1),(0,1).

5.5 Flow in a rectangular duct

Asymmetry leads to very interesting effects in duct flow. For flow in a square duct (Sec. 5.4.2), a single density wave occurred at the center of the system (Fig. 5.25a). Once the duct of the system is made rectangular, the separation of density waves occurs as we discuss below.
Fig. 5.26 shows the mean stream-wise velocity and density profiles at three different ratios of W:D - 4:1, 6:1 and 12:1. The density profile for W:D=4:1 (Fig. 5.26b) shows two mean density waves whose peaks are equidistant from the channel center. The mean velocity plot also shows a lobed profile corresponding to the positions of high density (Fig. 5.26a). As the ratio of width to depth is increased, along with the dense regions near the corners, additional smaller dense region near the channel center (Fig. 5.26d) develop. The number of these small density regions which appear close to the center is proportional to ratio - W:D of the system. Three of these are seen for W:D=12:1 as shown in Fig. 5.26f.
On analyzing the instantaneous snapshots at different times it was observed that the density waves travel from the center, to the side walls and migrate back to the center. Figs. 5.27a, 5.27b and 5.27c show the top view of instantaneous snapshots taken at t = 65.9, 75.4 and 85.4, respectively, for the system L:W:D=1:6:1. At t=65.9, one can see a central dense region and two small dense regions close to side walls as marked in circles in Fig. 5.27a. Almost uniform density wave appears along the center of the system at t=75.4 (Fig. 5.27b). At t=85.4, most particles are arranged near two side walls as marked on circles (Fig. 5.27c). The system alternates between these three modes throughout the simulation. The density near the corners is relatively high irrespective of the time. Thus, we get two dominant peaks near the corner in the mean volume fraction and velocity profiles. From this we can conclude that the separation of density waves in rectangular ducts is an effect due to the presence of corners.

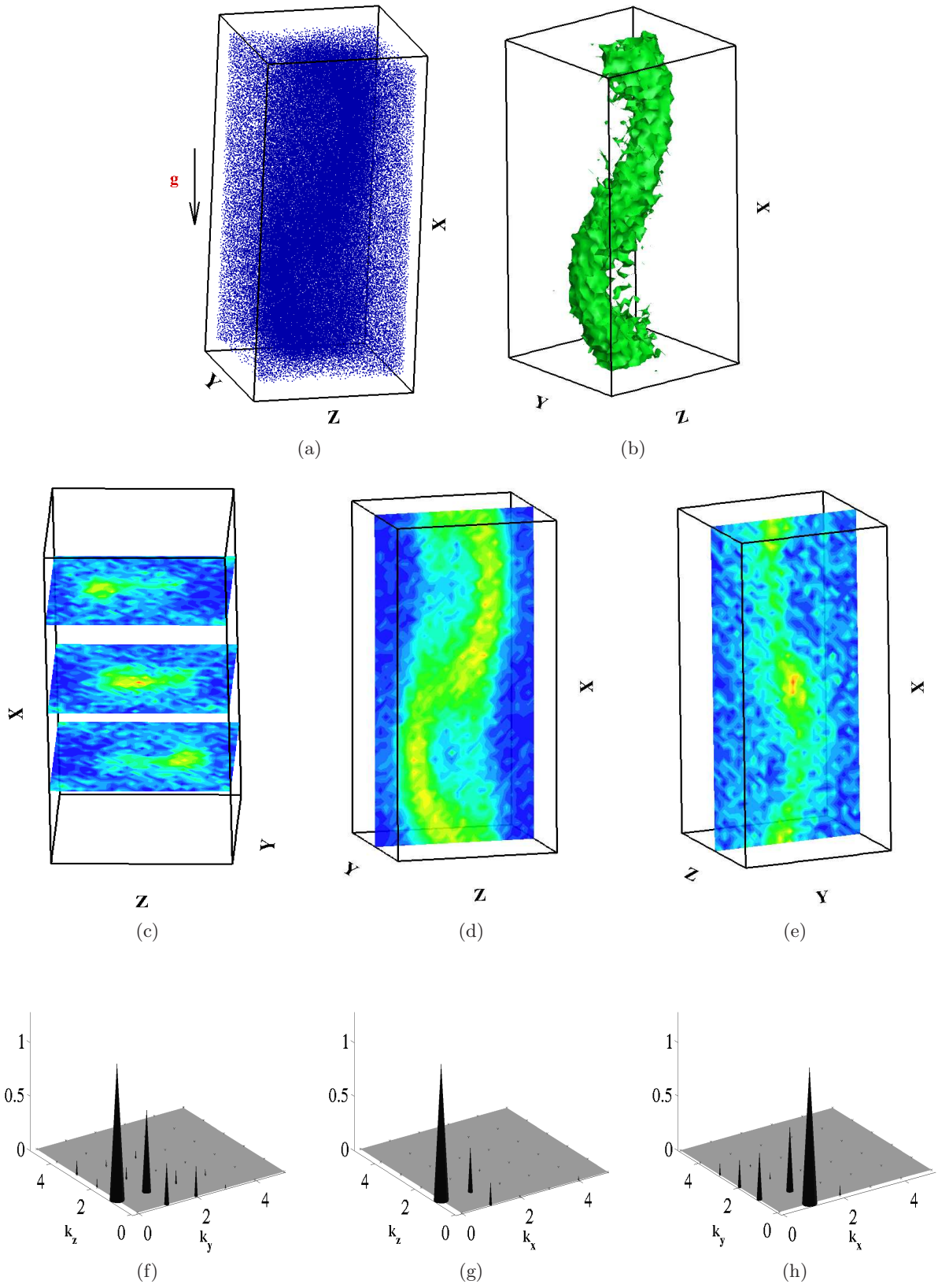

Figure 5.24: Flow in a square duct: (a) Instantaneous particle positions and (b) density isocontours of ASYMMETRIC flow formed at t=38.9. Density profile of slices taken parallel to YZ-plane (c), XZ-plane (d) and XY-plane (e). The corresponding power spectrum of the central slices are shown in (f), (g) and (h).

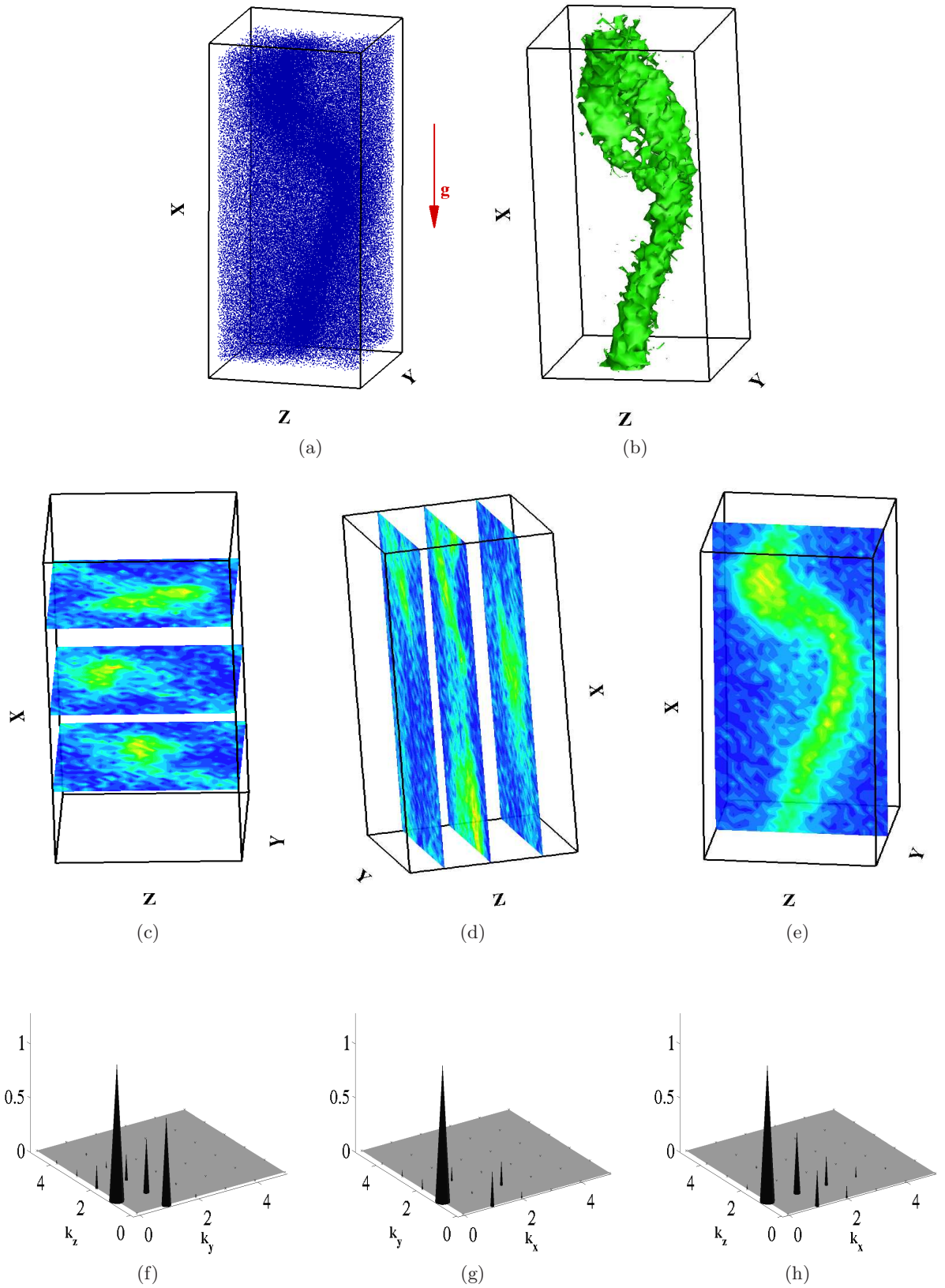

Figure 5.25: Flow in a square duct: (a) Instantaneous particle positions and (b) density isocontours of SLUG flow formed at t=70.2. Density profile of slices taken parallel to YZ-plane (c), XZ-plane (d) and XY-plane (e). The corresponding power spectrum of the central slices are shown in (f), (g) and (h).

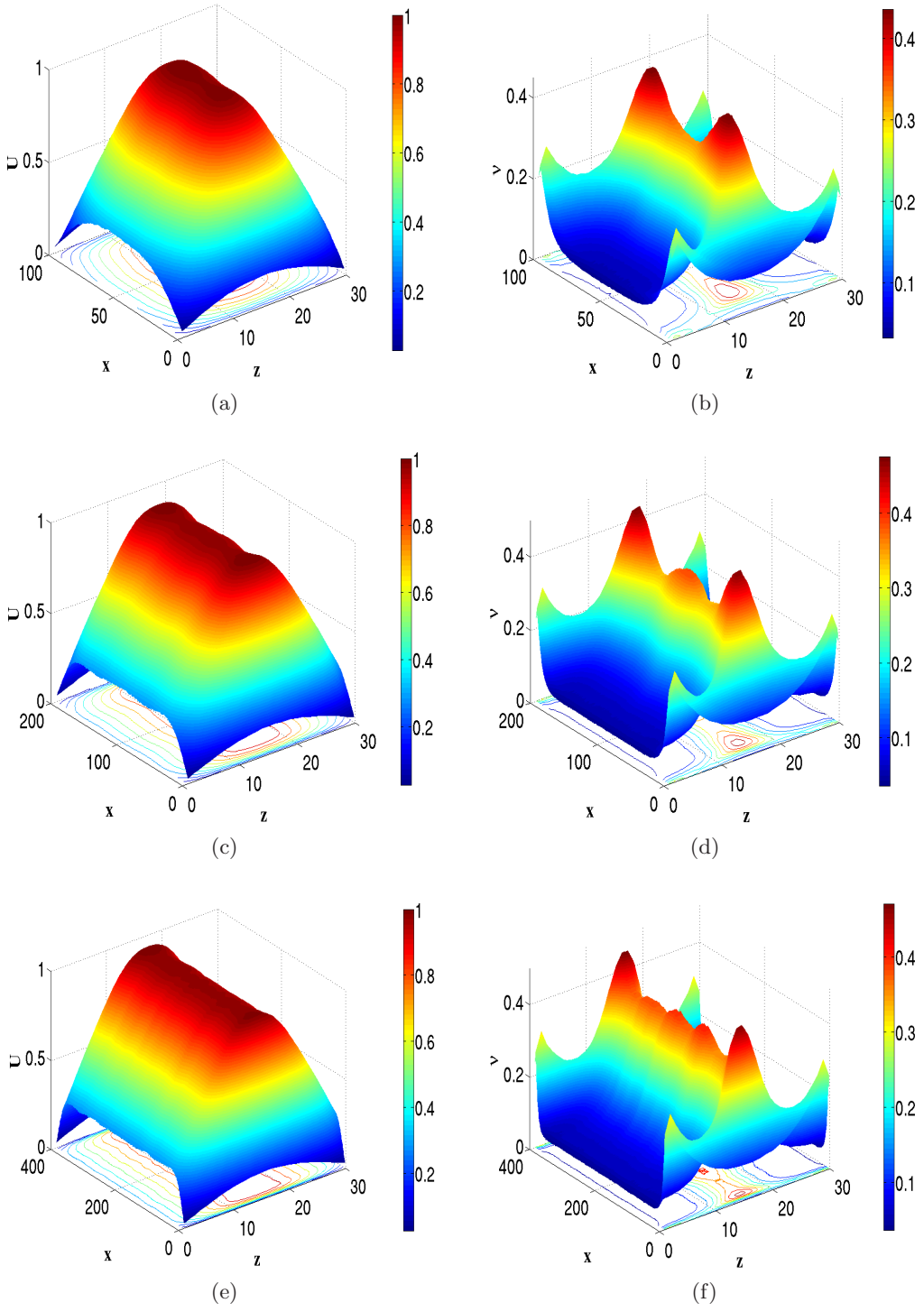

Figure 5.26: Flow in a rectangular duct: Volume fraction (ν) (b), (d) and (f) and mean streamwise velocity fields (a), (c) and (e) for W:D = 4:1, 6:1 and 12:1, respectively. The restitution coefficient e_n=0.85 and β_w=-0.6.

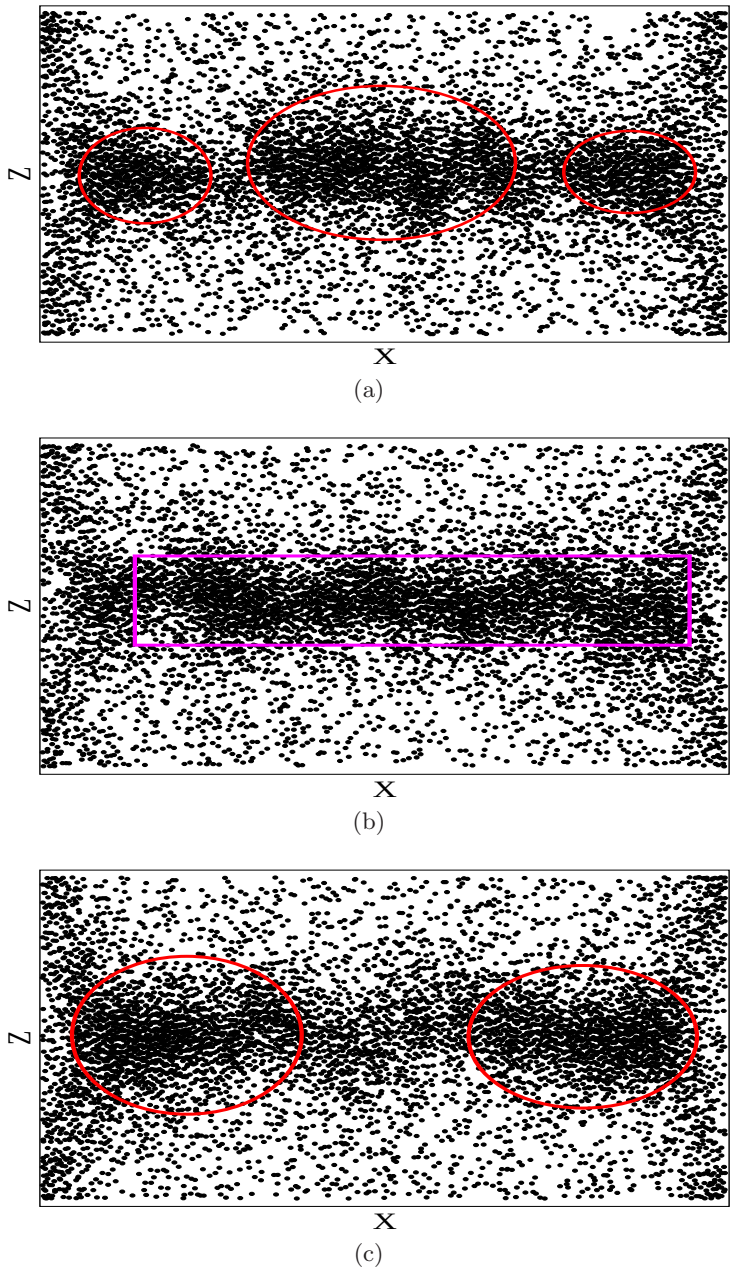

Figure 5.27: Flow in a rectangular duct: Top view of instantaneous snapshots taken at t=65.9 (a), 75.4 (b) and 85.4 (c). This is for L:W:D=1:6:1.

Chapter 6

Summary

Granular Poiseuille flow in two and three dimensions is studied. Event driven molecular dynamics is used to simulate the flow. A time and memory efficient code is written for granular Poiseuille flow based on the algorithm suggested by Rapaport (1980). Study of velocity distribution function (VDF), granular temperature bimodility and boundary conditions are the main focus in 2D granular Poiseuille flow. In case of 3D simulations; mean fields, VDF and density waves are studied for two different geometries - flow between two parallel plates and flow in a square duct. Below is the chapter-wise summary of the results.

In the first part of chapter 3, results of mass flow rate (Q) versus Knudsen number (Kn) for different volume fractions ($\nu = 0.01$, 0.1 and 0.3) show that Q increases with ν. This is because the mean free path (λ) decrease with the increase in the density of the system, with the increase in the system density the Knudsen number decreases. Change in the wall restitution coefficient from perfectly rough walls ($\beta_w \sim 1$) to smooth walls ($\beta_w \sim$ -1) increases the mass flow rate. This is because the particles tend to move along the direction of gravity after colliding with smooth walls. Knudsen paradox observed in rarefied gas flows is not observed in granular Poiseuille flow. Next, granular temperature bimodality is examined in detail. For a fixed configuration of the system, decrease in e_n increases the peak of the bimodality. The distance between the peaks initially decreases with decrease in e_n. This corresponds to a plug flow. Further, the distance between the reaches a minimum and later increases when the flow transcends to a slug flow. The value of e_n when the system reaches a minimum depends on the system volume fraction. In the last section, VDF of dilute ($\nu = 0.01$) granular Poiseuille flow is examined as function of e_n, β_w and Knudsen number, with the major focus on the tail region of the distribution. The tails tend to obey stretched exponential ($\sim C \exp^{(-\gamma(|u|/\sigma)^\alpha)}$). The exponent $\alpha \sim 2.0$ for quasi-elastic systems for Kn $\sim$ O(0.01), O(0.1) and O(1). Once dissipation is introduced into the system, α decreases with decrease in Knudsen number. The distribution function becomes broader and the x-distribution becomes asymmetric for dissipative flows ($e_n < 1$). In such cases the tails of the VDF near the walls have higher exponent than at the center as most of the clustering happens at the center of the system. For quasi elastic systems with smooth walls, $\alpha \sim 2.0$. As the wall roughness is increased ($\beta_w \sim 0.0$), the P(u_x) becomes asymmetric with a dominant peak on the negative velocity. This asymmetry is identified throughout the system for Kn $\sim$ O(1) but diminishes for lower Knudsen numbers. The P(u_y) distribution is bimodal for Kn $\sim$ O(1) in all bins. This bimodality decreases with the decrease in the Knudsen number.

Slip velocity and wall temperature are looked into in chapter 4 for $\nu = 0.01$. Knudsen number is varied by varying the width (W/d) of the channel. The slip velocity (U_w) in dilute flows is higher than in dense flows. As the system is made inelastic ($e_n < 1$), U_w decreases in case of

dilute flows but the variation of slip is negligible in dense flows. Slip velocity is highly sensitive to wall boundary conditions. With the increase in wall roughness, it decreases sharply for dense flows compared to dilute flows. It is observed that for Kn $\sim$ [0.01, 0.32], slip velocity obeys power law [$U_w \propto Kn^{\alpha}$], where α = 0.87, 0.83 and 0.73 for e_n = 0.99, 0.95 and 0.9, respectively. The gradient of slip behaves as a power law with respect to Knudsen number [$dU_w/dy \propto Kn^{\bar{\alpha}}$]. The value of this exponent $\bar{\alpha} < 0$ for Kn $>$ 0.1, is equal to 0 for [0.07 $<$ Kn $<$ 0.1] and is $>$ 0 for Kn $<$ 0.07. Wall temperature decreases reaches a minima and further increases with the decrease in e_n. Very smooth ($\beta_w \sim$ -1) and perfectly rough walls ($\beta_w \sim$ 1) have the highest wall temperatures. Decrease of e_n does not effect the gradient of wall temperature (dT_w/dy) in dilute flows but in case of dense flows this gradient increases steeply.

In the final chapter (Chp. 5), results of 3D flows are shown. Mean field profiles of streamwise velocity (U), granular temperature (T) and volume fraction (ν) are studied as a function of e_n for flow in a square duct and flow between two parallel plates. The velocity profile is flatter at the center for inelastic systems compared to the quasi-elastic systems (e_n = 0.99). This is due to accumulation of particles at the center of the system which leads to a dense flow in the core of the channel. This can be seen in the volume fraction profile. The local mean free path at the center of the system is reduced for $e_n < 1.0$. This leads to clustering and thereby, decrease in the fluctuating velocities and hence the granular temperature. The above arguments hold true for both geometries - flow between parallel plates and flow in square duct. Along with these arguments, the presence of corners in flow in a square duct results in accumulation of particles at the corners. Next VDFs are studied at different positions in the system for changing e_n. The VDFs of inelastic systems tend to become broader and $P(u_x)$ becomes asymmetric for lower values of e_n. The degree of asymmetry increases as we move from the wall towards the center. VDF is calculated for an additional bin at the corner of the system for flow in a square duct. VDF of the corner bin is symmetric for all values of e_n but becomes broader as e_n is reduced. Next, density wave formation in both the geometries are studied (square inlet). Starting with a cubic lattice configuration, we see that during the initial time of simulation, particles tend to accumulate close to the walls (and corners for flow in square duct) to form a density wave. As the simulation proceeds, these density waves migrate towards the center of the system and merge to form a central plug. Further more, they transform to symmetric, asymmetric and finally slug flow. All these density waves modes are identified by calculating the power spectra of slices taken at various positions of the system and analysis is done in a similar method as reported by Conway & Glasser (2004). Furthermore, it is observed that dense corners influence the central dense wave. Simulation done for rectangular ducts of varying W:D ratio, yield interesting results. The density waves separate out and constantly migrated back and forth from the center to the walls. This migration is an effect due to the presence of corners.

References

Alam, M. & Chikkadi, V. 2010 Velocity distribution function and correlations in a granular poiseuille flow. *Journal of Fluid Mechanics* **653**, 175.

Alam, M., Chikkadi, V. & Gupta, V. 2009 Density waves and the effect of wall roughness in granular poiseuille flow: Simulationand linear stability. *The European Physical Journal Special Topics* **179** (1), 69–90.

Allen, M. P. & Tildesley, D. J. 1989 *Computer simulation of liquids*. Oxford university press.

Aoki, K., Takata, S. & Nakanishi, T. 2002 Poiseuille-type flow of a rarefied gas between two parallel plates driven by a uniform external force. *Physical Review E* **65** (2), 026315.

Blair, D. L. & Kudrolli, A. 2001 Velocity correlations in dense granular gases. *Physical Review E* **64** (5), 050301.

Brey, J. J., Cubero, D. & Ruiz-Montero, M. 1999 High energy tail in the velocity distribution of a granular gas. *Physical Review E* **59**, 1256–1258.

Brey, J. J. & Ruiz-Montero, M. 2003 Velocity distribution of fluidized granular gases in the presence of gravity. *Physical Review E* **67** (2), 021307.

Campbell, C. S. 1990 Rapid granular flows. *Annual Review of Fluid Mechanics* **22** (1), 57–90.

Chikkadi & Alam 2007 Velocity distribution and the effect of wall roughness in granular poiseuille flow. *Physical Review E* **75** (5), 051306.

Chikkadi, V. & Alam, M. 2009 Slip velocity and stresses in granular poiseuille flow via event-driven simulation. *Physical Review E* **80** (2), 021303.

Conway, S. L. & Glasser, B. J. 2004 Density waves and coherent structures in granular couette flows. *Physics of Fluids* **16**, 509.

Denn, M. M. 2001 Extrusion instabilities and wall slip. *Annual Review of Fluid Mechanics* **33** (1), 265–287.

Dongari, N., Sharma, A. & Durst, F. 2009 Pressure-driven diffusive gas flows in micro-channels: from the knudsen to the continuum regimes. *Microfluidics and nanofluidics* **6** (5), 679–692.

Duran, J. 2000 *Sands, powders, and grains*. Springer New York.

Ellingsen, S. Å., Gjerden, K. S., Grøva, M. & Hansen, A. 2010 Model for density waves in gravity-driven granular flow in narrow pipes. *Physical Review E* **81** (6), 061302.

Esipov, S. E. & Pöschel, T. 1997 The granular phase diagram. *Journal of statistical physics* **86** (5-6), 1385–1395.

Forterre, Y. & Pouliquen, O. 2001 Longitudinal vortices in granular flows. *Physical Review Letters* **86** (26), 5886.

Galvin, J., Hrenya, C. & Wildman, R. 2007 On the role of the knudsen layer in rapid granular flows. *Journal of Fluid Mechanics* **585**, 73–92.

Goldhirsch, I. 2003 Rapid granular flows. *Annual review of fluid mechanics* **35** (1), 267–293.

Goldsack, D. E., Leach, M. F. & Kilkenny, C. 1997 Natural and artificial'singing'sands. *Nature* **386**, 29.

Horikawa, S., Nakahara, A., Nakayama, T. & Matsushita, M. 1995 Self-organized critical density waves of granular material flowing through a pipe. *Journal of the Physical Society of Japan* **64** (6), 1870–1873.

Ichiki, K. 1995 Hydrodynamic effects in density waves of granular flows. *arXiv preprint adap-org/9505004* .

Jaeger, H. M., Nagel, S. R. & Behringer, R. P. 1996 Granular solids, liquids, and gases. *Reviews of Modern Physics* **68** (4), 1259–1273.

Karniadakis, G. E., Beskok, A., Aluru, N. R. *et al.* 2005 *Microflows and nanoflows: fundamentals and simulation*, , vol. 29. Springer Science+ Business Media.

Khain, E. 2011 Dense granular poiseuille flow. *Mathematical Modelling of Natural Phenomena* **6** (04), 77–86.

Knudsen, M. 1909 Die gesetze der molekularstromung und der inneren reibungsstromung der gase durch rohren. *Ann. Phys.* **333**, 75–130.

Lauga, E., Brenner, M. P. & Stone, H. A. 2005 Microfluidics: the no-slip boundary condition. *arXiv preprint cond-mat/0501557* .

Liss, E. D., Conway, S. L. & Glasser, B. J. 2002 Density waves in gravity-driven granular flow through a channel. *Physics of Fluids* **14**, 3309.

Lubachevsky, B. D. 1991 How to simulate billiards and similar systems. *Journal of Computational Physics* **94** (2), 255–283.

Luding, S. & McNamara, S. 1998 How to handle the inelastic collapse of a dissipative hard-sphere gas with the tc model. *Granular Matter* **1** (3), 113–128.

Lun, C. & Savage, S. 1986 The effects of an impact velocity dependent coefficient of restitution on stresses developed by sheared granular materials. *Acta Mechanica* **63** (1-4), 15–44.

Mansour, M., Baras, F. & Garcia, A. L. 1997 On the validity of hydrodynamics in plane poiseuille flows. *Physica A: Statistical Mechanics and its Applications* **240** (1), 255–267.

McNamara, S. & Young, W. 1992 Inelastic collapse and clumping in a one-dimensional granular medium. *Physics of Fluids A: Fluid Dynamics* **4**, 496.

Möbius, M. E., Lauderdale, B. E., Nagel, S. R. & Jaeger, H. M. 2001 Brazil-nut effect: Size separation of granular particles. *Nature* **414** (6861), 270–270.

Moon, S. J., Shattuck, M. & Swift, J. 2001 Velocity distributions and correlations in homogeneously heated granular media. *Physical Review E* **64** (3), 031303.

Moon, S. J., Swift, J. & Swinney, H. L. 2004 Steady-state velocity distributions of an oscillated granular gas. *Physical Review E* **69** (1), 011301.

Moriyama, O., Kuroiwa, N., Matsushita, M. & Hayakawa, H. 1998 4/3 law of granular particles flowing through a vertical pipe. *Physical review letters* **80** (13), 2833.

van Noije, T. & Ernst, M. 1998 Velocity distributions in homogeneous granular fluids: the free and the heated case. *Granular Matter* **1** (2), 57–64.

Ottino, J. & Khakhar, D. 2000 Mixing and segregation of granular materials. *Annual Review of Fluid Mechanics* **32**, 55–91.

Peng, G. & Herrmann, H. J. 1994 Density waves of granular flow in a pipe using lattice-gas automata. *Physical Review E* **49** (3), R1796.

Porodnov, B., Suetin, P., Borisov, S. & Akinshin, V. 1974 Experimental investigation of rarefied gas flow in different channels. *Journal of Fluid Mechanics* **64** (3), 417–437.

Pöschel, T. & Schwager, T. 2005 *Computational granular dynamics: models and algorithms*. Springer.

Raafat, T., Hulin, J. & Herrmann, H. 1996 Density waves in dry granular media falling through a vertical pipe. *Physical Review E* **53** (5), 4345.

Rao, K. K., Nott, P. R. & Sundaresan, S. 2008 *An introduction to granular flow*. Cambridge University Press Cambridge.

Rapaport, D. 1980 The event scheduling problem in molecular dynamic simulation. *Journal of Computational Physics* **34** (2), 184–201.

Rapaport, D. C. 2004 *The art of molecular dynamics simulation*. Cambridge university press.

Riethmüller, T., Schimansky-Geier, L., Rosenkranz, D. & Pöschel, T. 1997 Langevin equation approach to granular flow in a narrow pipe. *Journal of statistical physics* **86** (1-2), 421–430.

Rosato, A., Strandburg, K. J., Prinz, F. & Swendsen, R. H. 1987 Why the brazil nuts are on top: Size segregation of particulate matter by shaking. *Physical Review Letters* **58** (10), 1038.

Rouyer, F. & Menon, N. 2000 Velocity fluctuations in a homogeneous 2d granular gas in steady state. *Physical review letters* **85** (17), 3676–3679.

Schulze, D. 2012 Powders and bulk solids. *Journal of Statistical Mechanics: Theory and Experiment* **2006** (07).

Shinbrot, T. & Muzzio, F. J. 1998 Reverse buoyancy in shaken granular beds. *Physical review letters* **81** (20), 4365.

Sperl, M. 2006 Experiments on corn pressure in silo cells–translation and comment of janssen's paper from 1895. *Granular Matter* **8** (2), 59–65.

Succi, S. 2002 Mesoscopic modeling of slip motion at fluid-solid interfaces with heterogeneous catalysis. *Physical review letters* **89** (6), 064502–064502.

Taheri, P. & Struchtrup, H. 2012 Poiseuille flow of moderately rarefied gases in annular channels. *International Journal of Heat and Mass Transfer* **55** (4), 1291–1303.

Tij, M. & Santos, A. 2004 Poiseuille flow in a heated granular gas. *Journal of statistical physics* **117** (5-6), 901–928.

Toschi, F. & Succi, S. 2005 Lattice boltzmann method at finite knudsen numbers. *EPL (Europhysics Letters)* **69** (4), 549.

Vriend, N. 2010 *Booming sand dunes*.

Wang, C., Jackson, R. & Sundaresan, S. 1997 Instabilities of fully developed rapid flow of a granular material in a channel. *Journal of Fluid Mechanics* **342**, 179–197.

van Zon, J. & MacKintosh, F. 2004 Velocity distributions in dissipative granular gases. *Physical review letters* **93** (3), 038001.

van Zon, J. & MacKintosh, F. 2005 Velocity distributions in dilute granular systems. *Physical Review E* **72** (5), 051301.